LIQUID-ON-LIQUID MIXING
FOR SLIDE-BASED BIOLOGICAL ASSAYS

A Dissertation

Presented to the Faculty of the Graduate School

of Cornell University

in Partial Fulfillment of the Requirements for the Degree of

Doctor of Philosophy

by

Richard Cheng-I Yeh

January 2007

LIQUID-ON-LIQUID MIXING
FOR SLIDE-BASED BIOLOGICAL ASSAYS

Richard Cheng-I Yeh, Ph.D.

Cornell University 2007

Many parallel biochemical assays rely on thin aqueous films to spread a reactant solution over a wide area decorated with multiple distinct substrates. In this asymmetric, microfluidic geometry, diffusion limits the transport of reactants to substrates. Chemical equilibrium, a requirement for reproducibility of results, can take days to achieve.

The liquid-on-liquid mixing (LOLM) method overcomes the diffusion barrier by layering an immiscible spectator fluid, such as mineral oil, on the thin film. Stirring the spectator fluid transmits shear at the liquid-liquid interface into the thin film. The mixing accelerates the march towards equilibrium. This technique increases the speed and sensitivity of immunofluorescence staining of *Drosophila* larval polytene chromosomes by a factor of 100 in time and concentration, when compared to standard coverslip techniques.

Flow visualization experiments reveal the fluid motions in the thin aqueous layer. Using time-lapse video photography to monitor the evolution of a drop of colloidal dye in the thin film, I estimate the time needed to achieve good mixing at various stir rates.

The major aim of this technique is improving the hybridization step in DNA microarrays. I printed microarrays and subjected them to hybridizations with varying

stir rates, durations, and target DNA concentrations. My data suggest that the mixing produces at best a modest improvement in efficiency, uniformity, sensitivity, and specificity when compared to microarrays incubated with the standard coverslip method.

BIOGRAPHICAL SKETCH

Richard C. Yeh was born on February 15, 1976 in Pasadena, California, the son of an immigrant physics graduate student who had taken “Albert” as a Western middle name and may have had another famous physicist in mind for his firstborn. On the same date twelve years later, Richard Feynman died.

Richard C. Yeh majored in physics at Caltech. He graduated in 1998 with the degree of Bachelor of Science and matriculated at Cornell University, obtaining the degree of Master of Science in 2002. In 2004, he undertook a fellowship in science and technology policy at the National Academies. He worked from 2005 to 2006 at National Security Technologies (then Bechtel Nevada / Lockheed Martin Nevada Technologies) in Los Alamos, where the public library holds a tape recording of Hans Bethe’s eulogy for Feynman. He now works at Bank of America in Manhattan

ACKNOWLEDGMENTS

I am grateful to Professor Carl Franck for continuous support, encouragement, and critical reading of this doctoral dissertation.

Special thanks to Eric D. Siggia for pointing out the possible diffusion bottleneck in slide-based assays; to Brian E. Schwartz and Janis K. Werner for training me and offering advice on polytene chromosome preparation and staining; to Jerome K. Hyun for assembling the stirrer controller; to Alice M. Crawford and Arthur La Porta for discussions on fluid dynamics; to K. Andre Mkhoyan for recommending software to take time-lapse image sequences; to Eberhard Bodenschatz for a gift of flow tracers; to Paul Debbie for hints on microarray printing; to Shannon Guiles for making the DNA solutions used for microarray printing and hybridization; to Stephen A. Jesch and Susan A. Henry for instruction and sponsorship in the use of the microarray scanner; to Lynn Winkleman at the University of Michigan, M. Juanita Martinez at the University of New Mexico, and S. Caprice Rosato at Oregon State University for diagnosing the intrinsic fluorescence of DMSO; to Patricia J. Koutz at V&P Scientific, for detailed technical support with microarray printing; to Michael DeFreitas and Wilson Lew at Axon, for detailed technical support with microarray scanning; to Jason Carpentier for collecting additional flow-visualization data; to Benjamin Smith for careful analysis and data at critical junctures; to James P. Sethna for advice on improving the discussion of mixing theory.

I want to thank my current and former committee members: Barbara H. Cooper, Carl Franck, Sol M. Gruner, Donald L. Hartill, James P. Sethna, Saul A. Teukolsky, and Michelle D. Wang; David J. BenDaniel; Veit Elser; Douglas B. Fitchen; Debra A. Hatfield; John T. Lis; Robert F. Snedeker; Eva Tardos;

my teachers at Caltech and Thousand Oaks High School; Derek Cheung; K.C. and Jenny Wang; my manager Thomas W. Tunnell; my friends: Karen Adelman, Janis L. Chang, Elaine L. Cheung, David C. Fang, Liesl Folks, Sommer E. Gentry, Chunlei Huan, Wei-Hwa Huang, Benjamin C. Jantzen, Daniel S. Johnson, Jennifer M. Kitahara, Steven J. Koch, Steven I. Kwon, Arthur La Porta, Christianto C. Liu, Yufen Lee Mehta, Erik M. Muller, Alexander C. Ney, Akiko Shirakawa, Valerie E. Sugiyama, Patricia T. Viele, Yujun Wang, Kim D. West, Jonathan P. Wrubel, Nikao Yang; my parents; my sister Helen; my wife Xiaoli — for believing in me even when I did not.

This work was supported by the Cornell University Center for Biotechnology, a New York State Center for Advanced Technology, supported by the New York State Office for Science, Technology, and Academic Research and industrial sponsors. This material is based upon work supported in part by the STC Program of the National Science Foundation under Agreement No. ECS-9876771, through the Cornell Nanobiotechnology Center (NBTC). This work made use of the computing facility of the Cornell Center for Materials Research (CCMR), supported through the National Science Foundation Materials Research Science and Engineering Centers (MRSEC) program (DMR-0079992). This work made use of a site license for National Instruments LabVIEW software purchased by Cornell's Laboratory of Atomic and Solid-State Physics. I thank Cornell University and in particular the Department of Physics for awarding me a teaching assistantship in the spring of 2004 to allow me to conduct this research.

TABLE OF CONTENTS

LIST OF TABLES

LIST OF FIGURES

ABBREVIATIONS AND GLOSSARY

bp	base pairs
CCD	charge-coupled device
dc	direct current
DMSO	dimethyl sulfoxide
DNA	deoxyribonucleic acid
dsDNA	double-stranded deoxyribonucleic acid
E. coli	Escherichia coli
feature	*please see* "spot"
LOLM	liquid-on-liquid mixing
µg	microgram
µl	microliter
µm	micrometer
ng	nanogram
nl	nanoliter
nt	nucleotides
PCR	polymerase chain reaction
PMT	photomultiplier tube
probe	known DNA molecules immobilized on the glass microarray surface. Compare target.
RNA	ribonucleic acid

rpm	revolutions per minute
spot	In Chapter 3, “dye spot” is the portion of the reaction chamber or image thereof covered with a high concentration of the polystyrene microsphere colloidal-dye tracers. In Chapter 4, “probe spot” is the mass of DNA left on the glass substrate after the printed probe DNA solution dries, as well as the location of these masses. Also in Chapter 4, “fluorescent spot” is the collection of pixels comprising the fluorescent image of a probe spot — also known as a feature. In Chapter 8 (Appendix), “spot” is the collection of pixels comprising the fluorescent image of a mass of dried target DNA solution. In Chapter 8 (Appendix), “spot” is used as a verb to mean the process of printing DNA onto a substrate, and as a noun to mean the result of that process.
ssDNA	single-stranded deoxyribonucleic acid
target	DNA molecules in aqueous solution applied to the microarray in a hybridization experiment. Compare probe.
V	voltage
v/v	volume of solute added as a fraction of final solution volume

1 INTRODUCTION

Physics has had a long history of technology transfer and development for medicine. Developments in optics led to van Leeuwenhoek's microscope, used today by pathologists to identify diseased tissues and disease-causing bacteria. Roentgen's x-rays, aside from their applications in medical imaging and cancer treatment, led to Bragg's diffractometer, which in turn enabled the discovery of DNA's double-helical structure. Townes's maser led to the laser, now used for fluorescence excitation in biomedical research. In the past ten years, DNA microarrays have become a popular tool for genetic research, notably enabling the identification of the family of viruses responsible for severe acute respiratory syndrome (Wang et al., 2003), and now physicists are working to validate and improve microarray technology. DNA microarrays are supposed to enable the parallel, quantitative, rapid measurement of known gene sequences in an unknown sample — a test that will enable precision cancer diagnosis (see, for example, Chen, Bilke, and Khan, 2005) and prescriptions tailored to individual genomic profiles — but, as we shall see later, their use is not very quantitative and far from rapid. These problems, belied by the rapid commercialization of the technology, must be overcome before microarrays can jump from the lab to the clinic.

Conventional DNA microarrays are an example of a slide-based assay where chemical reactions must occur in a thin aqueous film. Such reactions in microfluidic geometries are all rate-limited by diffusion, and this dissertation explores a method for overcoming this diffusion limitation in slide-based assays. This dissertation has the following organization: I first describe an experiment on the immunofluorescence staining of polytene chromosomes, which will illustrate the operation of the liquid-on-liquid mixing (LOLM) system for slide-based assays; I then describe flow-

visualization experiments, which provide a quantitative measure of the performance of the liquid-on-liquid mixing system; I describe my initial experiments with liquid-on-liquid mixing applied to DNA microarrays; and finally, I discuss mixing from a dynamical systems perspective, how the geometry of the mixing chamber affected its performance, and potential future experiments.

2 IMMUNOFLUORESCENCE STAINING OF POLYTENE CHROMOSOMES[1]

2.1 Introduction

Reactions in thin films are important in the modern genetics laboratory. Typically performed under a cover glass, they are found in experimental techniques such as in-situ hybridization, microarrays, and immunohistochemistry. (Bowtell and Sambrook, 2003) One problem associated with thin films in such slide-based techniques is that convective transport processes are absent and reactants diffuse so slowly that assays may require hours or days to reach equilibrium. (Duggan et al., 1999; Siggia, 2001) To overcome this diffusion limitation, several researchers have introduced techniques to increase the motion of reactants in slide-based assays. (Holloway et al., 2002)

In this paper, we describe the liquid-on-liquid mixing (LOLM) method for stirring thin films. This method has the advantage of preserving the small reactant volumes associated with the conventional "coverslip" method (for example: 12–15 μl, Brown, 1999; 34 μl, DeRisi, 2001) while avoiding the potential dangers associated with the use of cover glasses, such as trapped bubbles and scratched slide substrates, and complications such as excessive or insufficient humidification (Best et al., 2003). It does so by layering a liquid, immiscible with and less dense than the aqueous bioreactant solution, over the thin film. This stirrer liquid touches and spreads the

[1] Reprinted from Journal of Biochemical and Biophysical Methods, Vol. 64, Richard C. Yeh, Jerome K. Hyun, Amber K. Boehm, John T. Lis, and Carl Franck, "Improving Slide-Based Assays by Stirring: Application of Liquid-on-Liquid Mixing to Immunofluorescence Staining of Polytene Chromosomes," Pages 59–68,

reactant solution as a cover glass would, but does not contact the slide surface. Hydrodynamic shear is transmitted across the liquid-liquid interface; by stirring the confining liquid, we can mix the fluid in the thin film.

The LOLM setup resembles the Ventana Medical Systems, Inc. Discovery™ system, except that the LOLM mineral oil cover is thicker and more viscous than Ventana's Liquid Coverslip™ (Miller et al., 1993), and the LOLM method uses a paddle to stir the mineral oil directly, unlike Ventana's method of directing air jets on the covering liquid (Copeland et al., 1997). In addition, the LOLM system is able to use reactant volumes as small as 10 µl, which can enable researchers to use less material or higher concentrations, potentially obtaining higher signals, compared to the 100 µl or more required for most of the automated systems recently reviewed by Holloway et al. (2002), including the Ventana system.

Very recently, an alternative approach to active mixing has been introduced by Advalytix (http://www.advalytix.com/). Their ArrayBooster™ system uses surface acoustic waves to agitate volumes as small as 10 µl, comparable to our system's capabilities, although it is not clear over how wide an area the reactant volume can be spread. Compared to both the Ventana and Advalytix systems, our scheme offers the advantages of considerable simplicity and economy.

2.2 Materials and Methods

Our flow visualization studies with non-diffusing colloidal dye tracers described in Chapter 3 indicate that the LOLM scheme used for this experiment promotes effective spreading of the tracers over 70% of the surface of the reaction chamber, which is sufficient for the present application because there are many (typically 50) squashed nuclei in each preparation. To compare the efficacy of our technique with the conventional coverslip method for spreading thin films of

bioreactant solution, we performed parallel immunofluorescence staining experiments that differed in the incubation condition of the primary antibody. This strategy is shown as a flowchart in Figure 2-1. To determine the limitations that diffusion places on our system, we repeated the experiment at various antibody concentrations and staining durations, which are shown as points in Figure 2-4.

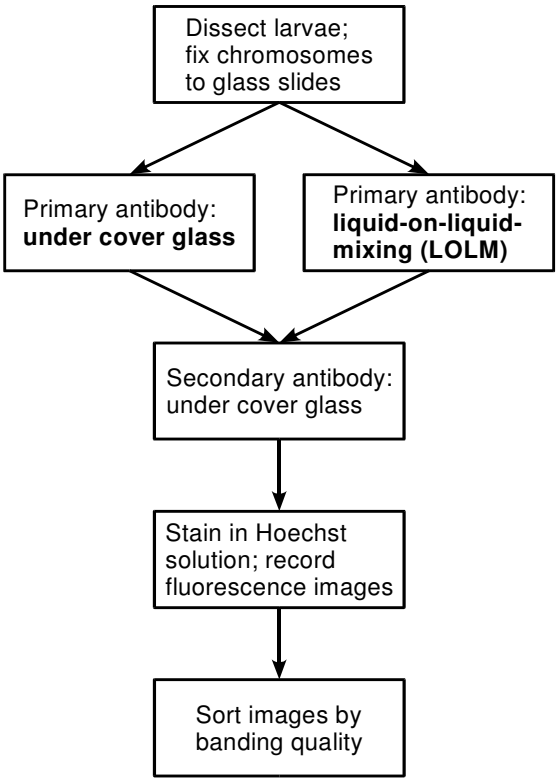

Figure 2-1: Flowchart of the experimental procedure used to validate the liquid-on-liquid mixing staining method. We compared standard incubations, where the primary antibody solution was spread with a cover glass, with the liquid-on-liquid mixing method. Slides were assigned to stir and no-stir stain conditions in such a way as to eliminate any bias in the quality of the chromosome spreads. In all other steps, the samples received the same treatment.

2.2.1 Liquid-on-liquid mixing (LOLM)

The liquid-on-liquid mixing apparatus is shown in Figure 2-2. The wall of the 1.9-cm (¾-inch) diameter cylindrical reaction chamber was made of acrylic. The glass slide bearing the chromosome sample was held at the bottom opening of the cylinder. An O-ring prevented liquid leakage between the glass-acrylic gap. The 20-µl antibody solution (described below) was pipetted to the surface of the slide facing the cylinder, wetting that surface. Then, 3 ml of mineral oil (heavy paraffin oil, Fisher) was pipetted over the thin film of antibody solution.

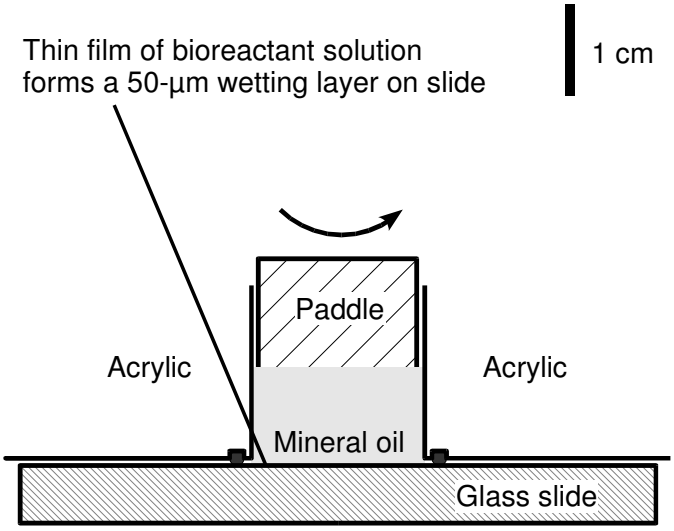

Figure 2-2: Diagram of the liquid-on-liquid mixing technique for delivering primary antibodies to chromosomes fixed on slides. In the current experiment, the cylindrical reaction chamber is bounded from below by the glass slide bearing the polytene chromosomes, and on the sides by acrylic, with an O-ring to seal the glass-acrylic gap. After the slide is fixed in place, the antibody solution (20 µl) is pipetted into the reaction chamber, wetting the slide in a thin film, and the mineral oil stirring fluid (3 ml) is pipetted over the aqueous layer. A stirring paddle is immersed in the mineral oil and turns at 3.4 rpm.

Finally, a paddle (spanning almost the entire diameter of the cylindrical cavity) was immersed in the mineral oil to a depth where its edge was 4 mm from the surface of the slide. The paddle was turned along the axis of the cylindrical reaction chamber continuously at 3.4 rpm. At the end of stirring, the paddle was lifted out of the mineral oil. Distilled water was pipetted into the reaction chamber, lifting the mineral oil away from the slide. The slide was removed from the holder and rinsed with distilled water to remove any residual mineral oil. To avoid contamination, the O-ring was discarded and the reaction chamber was cleaned after each use. Compared to the coverslip method, this procedure is easy to perform, requiring only a few additional pipetting steps.

2.2.2 Immunofluorescence staining

Polytene chromosomes from *Drosophila melanogaster* third-instar-larval salivary glands were fixed to base-treated microscope slides and stained as described by Lis et al. (2000) with the following modifications. The slides were stained for either 10 minutes or 1 hour with 20 µl of RNA Pol II antibody H14 (MMS-134R supplied as 3–5 mg/ml, Covance Research Products, Berkeley, CA) diluted 1:10, 1:100, 1:500, 1:1,000, or 1:10,000 in 5% normal donkey serum (Jackson ImmunoResearch Laboratories, Inc., West Grove, PA) in 10-mM Tris-buffered saline. The antibody solution was either incubated under a cover glass in a moist chamber or stirred with the LOLM technique. Usually, at least two slides were subjected to each antibody dilution, staining duration, and incubation condition.

The slides were washed, and then secondary antibody stainings were performed by incubation under a cover glass for 1 hour in a moist chamber, using a 1:100 dilution of rhodamine Red-X-conjugated anti-mouse immunoglobulin (Ig) M (Jackson ImmunoResearch Laboratories, Inc.). The slides were then washed again,

stained with 0.8 µg/ml Hoechst 33258 (Sigma) in Tris-buffered saline, washed again, and mounted without fluorescent microspheres.

In keeping with standard practice, we selected the best-spread and best-stained chromosomes on each slide and recorded, pseudocolored, and overlaid fluorescent images of them. We expect that the intensity of the rhodamine (red) fluorescence will depend on the quantity of the H14 antibody that bound to the epitopes. The quality of banding in the rhodamine fluorescence for each chromosome image was rated as clear (for distinct banding on most or all of the chromosome arms), faint (for banding patterns with lower fluorescent intensity), or none (for no fluorescence, nonspecific fluorescence, fluorescence patterns consisting only of discrete dots, and incomplete or nonuniform staining). Exemplar images for each banding category appear in Figure 2-3.

2.3 Results and Discussion

Table 1 shows the image quality of the best-stained polytene chromosome on each slide. We chose to report only the best-quality stain that could be expected under each set of experimental conditions because standard practice demands use of high-quality stained chromosomes: those are the ones from which the level of transcription initiation or other activity can be most readily inferred.

2.3.1 Diffusion model

In this section, we roughly estimate that in all cases, the total binding capacity of the antibody molecules in solution was at least the total number of epitopes on the slide; however, without stirring, diffusion probably prevented most of the antibodies from visiting and binding to the antigens.

The H14 antibody is an IgM that binds to the heptapeptide repeats phosphorylated at Ser5 found in the C-terminal domain of elongating RNA polymerase II (Bregman et al., 1995; O'Brien et al., 1994). IgMs form pentamers, each with 10 epitope-binding sites and a molecular weight of 950 kDa. The 3–5-mg/ml stock concentration of H14 represents 3–5 µM. At the 1:10,000 dilution (the lowest concentration used) of the primary antibody, there would be 4×10^9 H14 pentamers in the 20 µl antibody solution; given that the equilibrium dissociation constant of H14 has been reported by Jones et al. (2004) to be "in the low nanomolar range", this lowest concentration and amount of H14 pentamers could bind 6×10^7–7×10^9 epitopes.

By comparison, we estimate the total number of epitopes as the product of: 10 epitopes per polymerase enzyme (In *Drosophila,* each RNA polymerase II enzyme has 42 heptapeptide repeats (Patturajan et al., 1998; Zehring et al., 1988), but many fewer than 42 are phosphorylated (O'Brien et al., 1994).); 500–5,000 active polymerase enzymes per chromatid (O'Brien and Lis (1991) found that upon heat-shock induction, 25 Pol II enzymes gather on each of the two *hsp70* genes at 87A. Visual estimates of H14 staining suggest that those 50 polymerases represent between 1% and 10% of the signal from the whole squashed nucleus.); 1,000–2,000 chromatids per polytene chromosome [1,024, (Alberts et al., 1994, p. 349); 1,024, (Lewin, 2000, p. 558); 1,000–2,000, (Lodish et al., 2000, p. 272); 2,000, (Rudkin, 1972)]. In this way, each cell yields 5×10^6–1×10^8 epitopes. Each larva's pair of salivary glands consists of about 50 cells, so the total product is some 2×10^8–5×10^9 epitopes per slide.

Figure 2-3: Sample images of stained polytene chromosomes.

For each example, the color picture with both the Hoechst (blue) and rhodamine (red) fluorescence is shown as a guide to the eye; the grayscale image showing only the rhodamine intensity is evaluated for banding quality. The images were captured with a 63x objective. The exposure times were adjusted to compensate for different levels of overall fluorescence. The green box in each 138-µm × 105-µm whole-chromosome image (A, B, C, D) shows the location of the corresponding 13-µm × 13-µm detail (a, b, c, d). Samples (A) and (B) (upper row) were incubated with a 1:500 dilution of H14 antibody for 10 minutes. Samples (C) and (D) (lower row) were incubated with a 1:10,000 dilution of H14 antibody for 1 hour. Samples (A) and (C) (left column) were stained with the coverslip (unstirred) method, while samples (B) and (D) (right column) were stained using the liquid-on-liquid mixing (stirred) method. The banding qualities assigned to each sample are: (A) faint; (B) clear; (C) none; (D) clear.

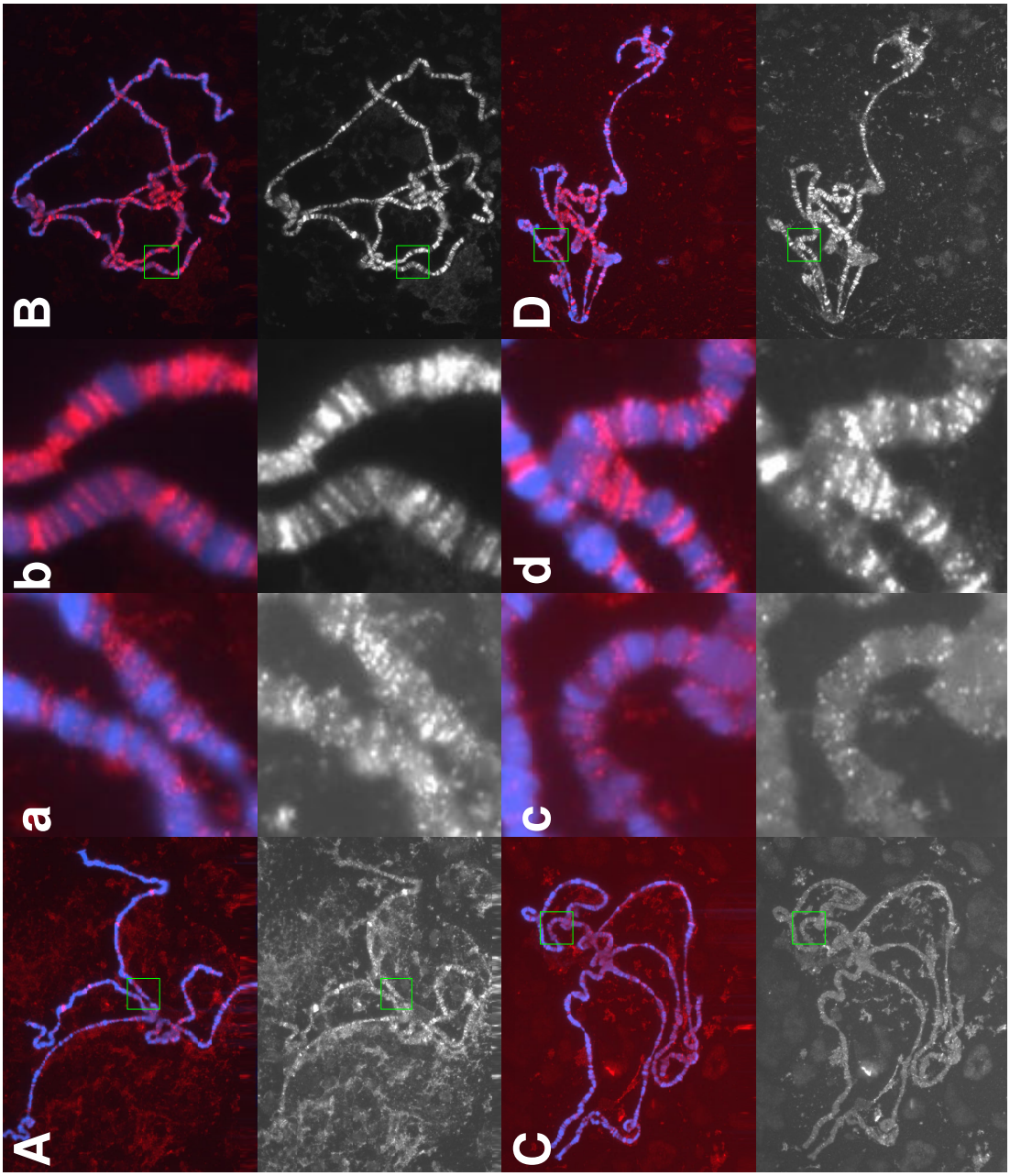
B
D
b
d
a
c
A
C

Table 1: **Fluorescent banding quality of stained chromosomes under various stain conditions.**

Each row contains results for a particular concentration of the H14 primary antibody, represented as a dilution ratio from stock. Each column specifies the staining duration and condition: "coverslip" indicates that the conventional coverslip method was used for the primary antibody incubation step; "LOLM" means that the primary antibody was stirred with the liquid-on-liquid mixing technique during incubation. Each symbol (● clear; ○ faint; × none) denotes the quality of the best-stained chromosome out of the approximately 50 salivary gland cells from a single larva fixed on each slide. Empty categories denote untested conditions. Higher concentrations of the H14 antibody and longer antibody incubation times produce better-quality chromosome stains. For most cases and particularly at the lowest concentrations of antibody, there is an improvement in stain quality due to stirring.

H14 dilution	10-minute coverslip (unstirred)	10-minute LOLM (stirred)	1-hour coverslip (unstirred)	1-hour LOLM (stirred)
1:10		●	●	
1:100	●●	●●○		
1:500	●●	●●●●○	●●●	
1:1,000	××××	●○○×××	●●○○○	●●
1:10,000		××	○×××	●●

When using the coverslip method for primary antibody staining, diffusion will limit the number of antibodies that may visit any given antigen. In two dimensions, it is expected that it will take an amount of time $t = x^2 / 4D$ for a particle with diffusion constant D to travel a distance x (Probstein, 1994). We estimate the number of antibodies near a single epitope in time t by calculating the number of H14 molecules present in a disk of radius x centered at the epitope. We assume that the antibodies are uniformly distributed under the cover glass, with constant area number density

σ = (Avogadro's number) × (molar concentration) ×
(reactant solution volume) / (total cover glass area)

barring local depletions and loss of reactant solution, and obtain:

(Number of antibodies in a disk of radius one diffusion-length) = $4 \pi D t \sigma$

We estimate the diffusion constant of the IgM pentamer to be 2×10^{-7} cm^2/s, since the calculation from the Stokes-Einstein fluctuation-dissipation relation (Probstein, 1994) falls within the range expected for molecules of similar mass (van Holde, 1985, p. 103, table 4.3). Our cover glasses are 22 mm square. Contours in Figure 2-4 indicate antibody concentrations and incubation times for which a diffusion-radius disk would be expected to encompass 10^6, 10^7, 10^8, 10^9, and 10^{10} IgM antibody pentamers. Assuming complete and rapid binding (i.e., the reactant concentration is sufficient to drive the stoichiometric equilibrium to the bound state), 5×10^5–1×10^7 IgM pentamers would be just enough to saturate all 5×10^6–1×10^8 epitopes in an isolated squashed nucleus. We would expect staining conditions on lower left side of some contour in the range 5×10^5–1×10^7 (lower concentrations and shorter times) to starve the epitopes for antibodies and conditions on the upper

right side (higher concentrations and longer times) to present enough antibodies in the diffusion-radius disk for all the epitopes, as long as the H14 concentration exceeds the equilibrium dissociation constant. For example, following the 10^8 IgM pentamers contour, this model predicts that the raw ascites fluid (stock concentration) should deliver enough antibodies to the epitopes to produce clear staining in a 10-second incubation, but it cannot say that all the antibodies visiting the epitopes in a 24-hour incubation at the subnanomolar 1:10,000 concentration will bind and remain bound.

If the H14 antibodies were monomers instead of pentamers, the molecular diffusion constant would approximately double, which would shift all the contours down and to the left. The factor-of-five increase in number concentration would be balanced by the factor-of-five decrease in the number of binding sites per molecule.

2.3.2 Diffusion is limiting

Comparing the banding quality of the samples that underwent incubations using the coverslip method for 10 minutes and 1 hour, we find that clear images can be obtained with either incubation duration for H14 antibody concentrations as low as 1:500 of stock. At the 1:1,000 antibody concentration with the coverslip method, the 10-minute incubations produced images with very low fluorescence and no banding, but the 1-hour incubations — which allowed an expected six times as many antibody molecules to diffuse to the chromosomes — produced images with clear banding. In Figure 2-4, these data are shown against the contours that estimate the number of antibodies in a diffusion-radius disk about each chromosome. These results are in qualitative agreement with the notion that diffusion presents a barrier limiting the quantity of antibody that visits any antigen.

Figure 2-4: **Diffusion limitation of conventional coverslip antibody staining technique. The map shows the estimated number of H14 antibody molecules available to any antigen site by diffusion without stirring, as a function of concentration (as a common logarithm of the fraction of the stock 3–5-µM concentration, i. e., –3 denotes a 1:1,000 dilution, or 3–5 nM) and incubation time (common log of number of seconds). The straight lines are isopleths representing 10^6, 10^7, 10^8, 10^9, and 10^{10} IgM pentamers in the span of a single-diffusion-length-radius disk. The ■ symbols represent conditions where we performed experiments. Next to some of the experimental conditions, other symbols (● clear; ○ faint; × none) indicate the average quality of the coverslip-method slides from Table 1**: **Fluorescent banding quality of stained chromosomes under various stain conditions..**

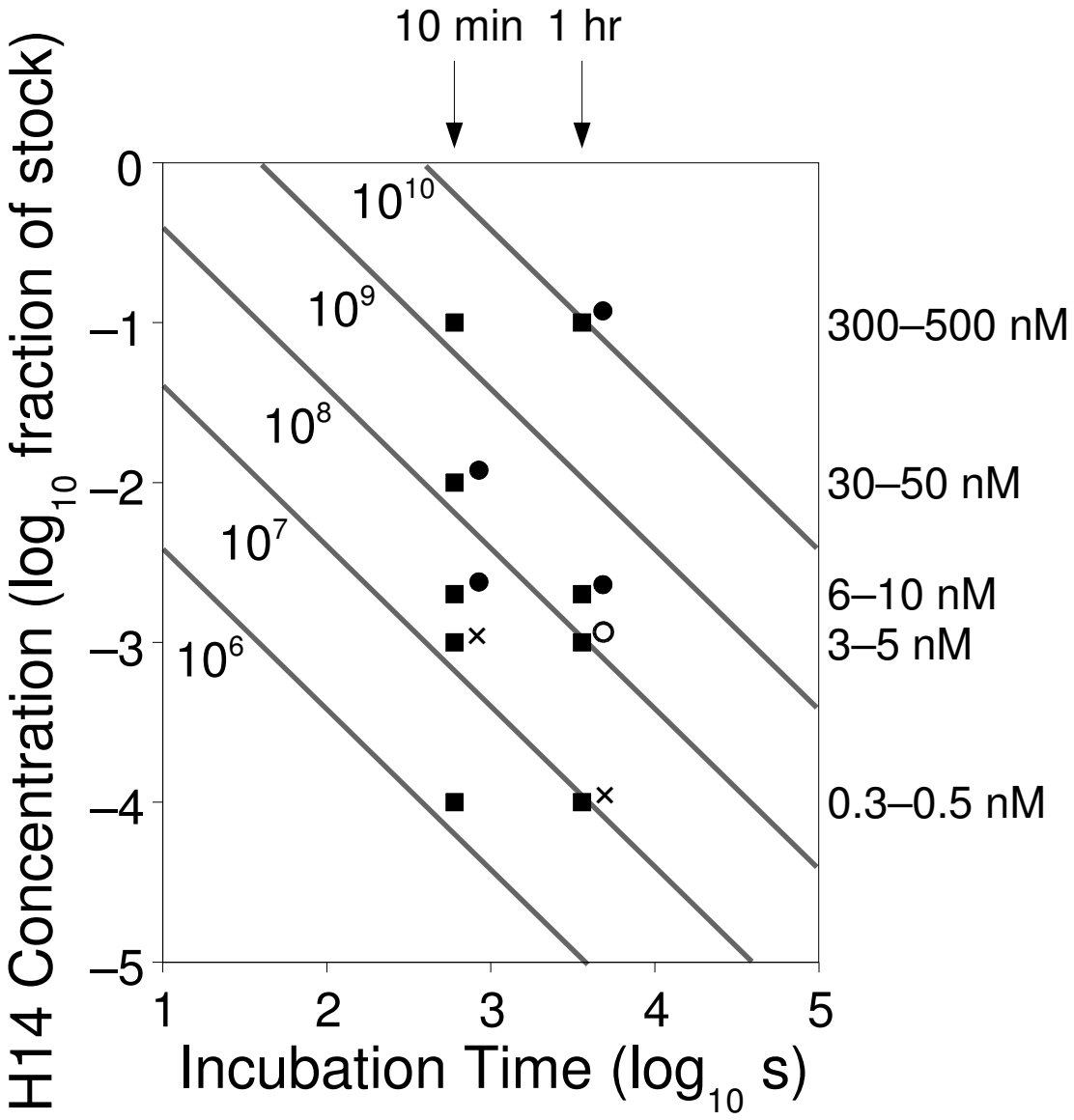
10 min
1 hr
0
–1
–2
–3
–4
–5
1
2
3
4
5
H14 Concentration (log10 fraction of stock)
Incubation Time (log10 s)
10^10
10^9
10^8
10^7
10^6
300–500 nM
30–50 nM
6–10 nM
3–5 nM
0.3–0.5 nM

Upon closer inspection, two problems emerge. The first is that the threshold between good and bad staining occurs between 10^7 and 10^8 IgM pentamers per diffusion-radius disk, which is greater than our prediction that the contour would fall between 5×10^5–1×10^7. This is probably due to the simplicity of our diffusion theory. Second, when we compare the two points closest to the threshold: the 1-hour 1:1,000 slides had faintly-stained chromosomes, but were expected to see more antibodies than those on the 10-minute 1:500 slides, which had clear staining. This is probably because the primary antibody's concentration at the 1:1,000 dilution is close to its equilibrium dissociation constant. (Jones et al., 2004) Nevertheless, overall, we see the expected crossover between good and bad staining as a function of antibody concentration and incubation time.

2.3.3 Stirring improves stain sensitivity

Comparing the banding quality of the samples that underwent incubations using the coverslip method with those that were stirred with the LOLM method for the same amount of time, we find at lower antibody concentrations that stirring reduces the fraction of slides with no banding or at best faint images in favor of those with clear images. We obtained good results for one-hour incubations with LOLM at much lower H14 antibody concentrations (1:10,000, a factor of 20 less) than we found was required for our static incubations and vastly less than has been used previously (1:5 in Lis et al., 2000) with the coverslip method. Recall that our lowest concentration should yield reaction-limited staining. This indicates that the liquid-on-liquid mixing technique can enhance the sensitivity of immunofluorescence staining at low antibody concentrations, where both diffusion and concentration are limiting.

2.4 Conclusion

The liquid-on-liquid mixing (LOLM) technique is a method for stirring thin liquid films by using an overlaid, immiscible stirrer fluid to transmit good mixing shear into the thin film. In the application described herein, the stirring has been shown to enhance the sensitivity of immunofluorescence staining of polytene chromosomes. The mineral oil layer also prevents the slide-based experiment from drying out. We anticipate that the success that this technique has demonstrated delivering antibodies in immunofluorescence staining will carry over to other slide-based assays such as histological preparations and DNA- and antibody-probe arrays.

3 FLOW VISUALIZATION EXPERIMENTS

3.1 Introduction, Background, and Theory

The immunofluorescence staining experiments described in Chapter 2 showed that the liquid-on-liquid mixing method appeared to improve the delivery of antibodies to the polytene chromosomes fixed on the glass substrate. To gain a more-detailed understanding of the mechanism of that effect and to evaluate the parameters controlling the performance of the mixer, I studied the fluid flow in the aqueous layer where the antibodies had been dispersed.

I view the efficient delivery of staining molecules to slide-bound substrates as a fluid mixing problem, and will use existing theory in this area as a guide both to describe my experiment and to interpret its results. Mixing is relevant to slide-based experiments because, as in other microfluidic reactors, diffusion limits the rate at which reactants can meet. Fluids confined in these devices' micron-scale geometries exhibit viscous effects (Ottino, 2004). Much active chemical engineering research has been directed to improving the speed and yield of bulk chemical reactions by optimizing tank and impeller shapes, but these solutions are not directly applicable to microfluidic problems.

Before proceeding, I should say that mixing is not the only scheme for overcoming diffusion in DNA hybridization reactions: using non-chaotic laminar flows, Lenigk and coworkers (2002) passed staining target solution over DNA probes printed in flat microfluidic channels; with a different geometry, Kohara and coworkers (2002, 2003) pumped staining target solution through a capillary tube containing DNA-probe-decorated glass beads (see Figure 3-1).

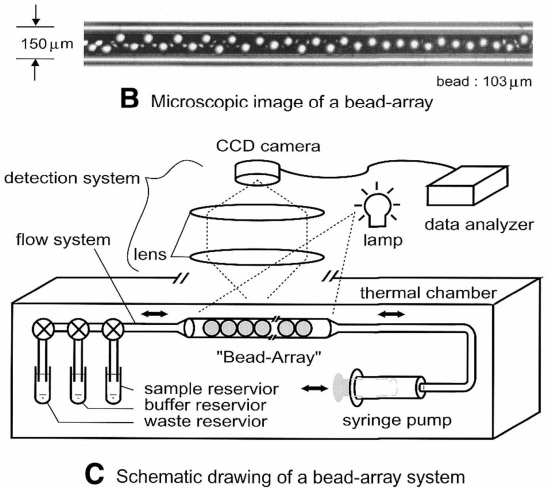

Figure 3-1: Bead-array system reproduced from Figure 1 of Kohara et al. (2002) relies on laminar pipe flow to deliver reactants to substrates.

Unlike the specialized microfluidic devices mentioned above, mixing does offer a potentially simple and cost-effective method for delivering reactants over a large slide surface and reducing local concentration differences in the reactant solution. For extensive reviews of chaotic mixing, please see Ottino (1989, 1990). Chaotic mixing guarantees exponential growth of the area of the imaginary surface separating fluid reactants. For example, if we consider the stretch-and-fold steps of the baker's map (see Figure 3-2) as a model of mixing of two reactants, each iteration doubles the length of the boundary between the two colors and halves the thickness of the stripes.

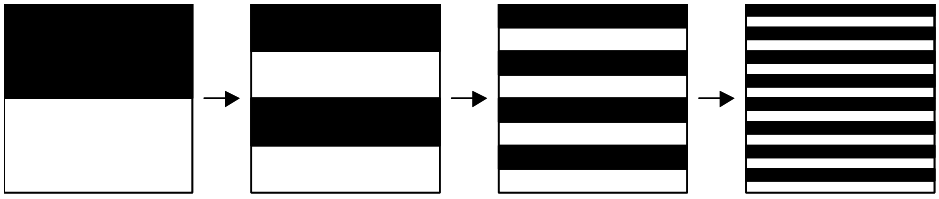

Figure 3-2: Baker's map.

The following paragraph follows Ottino (1990) and Sprott (2000). In general, periodically-perturbed chaotic systems are characterized with a spectrum of Floquet (or Lyapunov) exponents $\lambda_1 \geq \lambda_2 \geq \lambda_3 \ldots$: one exponent describing the rate of expansion or contraction for each dimension of the system. For example, the Baker's map has one positive exponent λ_1 and one negative exponent λ_2; since the map is area-preserving, $\lambda_1 + \lambda_2 = 0$. For a chaotic three-dimensional flow, one exponent must be positive. To estimate the largest real Floquet exponent in a dynamical system, ideally one could imagine two points initially separated by a small distance d_0 and then (after one iteration of the map or time step) by a distance d_1. The logarithm of the distance increase ratio, averaged over many single iterations of the map or time steps in the flow (each time resetting d_0 to point in the same direction as the d_1 resulting from the previous iteration), then estimates the largest Floquet exponent:

λ_1 = average over many map iterations or time steps of (ln (d_1 / d_0))

In bulk liquid chemical reactions, one can imagine that a well-mixed system is one where all the reactants are available to react everywhere in the desired reaction volume until the proper end of the reaction. Slide-based experiments differ from this description in that the substrate is fixed at the glass surface; it may be impossible to change the area of the fixed substrates in contact with the staining solution. At best, mixing can only bring reactants to the diffusion boundary layer above the substrate and attempt to shrink the thickness of this layer. Assuming that the reaction is fast when the reactants are available, I will consider the reaction surface to be the part of the solution that has had the opportunity to cover the substrate during the course of the experiment. This motivates the following definition of the "blend time" T — the time needed for a system to achieve the well-mixed state. A qualitative physical argument will precede the mathematical description.

Returning to the example of the baker's map, the volume of reactant solution depleted in a particular molecular species due to reaction with the substrate can be imagined as a stripe emanating from the reactive spot. Over the area of the slide, mixing should make the reactant solution uniform, erasing local depletions of reactant. How uniform is enough? The system is well mixed when the black-and-white striations are sufficiently narrow that diffusion can move reactants across the stripes in an amount of time small compared with other processes in the reaction — such as when the striation thickness is the same size as the reactive spots. The blend time is seen to be the time needed to overcome the limitations of diffusion.

The baker's map reveals the sensitivity of trajectories to initial conditions characteristic of chaotic mixing. The distance between most closely-spaced pairs of points increases exponentially with each iteration of the map. This is akin to writing:

$$d(t) = d_0 \exp(\lambda_1 t)$$

where λ_1 is the largest Floquet exponent for the chaotic mixing process. (By contrast, in diffusive mixing, the distance between closely-spaced pairs of diffusing particles increases only as the square root of time.) The constant area of the reaction chamber imposes a detailed-balance constraint equating the times for the spreading of reactants in a small area over the entire surface and for the delivery of reactants from the entire surface to every small reactive area. The blend time to overcome diffusion is equal to the time needed to separate two initially neighboring reactant particles by a distance on the scale of the reaction chamber diameter. The blend time can then be expressed as:

$$T = \ln(D / d) / \lambda_1$$

where D is the diameter of the reaction chamber and d is the diameter of a reactive microarray probe spot.

Although the extreme initial state of the baker's map may be unlike the uniform reactant solutions initially applied to slide-based assays, the blend time can be considered an upper bound on the time needed to maintain uniformity. I will use the blend time to characterize the performance of the liquid-on-liquid mixing of the thin aqueous layer.

Fluid flows can be laminar or turbulent. Laminar flows are smooth, regular, nearly non-dissipative, time-reversible. Turbulent flows contain large- and small-scale eddies, dissipating energy and accelerating diffusion. The dimensionless Reynolds number

$Re = UL/\nu$

describes fluid flows, where U is a characteristic velocity of the flow, L is a characteristic length scale of the flow, and $\nu = \eta/\rho$ is the kinematic viscosity of the fluid. Experimentally, fluid flows with $Re < 30$ tend to be laminar; turbulent flows develop when $Re > 30$. (Tritton, 1998)

The chaotic laminar flows and turbulent flows that produce good mixing are often too complicated to calculate or simulate. In these cases, the best description of the flow is a physical model of the phenomenon. Flow visualization techniques employ tracers, carried with the flow, to reveal the motions in the fluid. If the Peclet number characterizing the flow — the ratio of the fluid velocity times a characteristic length to the tracer diffusion constant — is sufficiently high, and the tracers move with the flow more than they diffuse, then the fluid motions can be seen by observing the tracers.

3.2 Methods

Here, I visualized the fluid flow in the liquid-on-liquid mixing aqueous layer by injecting small quantities of tracers into that layer and using video photography to track the tracers before and during stirring. This is similar to techniques that have been applied to chaotic flows (see, for example, Ottino 1989), and appropriate to the instant case because the aqueous layer is thin and the large-scale flows are two-dimensional. The tracers are polystyrene microspheres. The camera cannot resolve the individual microspheres; instead, I measure the area covered by the mass of microspheres and describe the initial, short-time evolution of this area.

If the transport process is purely diffusive, then every particle on the circumference of a circular dye spot can be expected to diffuse a distance:

$$\sqrt{\langle x^2 \rangle} = \sqrt{4Dt}$$

where x is the distance from the position at time $t = 0$ and D is the diffusion constant. Diffusion by molecules in the interior of the circular dye spot does not affect the apparent area of the dye spot. The area covered by the tracer particles is then:

$$\text{Area} = \pi\left(R + \sqrt{\langle x^2 \rangle} \right)^2 \approx \pi R^2 \left(1 + \frac{2\sqrt{\langle x^2 \rangle}}{R} \right)$$

where R is the initial radius of the dye spot. The approximation holds when the diffusion distance is much less than the initial radius, and the coverage of a circular dye spot grows as the square root of time. This should be valid for the pre-stir periods, because the dye spot's diameter is usually about 3 mm, and the microsphere tracer particles are expected to diffuse 0.03 mm in the ten minutes prior to the start of stirring.

On the other hand, if the transport process is chaotic, then the dye spot will be stretched and folded. However, this area-spreading experiment is not a direct measurement of the distance-increase Floquet exponent described above for two reasons:

- I cannot reset the area covered by the tracers to an infinitesimal region at each time step; nor can I resolve individual tracer particles; and
- the area spreads in two dimensions, not one.

To understand the data from the area-spreading experiment, I must adapt the mixing theory to the area-spreading experiment by addressing the differences above. To reduce the effect of the first difference, I must consider only the initial rate of area growth upon the start of stirring. To address the second difference: If we consider the dye spot area to be the cross product of two vectors, each controlled by a unique Floquet exponent (for example: one for x and one for y; or one for θ and one for r), then the initial area-increase rate will be the sum of the two largest distance-increase Floquet exponents.

$$\text{Area} \propto v_1 \exp(\lambda_1 t) \times v_2 \exp(\lambda_2 t) = (v_1 \times v_2) \exp((\lambda_1 + \lambda_2) t)$$

(In the specific case of a volume-preserving process, where in some dimension λ_1 is positive, $\lambda_2 = 0$, and λ_3 is negative, we could consider the "new area" to be just the area within one diffusion length of the exponentially-growing boundary of the dye spot. While the flow, confined to the reaction chamber, is indeed area-preserving, the algorithm (described later) measuring the dye spot area applies a threshold, which allows the two-dimensional spot area to increase.)

The area-increase Floquet exponent ($\lambda_1 + \lambda_2$) is at most twice the largest particle-separation Floquet exponent λ_1 used in the blend time definition above. I will

use the area increase due to mixing to estimate the area-increase Floquet exponent and then the blend time. For the microarray experiment, the area of the 1.9-cm-diameter reaction chamber is 1,000 times that of the 600-um-diameter microarray probe spot (see Chapter 4), so the blend time is $T = 0.5 \cdot \ln(1{,}000) / \lambda_1 \leq \ln(1{,}000) / (\lambda_1 + \lambda_2)$, where the expression with the measured area-increase Floquet exponent provides an upper bound to the blend time. Since my analysis cannot obtain the largest distance-increase Floquet exponent, we will use the upper bound as the blend time.

On longer time scales (on the order of a day), the tracers spread over the entire surface of the reaction chamber. I will ignore this because:

- the large area is hard to measure (discussed later);
- I failed to collect enough data on this behavior; and
- this behavior occurs on a time scale longer than many of the hybridization experiments.

3.2.1 Video apparatus

In slide-based assays, the aqueous reactant layer is in contact with the glass substrate. Here, the glass slide is the window through which I view the colloidal dye tracers. As shown in Figure 3-3, a CCD-based digital camera (Logitech QuickCam Pro 4000) underneath the slide holder records the image through the bottom of the slide. The camera, with a fixed 640-by-480-pixel spatial resolution, was placed so that the smaller dimension of its rectangular field of view would span most of the 0.75-inch reaction chamber diameter.

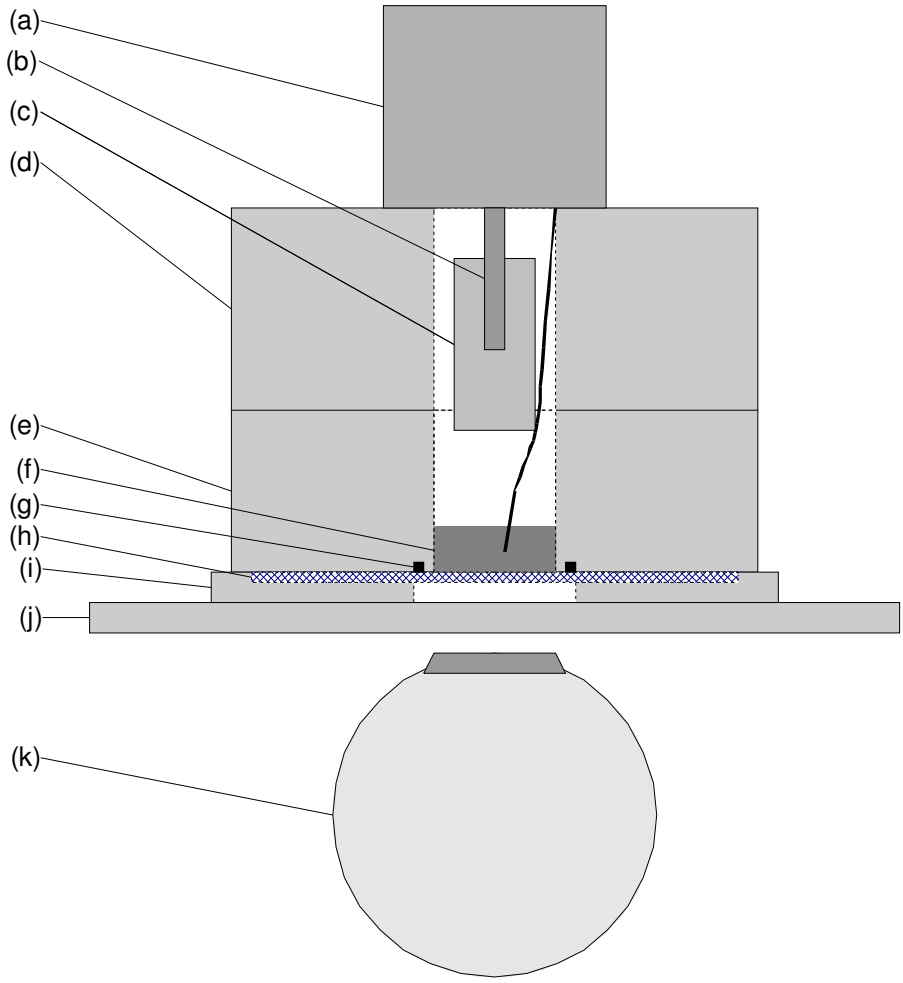

Figure 3-3: Flow visualization and liquid-on-liquid mixing apparatus. (a) Stepper motor turns (b) motor shaft holding (c) cam or paddle adapter. (d) Motor mount sits atop (e) reaction chamber confining (f) mineral oil stirred by the paddle. (g) O-ring groove not used in this experiment. (h) Glass slide sits in (i) slide holder with window for viewing slide. (j) Transparent acrylic platform holds mixer/reaction chamber/slide holder above (k) CCD camera.

To focus the camera and to check for aberrations, I drew a square grid with 2/72" pitch and placed it on a slide. The image of this square grid taken by the camera is shown in Figure 3-4. The dark circle is inscribed in the reaction chamber, and the image of the grid shows little distortion or astigmatism in that area.

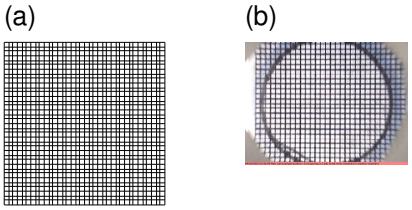

Figure 3-4: Flow visualization image calibration. (a) Grid with 2/72-inch pitch. (b) Image of the grid at the slide surface.

The images of the aqueous layer had a spatial resolution of 700 pixels per inch (0.0013 square millimeters per pixel) in the plane of the slide surface. I used a webcam software program (ISpy, available from < http://www.ispy.nl/ >) to capture time-stamped image sequences with a time resolution of 1 second.

3.2.2 Stirring chamber and paddles

The stirring chamber is the same as that used for the immunofluorescence staining experiment in Chapter 2, except that silicone vacuum grease (Corning) was used to seal the glass-acrylic gap instead of an O-ring. This was done so that the reaction chamber volume would be cylindrical: an O-ring gap would have sequestered an unknown amount of the aqueous solution, which would have led to large uncertainties in calculating the thickness of the aqueous layer. In an attempt to discover an efficient chaotic mixer, I developed several different paddles for stirring, shown in Figure 3-5.

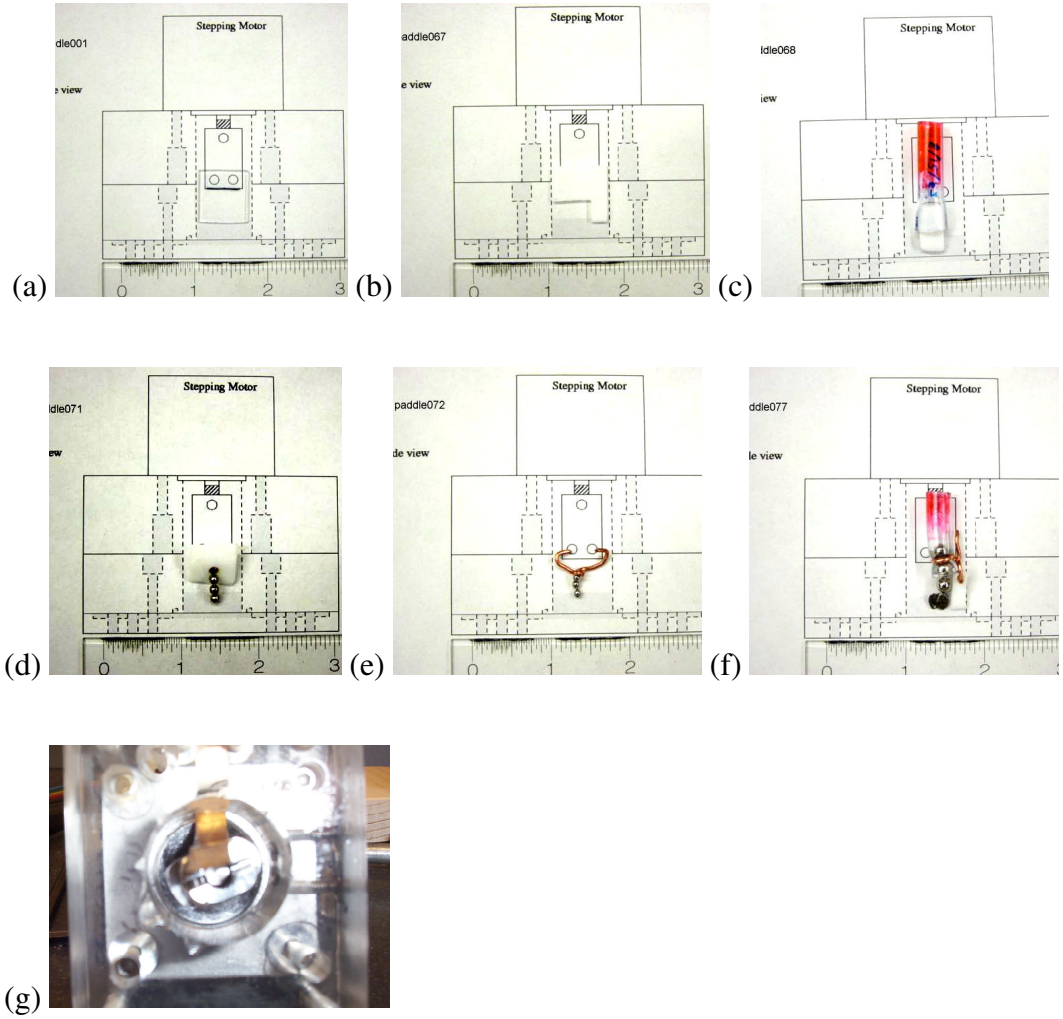

Figure 3-5: Impellers used in the flow visualization experiments, shown in side view against a 1:1 scale diagram of the reaction chamber and stirring apparatus, unless otherwise specified. (a) Acrylic paddle, used in the immunofluorescence staining experiments and flow visualization experiments fve001–fve066. (b) Teflon L-shaped paddle, used in fve067. (c) Small Teflon paddle, used in fve068–fve069. (d) Medium chain, used in fve071. (e) Small chain hanging from copper wire, used in fve072–fve074. (f) Big chain and Teflon paddle, used in fve077 and fve080. (g) Cam and beryllium-copper strip (bottom view) used in fve090–fve096 and in the microarray hybridization experiments.

The flat acrylic paddle (Figure 3-5(a)), which seemed to work so well in the immunofluorescence staining experiments, will be shown later (Figure 3-10) to exhibit an island, or stagnation zone, in the center of the reaction chamber. The L-shaped Teflon paddle (Figure 3-5(b)) was the first attempt to reduce this island, by allowing the stirred liquid to go around the paddle and hopefully through the center. The small Teflon paddle (Figure 3-5(c)) was centered away from the center of the reaction chamber, in an effort to break the symmetry of the original acrylic paddle, but this developed an island centered on the axis of stirring. The medium chain and suspended small chain (Figure 3-5(d–e)) attempted to break the symmetry of the stirring by transmitting random jostling motions (especially upon rotation reversal) into the stirred fluid. However, the chains failed to disperse the flow visualization tracers, so I attempted to combine the random motions of the chain with the large cross-section of the paddles with a hybrid stirrer (Figure 3-5(f)). This stirrer still failed to evict the island from the axis of stirring, so we finally went to the cam and non-rotating reciprocating beryllium-copper strip (Figure 3-5(g)), which successfully eliminated the stagnation zone.

3.2.3 Mineral oil

The bulk stirrer liquid used for the flow visualization and microarray experiments was light mineral oil (Fisher Scientific product number O121-1), unlike the heavy mineral oil (Fisher Scientific product number O122-1) used in the immunofluorescence staining experiments. Selected physical characteristics of these two oils and water are compared in Table 2.

Due to the large viscosity difference between the mineral oil and the water, I expect most of the shear between the motion of the paddle and the fixed slide surface to occur in the water.

Table 2: Selected physical characteristics of light and heavy mineral oil and water.

Liquid	Specific Gravity at 25°C	Viscosity at 40°C
Light mineral oil (NF/FCC)[1]	0.818–0.880 recent lots: 0.854–0.859	≤ 33.5 centistokes recent lots: 24.6–25.6 cS
Heavy mineral oil (USP/FCC)[2]	0.845–0.905 recent lots: 0.872–0.875	≥ 34.5 centistokes recent lots: 66.3–68.8 cS
Water	1.000	0.6580 cS = 0.65286 cP[3]

[1] Fisher Scientific < https://www1.fishersci.com/Coupon?cid=1336&gid=168730 > and < https://www1.fishersci.com/CofASearch?catnum=O121 >, 8 May 2005.

[2] Fisher Scientific < https://www1.fishersci.com/Coupon?cid=1336&gid=168739 >, and < https://www1.fishersci.com/CofASearch?catnum=O122 >, 8 May 2005.

[3] < http://webbook.nist.gov/ >, 8 May 2005, providing data from the International Association for the Properties of Water and Steam (IAPWS), *Revised Release on the IAPS Formulation 1985 for the Viscosity of Ordinary Water Substance*, Erlangen, Germany, 1997, 15, and Wagner W, Pruss A. 2002. "The IAPWS formulation 1995 for the thermodynamic properties of ordinary water substance for general and scientific use." J. Phys. Chem. Ref. Data 31:387–535.

3.2.4 Dye

The colloidal dye tracers were 1.0-micron (diameter) carboxylate-coated polystyrene microspheres (Polysciences), with a density of 1.05 g/cm^3 (phone conversation with Lauren Luce at Polysciences). I selected these tracers so that diffusion would not dominate their large-scale motion over the lifetime of the experiment. The diffusion constant for a 1.0-micron sphere in water is 0.43 $\mu m^2/s$. Any particle aggregation due to salt would have decreased the aggregates' diffusion constant.

3.2.5 Procedure

Each flow visualization experiment consisted of the following steps. First, vacuum grease was applied in a bead to the inner ring of the bottom surface of the acrylic reaction chamber. A clean side was placed in the slide holder, and the cylindrical reaction chamber was assembled to the slide holder, sealed to the slide with the vacuum grease. The reaction chamber was placed in a humid chamber so that a light fog formed on the exposed surface of the glass slide. A specified amount of target solution, usually 20 µl of water, was pipetted on to the glass surface of the reaction chamber. If the target solution failed to wet the slide, then the experiment was aborted. Then, 2 ml of light mineral oil was pipetted onto the target layer, so that the oil would float on the target solution, away from the glass surface. The tracer particles, usually 1 µl of stock Polysciences yellow polystyrene carboxylate beads, were pipetted directly to the target layer at the glass surface. Finally, the stirrer was assembled on the reaction chamber.

The digital camera was set to record images of the bottom of the reaction chamber. After 10 minutes, if any interfacial-tension-driven flows were observed, the

experiment was aborted. Otherwise, the stirrer was started, and images were recorded for another 10 minutes.

To increase the speed of stirring, I rewrote the stirrer software in LabVIEW so that it could run on a faster computer than was used in the immunofluorescence staining experiments. This more-sophisticated control software enjoyed all the capabilities of the original control software, such as direction reversal and speed control, plus enhancements such as randomized direction reversal and an optional duty cycle, used for the paused microarray stirring described in Chapter 4.

3.2.6 Image analysis

To measure the effect of stirring, I estimated the area covered by the tracer particles. This was done in three steps: first, I restricted the analysis to the region of the image where the tracer particles were to be found; then, I applied a threshold to select those pixels that were the same color as the tracer particles; finally, I counted the number of pixels selected by the color threshold. To facilitate and automate this process, I wrote a software program in LabVIEW using the IMAQ Vision (National Instruments) algorithm library that allows custom definition of the region of interest and color thresholds and performs instant measurement of the selected area for each image. This flexibility was necessary for two reasons: (1) occasionally the reaction chamber would move relative to the camera's field of view, and it is appropriate to choose the region of interest to follow the reaction chamber; (2) the camera used an automatic exposure setting, and the lighting conditions sometimes changed during the course of an experiment, so the color thresholds sometimes needed adjustment in order to select the correct area. I confirmed the correct behavior of the program on every image by visually comparing the selected area with the position of the dye spot. An example with the first two steps of the process is shown in Figure 3-6.

(a) 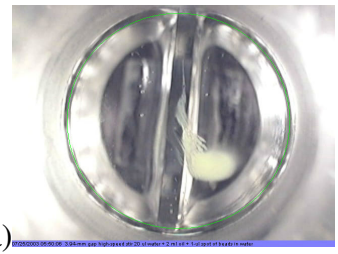 (b) 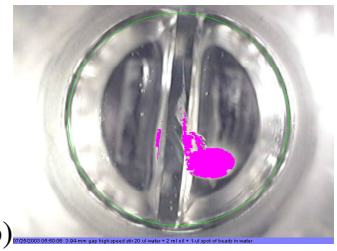 (c) 

Figure 3-6: Image analysis process. For each flow visualization experiment image, I defined a region-of-interest (a) restricting the subsequent analysis to the area within the green circle. I applied a color threshold shown in purple (b) to select the pixels covered by the yellow colloidal dye tracers. I counted the number of pixels shown in black (c) selected by the threshold and converted it to an area.

By repeating the above process for all images, I obtained the time series for the area covered by the tracer particles over the course of an experiment. Figure 3-7 shows an example resultant plot of the area covered by the tracer particles versus time.

I estimate the error in this quantitation in two ways. In the first method, I adjusted the color thresholds slightly to over- and under-estimate the region covered by the tracers. This provides an upward bound on the error at roughly 10–20%. The second method considers a sequence of images acquired during stirring and measured with a fixed color threshold. I attribute any periodic variation in the area measured in this way to exposure changes during paddle rotation. This error is smaller and is often limited to a fraction of the area of the paddle end: a few square millimeters. In either case, the area amplitude error has little or no effect on the time-of-growth, because the area is either systematically larger or smaller (in the first method) or only slightly perturbed (in the second method).

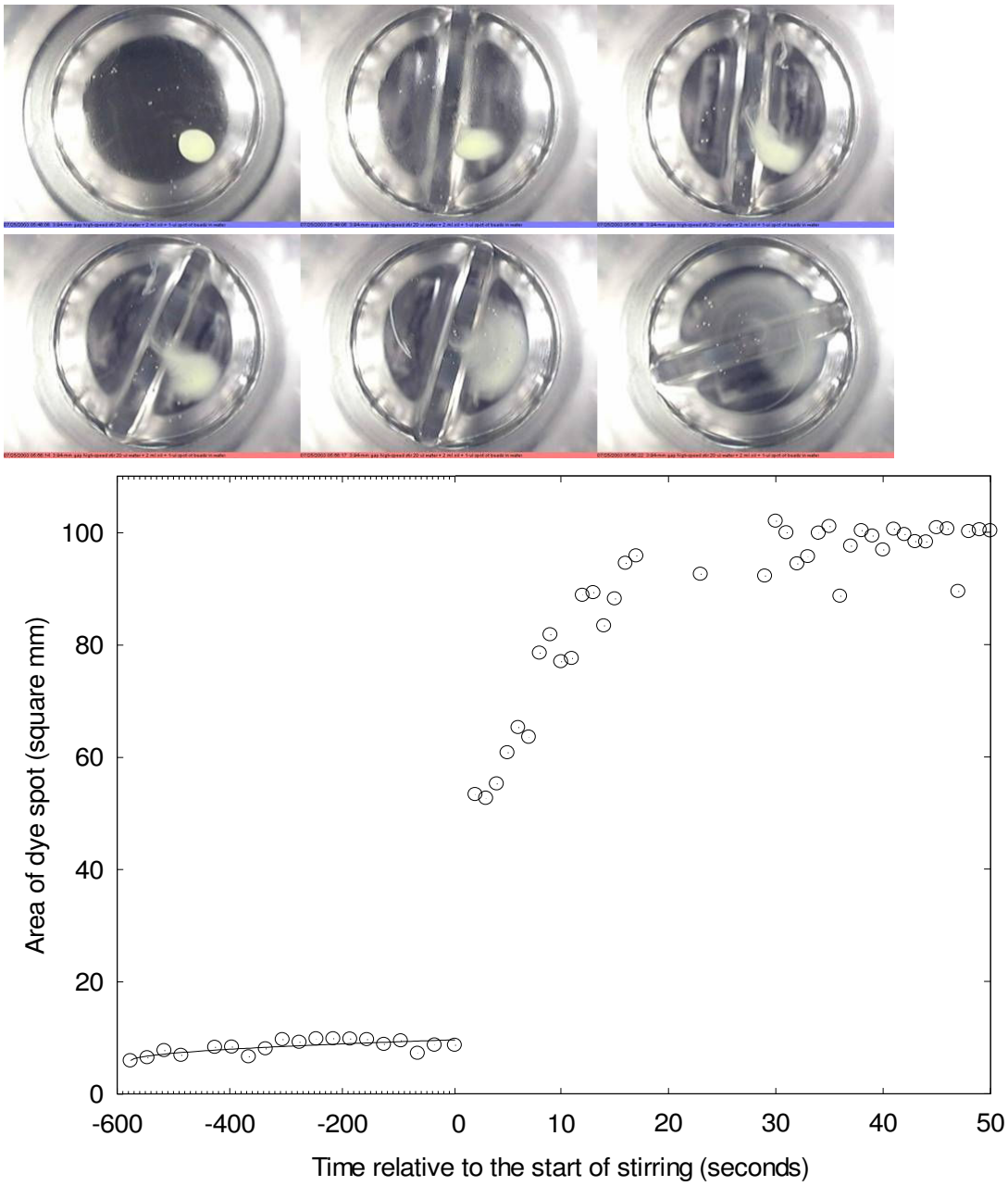

Figure 3-7: Example data (fve063). Images of dye spot taken 10 minutes, 8 minutes, and 30 seconds prior to the start of stirring and 2, 5, and 10 seconds after the start of stirring. Plot of area covered by dye spot. Data prior to the start of stirring ($t < 0$) are fit with a square-root-of-time diffusion model. Note the expanded horizontal scale to show the initial growth in area upon the start of stirring ($t > 0$).

3.2.7 Curve fitting and data analysis

I fit the unstirred data to the area diffusion expression above to calculate an effective diffusion constant. For the stirred data, I estimate the time scale of the initial increase in area through saturation, and assign this time scale to the inverse area-increase Floquet constant $1/(\lambda_1 + \lambda_2)$, even though the precise meaning of this value requires a factor-of-*e* area increase.

I investigate the initial few data points because the area covered by the dye spot cannot grow to infinity: the reaction chamber bounds the maximum area at 283 mm^2. The wide angle of the lens also causes the light-colored reaction chamber walls to limit the field of view where the area of the dye spot can be easily determined to the center 120 mm^2.

I repeated this analysis with different paddles and at different stir rates, but did not control for the initial placement of the dye spot.

3.3 Results and Discussion

I will first show the area increase data according to paddle type and stirring speed and then use the diffusion and time scale of area increase parameters to interpret the data.

3.3.1 Area increase data

3.3.1.1 Simple rotary paddle and slow stirring

The area-increase data for the paddle in Figure 3-5(a) turning at 3.4 rpm appear in Figure 3-8. Overall, we see gradual increases in the area covered by the tracers.

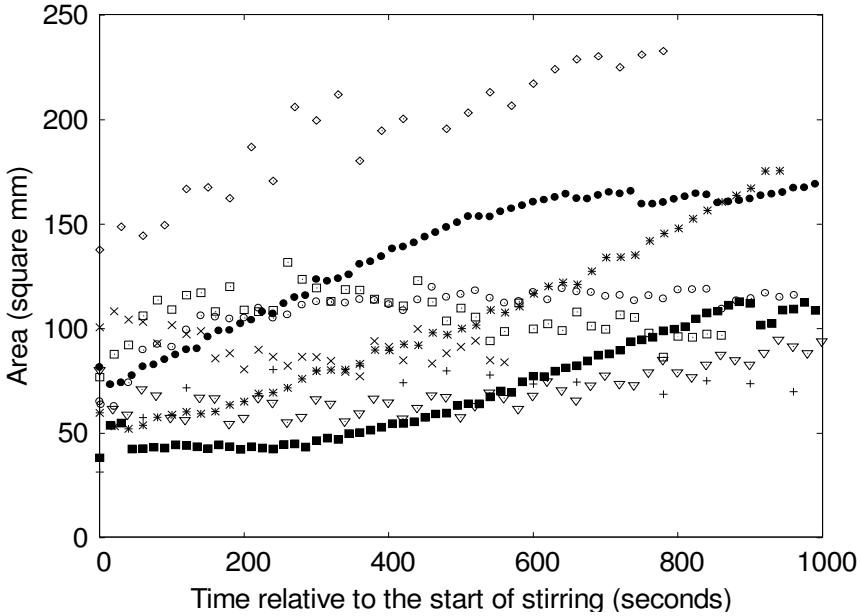

Figure 3-8: Initial experiments with acrylic paddle rotating at 3.4 rpm show very slow growth in area due to stirring. Each symbol denotes a different experimental run.

3.3.1.2 Simple rotary paddle and fast stirring

The maximum speed of the stirrer motor was increased by a factor of five, to 17 rpm. After the start of stirring, the area covered by the polystyrene microspheres shows a dramatic initial increase followed by saturation. In almost all cases, except for the first point, the average slope of the area time-series declines through the stirring phase of the experiment. These data appear in Figure 3-9.

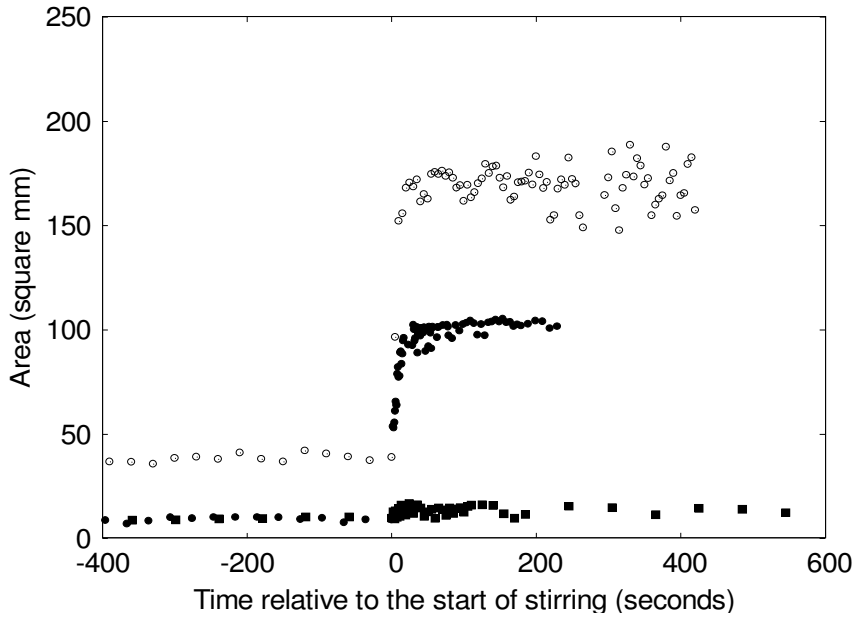

Figure 3-9: Acrylic paddle rotating at 17 rpm shows varying degrees of performance. (○) fve062 with twice the volume of dye tracers as (●) fve063, shows a dramatic increase in area upon the start of stirring. However, the area covered by the dye tracers in (■) fve066, with the same volume as fve063, fails to enjoy a similar expansion, because the paddle fails to disperse tracers in the very center of the reaction chamber (close to the axis of rotation).

In the traces where the area increases, the initial area increase occurs much faster than simply one-fifth of the time of the area increase shown in Figure 3-8, which suggests that the higher-speed stirring may be more effective at moving the tracers than the low-speed stirring. However, the flow produced in the aqueous layer by the simple paddle rotating in the mineral oil contains an island surrounding a center elliptic point, as shown in Figure 3-10.

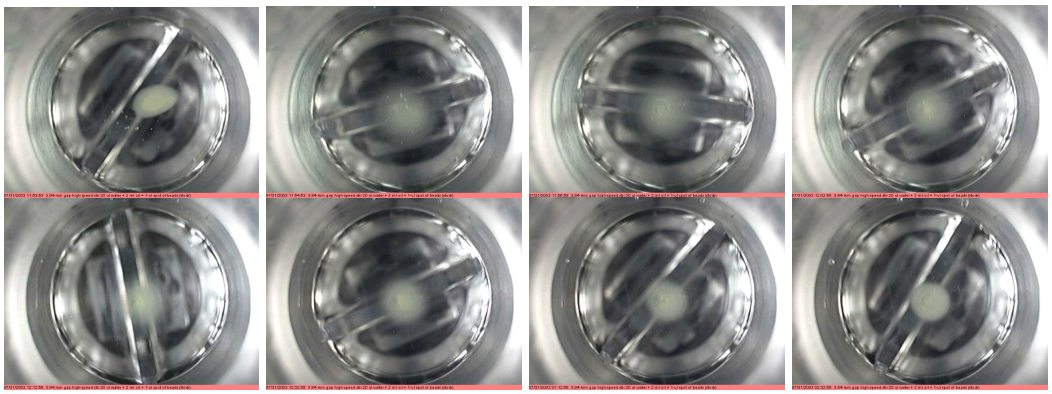

Figure 3-10: Image sequence showing center island (region of no chaotic mixing around an elliptic point) observed in experiment fve066. These images were recorded (top row) 0, 1, 3, 9, (bottom row) 19, 39, 79, and 159 minutes after the start of stirring.

This behavior accords with Ottino (1989), who notes that steady two-dimensional flows have fixed, non-intersecting streamlines, between which no mixing occurs except by diffusion. Two-dimensional flows may have elliptic points, about which the fluid circulates, and hyperbolic points, to which the fluid flows in certain directions and from which the fluid flows in other directions. (Ottino, 1989) Both types of points are shown in Figure 3-11.

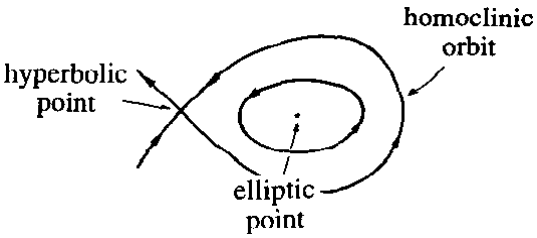

Figure 3-11: Elliptic points and hyperbolic points in a two-dimensional flow. From Ottino (1990), Figure 3(a).

Mixing can only occur when the flows change in time. I want to have a mixer with as small an island as possible.

3.3.1.3 Other stirrer designs with fast stirring

To improve the mixing, I attempted to eliminate the island by trying other stirrer designs, including swinging chains for inertial irreversibility, and randomly reversing the direction of stirring during each experiment. The paddles appearing in Figure 3-5(b–e) have tracer area-coverage data shown in Figure 3-12.

Most of these paddles showed modest tracer dispersal, probably because they had a smaller cross-sectional area to push the mineral oil. Having the paddles turn with time-randomized direction reversals still failed to eliminate the center island.

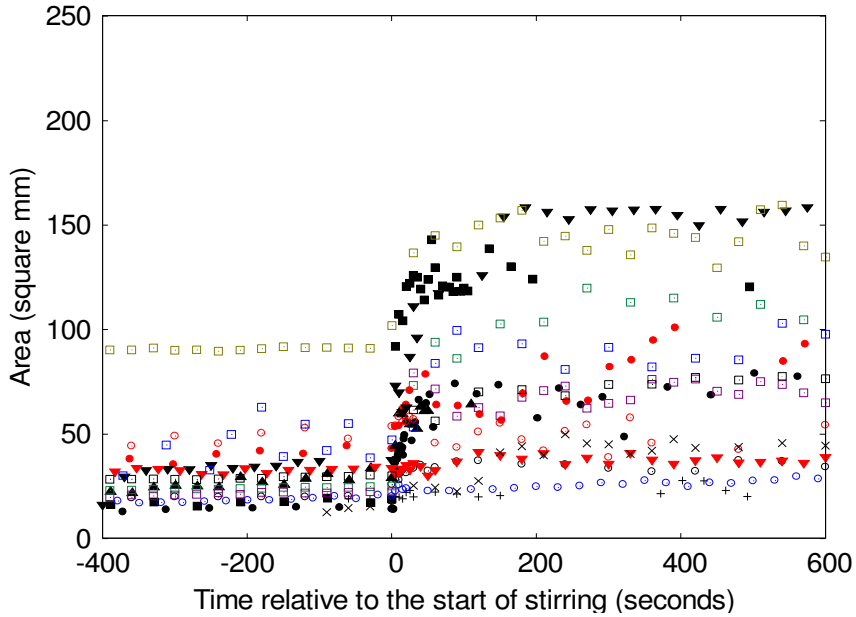

Figure 3-12: Exotic rotary paddles fail to evict islands and produce anemic area increases. (■) Teflon L-shaped paddle; (●) small Teflon bar; (+) copper arm; (▲) medium chain; (○) small chain hanging from copper wire; (▼) big chain and Teflon bar; (□) Teflon bar hanging from two copper wires; (×) Teflon bar hanging from handmade copper links.

3.3.1.4 Cam-pushed beryllium-copper strip

Finally, using the cam-pushed flexible beryllium-copper strip (shown in Figure 3-5(g)) to agitate the mineral oil in a reciprocating fashion, the island in the center of the reaction chamber was eliminated. An example image sequence with the behavior of this stirrer appears in Figure 3-13. The area-increase data appear in Figure 3-14.

Figure 3-13: Images the cam-pushed beryllium-copper strip and a dye spot 10 minutes prior to stirring and 0, 30 and 90 seconds after the start of stirring.

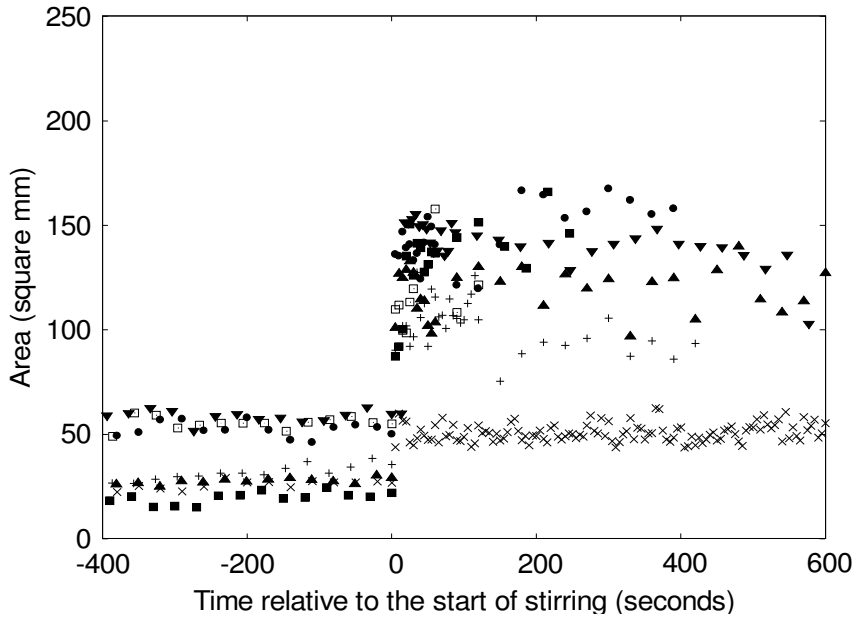

Figure 3-14: Area increase produced with the cam-pushed beryllium-copper strip is not as dramatic as with the acrylic paddle, but it eliminates the center island (dead zone). (×) initial attempt, including aluminum paddle, shows little area increase; after removal of paddle and adjustment of beryllium-copper strip, subsequent runs (+, □, ●, ■, ▲, ▼) show improved performance.

3.3.2 Diffusion

The effective diffusion constants obtained from fitting the area change before the onset of stirring varied wildly from 4.1 $\mu m^2/s$ to 1.6×10^3 $\mu m^2/s$. The fit diffusion constant for Figure 3-7 is approximately 13 $\mu m^2/s$, or more than 30 times the correct diffusion constant (0.4 $\mu m^2/s$) for the microspheres. This suggests that some process other than diffusion is contributing to the initial unstirred growth of the dye spot.

3.3.3 Stirring

I estimate the time scale of the initial increase in area covered by the tracers due to stirring, and use this time scale to describe the performance of the stirrer.

Faster stir rates produce a quicker dispersal of the tracers. At the highest stir rates (40–150 rpm), the cam-pushed beryllium-copper strip seems to mix the tracers in a time on the order of ten seconds. I approximate the time constant of the LOLM mixer with the following relationship:

$$\frac{1}{\lambda_1 + \lambda_2} = \frac{k}{f^r}$$

where the left-hand-side (expressed in seconds) is the reciprocal of the area-increase Floquet exponent, k is a constant, f is the stirring rate in rpm, and r is a constant. A fit produces k = 230 (+340/–150) [seconds · rpm^r] and $r = 0.87 \pm 0.27$, shown by the line in Figure 3-15. For f = 6 rpm, I calculate the area-increase Floquet time to be 48 (+26/–21) seconds; for f = 145 rpm, I calculate the area-increase Floquet time to be 3.0 ± 1.1 seconds.

Figure 3-15: Time-scale of area growth (in seconds, log scale), shown as a function of stir rate (rpm, log scale). (■) Acrylic paddle; (♦) Teflon L-shaped paddle; (◊) small Teflon bar; (Δ) small chain; (▲) medium chain; (□) Teflon bar hanging from two copper wires; (×) Teflon bar hanging from handmade copper links; (+) aluminum paddle and cam stirrer; (●) cam stirrer only. For clarity, data points from experiments at the same stir rate have been displaced horizontally; the true stir rates are noted on the x-axis. The fit line is (time constant) = 230 / (mixing speed)$^{0.87}$

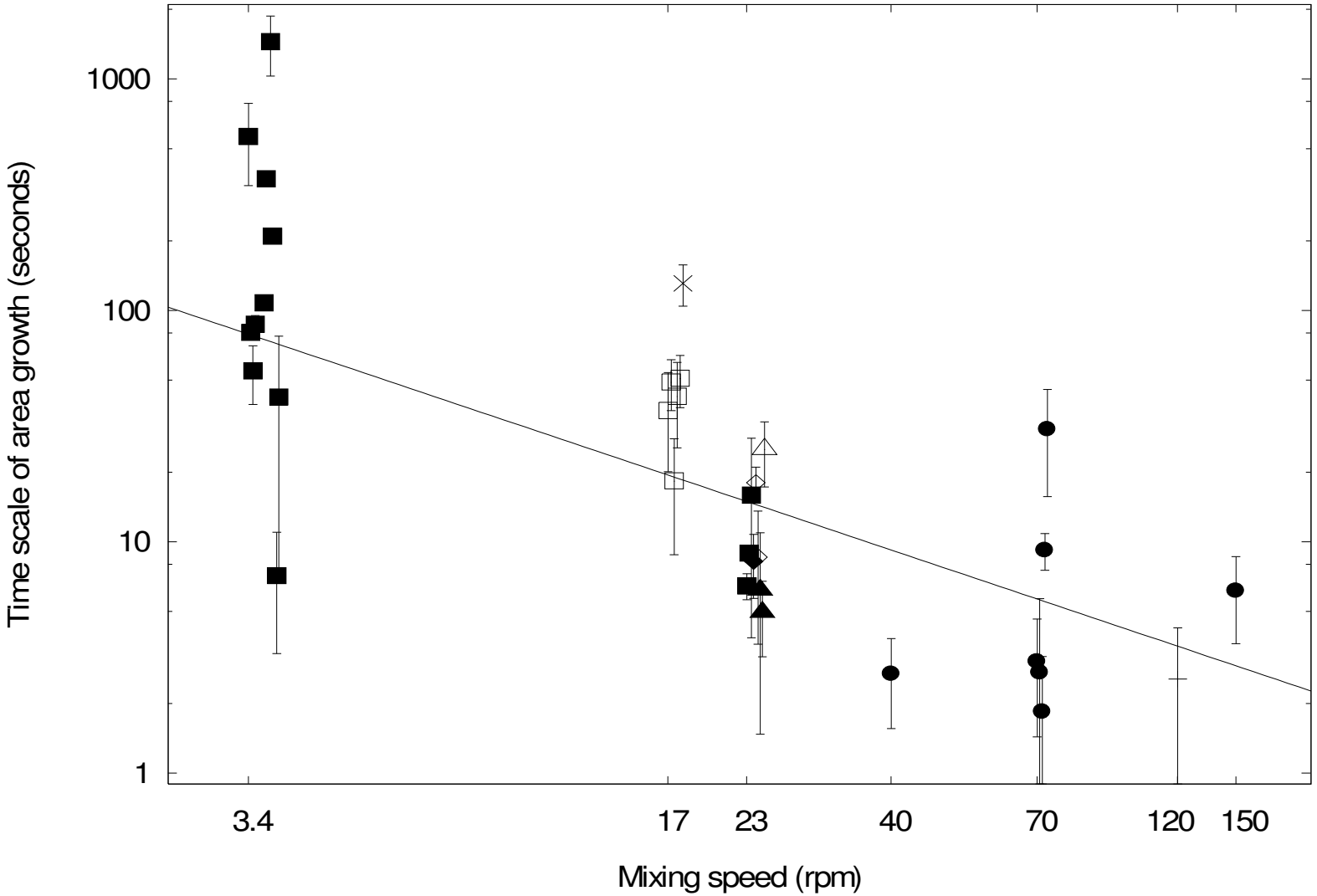
1000
100
10
1
Time scale of area growth (seconds)
3.4
17
23
40
70
120
150
Mixing speed (rpm)

3.4 Conclusions

The cam-based reciprocating stirrer appears to disperse the colloidal dye tracers almost as quickly as the acrylic paddle, and does not exhibit an island (dead zone) in the flow visualization experiments. With the estimation of the expected blend time for stirring at a variety of rates, we will proceed to the microarray hybridization experiments.

4 MICROARRAY HYBRIDIZATION EXPERIMENTS

4.1 Introduction

4.1.1 Background

Using a DNA microarray, a lone researcher can measure the quantity of tens of thousands of specific DNA molecules within 24 hours. Microarrays are substrates chemically modified to promote the specific, localized adsorption of molecules of interest. DNA microarrays rely on the property of DNA molecules to bind specifically to their complements. Every single-stranded DNA molecule consists of a linear sequence of adenine (A), cytosine (C), guanine (G), and thymine (T) nucleotides, and will form a stable double-helical structure with any single-stranded DNA molecule with the reverse-complementary sequence — where A will form two hydrogen bonds with T, and C three hydrogen bonds with G. For a review, see Wetmur (1976). This bonding process, called hybridization, was first used to identify specific DNA sequences in the 1960s. In 1975, E. M. Southern described a technique for transferring electrophoretically separated unknown DNA fragments to a membrane, immobilizing said fragments on the membrane, and exposing the membrane to radioactively-labeled defined-sequence DNA molecules, which hybridize with the complementary sequences immobilized on the membrane. The location of all matching fragments is revealed by subsequent exposure and development of a radiation-sensitive film. Based on the same principle, DNA microarrays consist of known “probe” DNA sequences immobilized in specific locations on glass substrates, to be presented for hybridization with unknown, fluorescently-labeled “target” DNA. During hybridization, the target DNA molecules interrogate the probes in parallel: if there is a match, the target binds; otherwise, the target diffuses away to another probe. After hybridization, the spatial distribution and intensity of the probe-bound target fluorescence is compared to the

original microarray design to deduce the identity and quantity of the sequences present in the target mixture.

Each of these steps contains many implicit assumptions — assumptions which, when studied further, reveal unanswered questions about the technology. For example, in most microarray protocols, the hybridization process is not given sufficient time to reach chemical equilibrium, even though non-specific hybridization occurs faster than specific hybridization (Dai et al., 2002) and longer hybridization times have resulted in better signals (Sartor et al., 2004). Post-hybridization washing can strongly affect results (Zhang et al., 2005). Some non-complementary probes bind targets more strongly than complementary probes. (Naef et al., 2002) Oligonucleotide-probe microarrays obtain results that differ from cDNA-probe microarrays. (Yauk et al., 2004) Microarrays are known to generate results that compress the quantity ratios obtained by independent methods, such as quantitative PCR. (Korkola et al., 2003) Further, the image quantitation itself is suspect: applying different analysis software to the same microarray fluorescence image obtains different estimates of gene expression level. (Tan et al., 2003; Korn et al., 2004)

Microarray technology is an active area of experimental and theoretical research. Tu and coworkers (2002) have obtained experimental bounds on the noise inherent in hybridization. Georgiadis and coworkers have used surface plasmon resonance to measure the rate of hybridization at a surface, but this technique had no spatial resolution, so only one molecular species could be measured at a time. (Georgiadis et al., 2000; Heaton et al., 2001; Peterson et al., 2001; Peterson et al., 2002) More recently, Lehr et al. (2003) have applied total internal reflection fluorescence to measure hybridization to microarrays.

The hybridization process has been modeled at various scales: the thermodynamics of the strand-to-strand binding (Held et al., 2003); the mean-field electrostatic repulsion of a field of charged probe molecules on a charged target (Vainrub and Pettitt, 2002); the adsorption of a chemical species to a reacting wall (Chan et al., 1995). Recent work treating microarray hybridization as a diffusion-reaction problem appear in Gadgil et al. (2004) and Pappaert et al. (2003a). These most recent works provide predictions on the rate at which target DNA molecules will adsorb to microarray probes, based on simple assumptions of diffusive transport and a probability of reacting. Using their methods, I modified the two-dimensional diffusion-only model applied in the immunofluorescence staining experiments (section 2.3.1) and compare with my data (section 4.3.1, especially Figure 4-8).

4.1.2 Theory

The molecular process of hybridization consists of a slow recognition and nucleation step followed by the fast zippering of complementary bases along the double helix. (Wetmur, 1976) Increasing the rate at which the target DNA molecules interrogate the immobilized probes may reduce the time for the microarray hybridization to reach chemical equilibrium. This rate depends on the concentration of the target molecules in the neighborhood of the probes, which in conventional hybridization reactions depends only on diffusion to bring target molecules to the probes. This diffusion bottleneck is severe: Stellwagen et al. (2003) report an empirical relationship for the diffusion constant for a single-stranded DNA target molecule of length N nucleotides, probably at room temperature and in water, to be:

$$D_{\mathrm{ssDNA}} = 7.38 \times 10^{-6} \times \mathrm{N}^{-0.539}\ \mathrm{cm}^2/\mathrm{s}$$

The area of a typical microarray may span as many as 10 square centimeters. The expected time for a typical thousand-base-long target molecule (from above,

$D = 1.8 \times 10^{-7}$ cm^2/s; this is a little higher than might be extrapolated from Nkodo et al., 2001) to diffuse over that surface is $t = x^2/4D = 10^7$ s, or over 100 days, while most protocols call for at most an overnight hybridization. In my experiment, the hybridization buffer has a higher salt concentration, which increases viscosity (Rant et al., 2003), and higher temperature, which decreases viscosity (International Association for the Properties of Water and Steam, 1997) than used in the studies collected by Stellwagen et al. (2003); the overall change in solution viscosity is a decrease by no more than 40%, which, while directly proportional to the diffusion time, does not change the conclusion that an overnight hybridization is far too little time for the assay to reach equilibrium.

4.1.3 Commercial Products

Schaupp et al. (2005) suggest that active mixing of the target solution improves microarray accuracy and reproducibility. Several commercial offerings claim to overcome the diffusion problem. Unfortunately, quantitative data on their performance, when available, are often not directly comparable, hard to interpret, or both. In this field, anecdotal evidence appears to be the coin of the realm, and, as the saying goes, anecdotes are not data. One of the earliest products is Ventana Medical Systems' Discovery device (Grogan et al., 1995), mentioned in Chapter 2. No quantitative data are available for the performance of this system on microarrays. Anecdotal evidence suggests that the Discovery system is effective for histology but does not help microarrays (conversation with Javed Khan, 8 February 2005). More recently, Adey et al. (2002) have described the BioMicro MAUI system, which uses a flexible bladder and a pneumatic system to drive the target solution over the surface of the array. The BioMicro MAUI product appears to reduce local target depletion and

improve sensitivity by two- to three-fold for limiting concentrations of several-hundred-base-long target DNA molecules.

Toegl et al. (2003) have described the Advalytix ArrayBooster system, which uses surface acoustic waves and a hard cover to induce mixing in the target solution. The Advalytix product literature shows that the ArrayBooster device increases the fluorescence signal compared to coverslip-method hybridizations (Figure 4-1(a)), while producing gene expression ratios similar to those obtained with the coverslip method (Figure 4-1(b)). However, the amount of increase shows great variation: hybridization to short-DNA (oligonucleotide) probe spots show much greater enhancement than hybridization to longer-DNA (PCR-product) probe spots (on average, a factor of four); different genes show different amounts of increase (a factor of 2–10 between the most-enhanced and least-enhanced at any given hybridization duration); the increase factors of any individual gene with respect to hybridization duration sometimes show large drops, unlike the monotonic increase or smooth changes expected; and different genes have different adsorption time-courses. Even if the ratios in Figure 4-1(b) are to be believed in the presence of such noise, there is no indication whether the signals with active mixing are more accurate measures of the true quantity of each target DNA species.

Also in 2003, Liu et al. of Motorola Labs described a system using vibration-induced cavitation to circulate fluid about micromachined holes in a special cover plate, reporting a "~5.3 times" increase in hybridization rate compared to the unmixed control. Pappaert et al. (2003b) describe another microfluidic implementation with a constant, direct flow, obtaining in 10 minutes the signal-to-noise ratio available from an overnight (16-hour) static hybridization.

Figure 4-1: Product literature for the Advalytix ArrayBooster device reveals uncertainty of hybridization signal with, without, or both with and without active mixing. (a) Ratio of hybridization signal obtained with active mixing with the Advalytix ArrayBooster product to that obtained without active mixing at five hybridization durations (8 hr, 20 hr, 32 hr, 48 hr, and 72 hr) for PCR-product microarray probe spots (1–10) and oligonucleotide probe spots (11–20). (Reproduced from Figure 2 in "Hybridization Efficiency of PCR-Product vs. Oligonucleotide Microarrays", < http://www.advalytix.com/application_notes/PCR_Oligo.pdf >, accessed 19 April 2005.) Since most of the factors are greater than unity, mixing appears to increase the hybridization signal. However, the amount of increase shows great variation over time, gene identity, and probe length. (b) Gene expression ratios obtained with cover glass and with active mixing, meant to show that mixing has no large effect on gene expression ratios. (Reproduced from Figure 5 in "Enhancing Results of Microarray Hybridizations Through Microagitation", by Andreas Toegl, Roland Kirchner, Christoph Gauer, and Achim Wixforth, (2003) *Journal of Biomolecular Techniques* 14:197–204.) It is not obvious which method produces more accurate results.

(a)

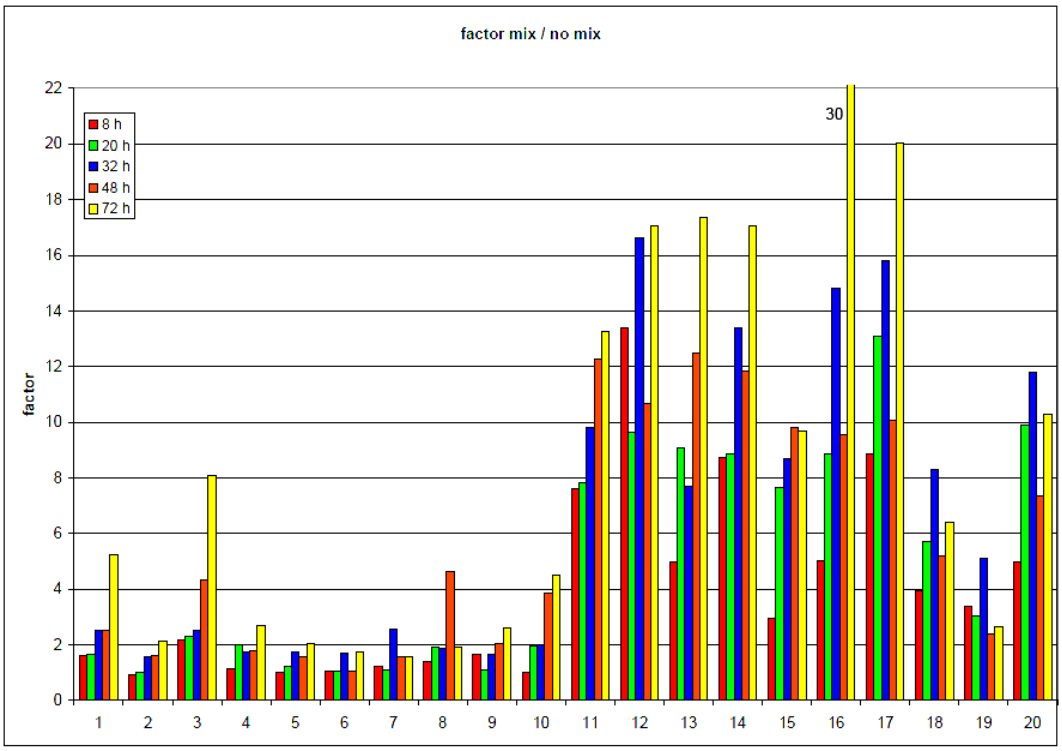
factor mix / no mix
factor
8 h
20 h
32 h
48 h
72 h
30
0
2
4
6
8
10
12
14
16
18
20
22
1
2
3
4
5
6
7
8
9
10
11
12
13
14
15
16
17
18
19
20

(b)

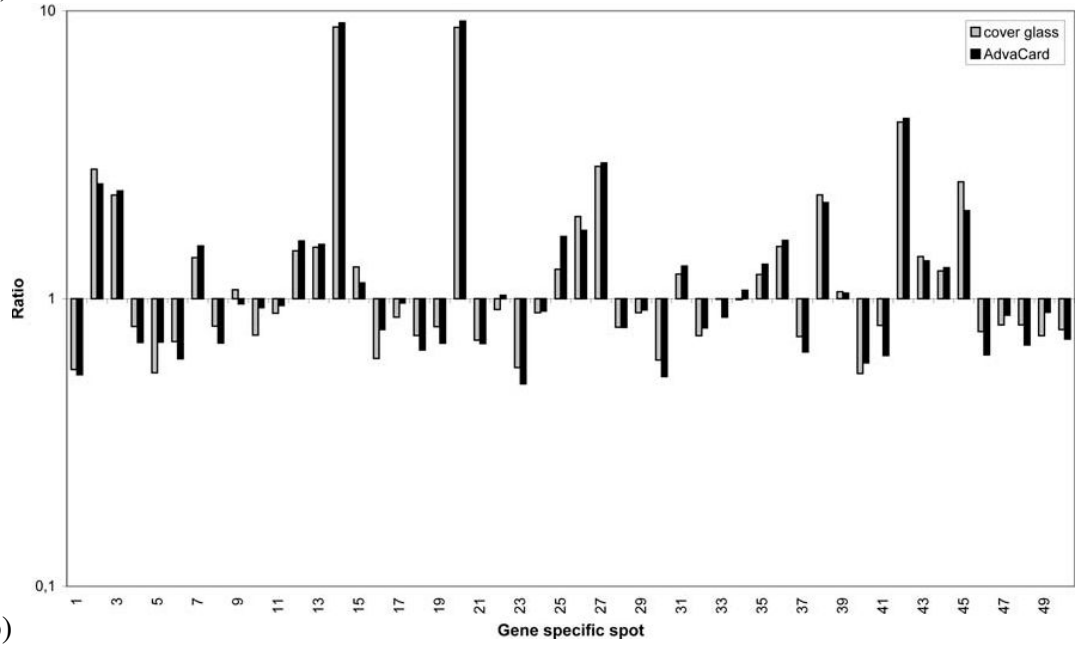
cover glass
AdvaCard
Ratio
10
1
0,1
1
3
5
7
9
11
13
15
17
19
21
23
25
27
29
31
33
35
37
39
41
43
45
47
49
Gene specific spot

The recently introduced TECAN system performs active convection of the target solution. In comparison to hybridizations performed under a cover glass, hybridizations performed with the TECAN system show an increased signal-to-background ratio, but a lower absolute signal. (communication with David Lin, relayed by Carl Franck, in e-mail dated 4 April 2005)

After the apparent success of the liquid-on-liquid mixer for improving the immunofluorescence staining of polytene chromosomes, I wanted to make a quantitative measurement of the effect. The following will describe my experiments applying the liquid-on-liquid mixer to small-scale microarrays.

4.2 Methods

4.2.1 Strategy

I wanted to assess the performance of the liquid-on-liquid mixing (LOLM) stirring technique when applied to microarrays. The chief performance metrics I want are the efficiency of the process, as a measure of the achievement of chemical equilibrium, the sensitivity and specificity of the assay, and the noise.

To do this, I produced microarrays patterned with positive and negative control probe spots, and subjected these microarrays to various hybridization conditions with fluorescent target DNA molecules, with stirred and unstirred reactions in parallel. To test the hypothesis that stirring-induced shear (see section 4.2.2) might inhibit the hybridization reaction, I used continuous stirring and pulsed stirring in separate experiments. The pauses were selected to provide enough time for hybridization between short periods of large-scale stirring. Following hybridization, these microarrays were washed and scanned. The scanner signal measures the intensity of the surface-bound fluorescence; this intensity estimates the number of bound target molecules. To calculate the efficiency of binding, the fluorescence intensity of the

specifically bound target molecules is compared to the expected total fluorescence intensity of all the target molecules that were present in the hybridization reaction. Finally, the efficiency for the stirred hybridization is compared to that for the unstirred hybridization.

This procedure avoids or controls for some of the problems described in the introduction: I used a known quantity of a single gene in my experiments, I ran stirred and unstirred hybridizations side-by-side on physically separate areas of the same microarray slide, and I washed, scanned, and analyzed the microarrays in a consistent manner.

4.2.2 Selection of stir rate and rationale for studying pauses

We do not know the precise effect of shear on the hybridization process. Van Ness and Hahn (1982) found that mixing could improve the extent of renaturation of high-complexity DNA; but physical intuition suggests that too high a rate of shear could prevent the initial recognition and nucleation of DNA hybrids. Flow visualization experiments with the cam-based stirrer (unpublished data courtesy of Jason Carpentier) indicate that appreciable large-scale fluid motions are seen at continuous stir rates exceeding 6 rpm; the maximum speed attained with the experimental setup was 145 rpm. Benjamin Smith estimated the shear gradient at the surface of the microarrays in the liquid-on-liquid mixing (LOLM) reaction chamber to be:

$$\sigma = 190\frac{f}{V}$$

where σ is the shear rate in inverse seconds, f is the stir rate in rpm, and V is the volume of the aqueous target layer in µl. Typically, the LOLM experiments have V = 200 µl and f = 6 or 145 rpm, which produces σ = 5.7 or 138 s^{-1} respectively. This

rate may be significant if its inverse is the same order of magnitude as the dominant time constant for relaxation of the single-stranded target DNA molecules (elongated polymer) into a random coil: in that case, the stirring may cause all the target molecules to be stretched, which may in turn inhibit the DNA nucleotide recognition step. This dominant time constant τ in seconds is estimated (Cantor and Schimmel, 1980a, pp. 656–658):

$$\tau = \frac{M^{5/3}}{RT\lambda k^{2/3}/\eta_0}$$

where M is the molecular weight of double-stranded DNA in Daltons (long enough to be in the coil regime), R is the ideal gas constant in cgs units (equal to Boltzmann's constant times Avogadro's number), T is the temperature in kelvin, λ is a constant equal to 1/0.451, k is a constant equal to 19.8, and η_0 is the viscosity of the solution in poise. At 50°C, in the hybridization buffer (500 mM salt), the denominator is 8.7×10^{13}. I interpret the mass M in the expression above to represent an equivalent number of persistence lengths; since I used single-stranded DNA, which has a much shorter persistence length than double-stranded DNA, I must rescale the mass of the ssDNA by the persistence length ratio before calculating the time constant. The persistence length of dsDNA is "roughly 450 Å" (Cantor and Schimmel, 1980b, p. 1036); ssDNA is more appropriately modeled as a freely-jointed chain, but I will say that its persistence length is on the order of a single nucleotide, or 5 Å, which is some 90 times smaller. The mass of a persistence length of dsDNA is (450 Å / 3.4 Å/bp * 600 Da/bp) = 7.9×10^4 Da, and the mass of a persistence length of ssDNA = (300 Da/nt) = 300 Da. The 981-nt ssDNA target molecules have the same number of persistence lengths as a 128-kb dsDNA molecule, of mass some 7.6×10^7 Da, with a relaxation time constant of 0.16 s.

The product $\sigma\tau$ is 0.9 for the 6-rpm LOLM stirring and 22 for the 145-rpm LOLM continuous stirring: shear likely extends the ssDNA target molecules in the 145-rpm stirring case, and shear may be significant in the 6-rpm case. In case even the 6-rpm continuous stirring applies enough shear to inhibit the hybridization reaction, I explored stirring with pauses. I wanted to retain at least the large-scale fluid transport available to 6-rpm continuous stirring, so, in the 145-rpm paused stirring experiments, I applied repeated cycles of 145-rpm stirring for 1 second followed by no agitation for 20 seconds (over 100 relaxation time constants), which I expect should provide sufficient time for hybridization, while generating large-scale fluid motions at the same average rate as the 6-rpm continuous stirring.

4.2.3 Dual reaction chamber

To perform hybridizations with the liquid-on-liquid mixing (stirring) in parallel with an unstirred control, I designed and constructed a dual reaction chamber. This was a modification of the slide holder used in the immunofluorescence staining and flow visualization experiments. The acrylic block with the centered reaction chamber (shown in profile in Figure 3-3 on page 28) was replaced by a block with two reaction chambers, one at the end, to be used for the unstirred reaction, and one closer to the center, for the stirred reaction, as shown in Figure 4-2. The motor mount was shifted by 1/4" to be aligned with the closer-to-center reaction chamber.

The unstirred control was always prepared in the same manner as the liquid-on-liquid mixing reaction, but the mineral oil was not agitated. Flow visualization tests showed that the mechanical coupling of the motor and paddle to the unstirred control produced insignificant fluid flow. (unpublished data courtesy of Jason Carpentier)

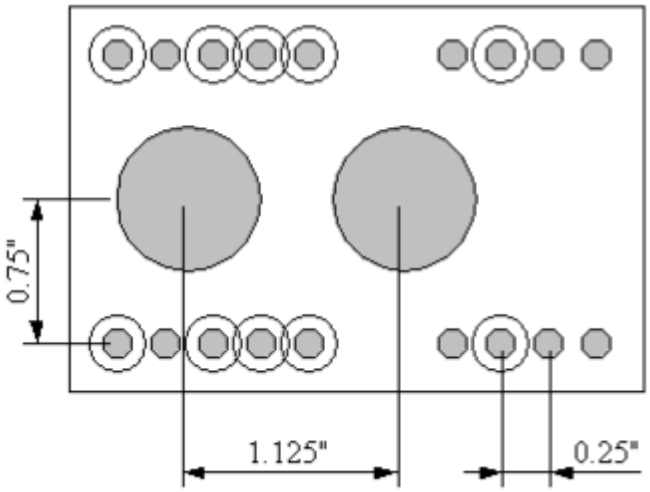

Figure 4-2: Diagram of dual reaction chamber design. The large disks in the center represent the reaction chambers. The smaller circles along the top and bottom edges represent potential screw-holes for attaching the stirrer motor mount and the reaction chamber to the slide holder.

4.2.4 Microarray production

I selected two different 981-nt dsDNA sequences from the Escherichia coli genome, named sfhB and b1771. Of the fewer than ten 981-nt genes or putative genes in the E. coli genome, sfhB and b1771 shared the least amount of common sequences. Their sequences appear in Table 3 and are available from the public genome databases.

Using standard protocols, Shannon Guiles amplified the two nucleotide sequences by the polymerase chain reaction (PCR), purified the PCR products with a pH-dependent DNA-binding column (QIAQuick PCR Purification Kit, standard protocol with a microfuge), and concentrated the purified DNA by precipitation in ethanol.

Table 3: Sequences of the two 981-bp probe genes printed on the microarray.

The top row gives the reverse complement of putative gene b1771, which has 47.8% GC content and was the positive control; the bottom row gives the reverse complement of gene sfhB, which has 52.8% GC content and was the negative control. The primer regions used to amplify the genes through PCR are underlined. The largest five alignments are highlighted. The sequences were downloaded from
< http://www.ncbi.nlm.nih.gov/entrez/viewer.fcgi?val=49175990&itemID=7011&view=gbwithparts > and
< http://www.ncbi.nlm.nih.gov/entrez/viewer.fcgi?val=26108223&itemID=537&view=gbwithparts >, both accessed 28 August 2005.

b1771 (reverse complement)

ATGAAAAAGA TACCTTTAGG CACAACGGAT ATTACGCTTT CGCGAATGGG GTTGGGGACA TGGGCCATTG
GCGGCGGTCC TGCATGGAAT GGCGATCTCG ATCGGCAAAT ATGTATTGAT ACGATTCTTG AAGCCCATCG
TTGTGGCATT AATCTGATTG ATACTGCGCC AGGATATAAC TTTGGCAATA GTGAAGTTAT CGTCGGTCAG
GCGTTAAAAA AACTGCCCCG TGAACAGGTT GTAGTAGAAA CCAAATGCGG CATTGTCTGG GAACGAAAAG
GAAGTTTATT CAACAAAGTT GGCGATCGGC AGTTGTATAA AAACCTTTCC CCGGAATCTA TCCGCGAAGA
GGTAGCAGCG AGCTTGCAAC GTCTGGGTAT TGATTACATC GATATCTACA TGACGCACTG GCAGTCGGTG
CCGCCATTTT TTACGCCGAT CGCTGAAACT GTCGCAGTGC TTAATGAGTT AAAGTCTGAA GGGAAAATTC
GCGCTATAGG CGCTGCTAAC GTCGATGCTG ACCATATCCG CGAGTATCTG CAATATGGTG AACTGGATAT
TATTCAGGCG AAATACAGTA TCCTCGACCG GGCAATGGAA AACGAACTGC TGCCACTATG TCGTGATAAT
GGCATTGTGG TTCAGGTTTA TTCCCCGCTA GAGCAGGGAT TGTTGACCGG CACCATCACT CGTGATTACG
TTCCGGGCGG CGCTCGGGCA AATAAAGTCT GGTTCCAGCG TGAAAACATG CTGAAAGTGA TTGATATGCT
TGAACAGTGG CAGCCACTTT GTGCTCGTTA TCAGTGCACA ATTCCCACTC TGGCACTGGC GTGGATATTA
AAACAGAGTG ATTTAATCTC CATTCTTAGT GGGGCTACTG CACCGGAACA GGTACGCGAA AATGTCGCGG
CACTGAATAT CAACTTATCG GATGCAGACG CAACATTGAT GAGGGAAATG GCAGAGGCCC TGGAGCGTTA
A

sfhB (reverse complement)

ATGGCACAAC GAGTACAGCT CACTGCAACG GTGTCCGAAA ACCAACTCGG TCAACGCTTA GATCAGGCTT
TGGCCGAAAT GTTCCCGGAT TATTCACGTT CGCGAATAAA AGAATGGATC CTCGACCAGC GAGTGCTGGT
TAACGGCAAA GTTTGTGATA AGCCGAAAGA AAAAGTATTG GGTGGCGAGC AGGTTGCCAT CAACGCTGAG
ATTGAAGAAG AAGCGCGTTT TGAACCGCAG GATATCCCGC TGGATATCGT CTATGAAGAT GAAGACATTA
TTATCATTAA TAAACCGCGC GACCTGGTGG TACATCCTGG CGCGGGTAAC CCGGATGGCA CGGTACTGAA
TGCGTTGCTT CATTACTATC CACCCATTGC CGATGTACCG CGTGCGGGCA TCGTCCATCG TCTGGATAAA
GACACCACTG GCCTGATGGT TGTGGCAAAA ACCGTTCCGG CTCAGACGCG TTTAGTCGAA TCTTTGCAAC
GGCGTGAAAT TACTCGTGAG TATGAAGCGG TGGCGATTGG TCATATGACC GCAGGTGGCA CGGTGGACGA
GCCAATCAGT CGCCACCCGA CCAAACGTAC CCATATGGCG GTGCATCCGA TGGGCAAACC AGCGGTGACT
CACTATCGCA TCATGGAACA CTTCCGTGTG CACACGCGTC TGCGGTTGCG TCTGGAAACT GGACGTACGC
ACCAGATCCG CGTGCATATG GCCCATATCA CTCATCCGCT GGTGGGCGAT CCGGTTTATG GTGGCCGTCC
GCGTCCGCCA AAAGGTGCTT CGGAAGCATT TATCTCCACG CTGCGTAAGT TTGACCGCCA GGCGCTACAT
GCAACCATGC TGCGTCTTTA TCACCCGATC TCCGGCATCG AAATGGAATG GCATGCGCCT ATTCCACAAG
ATATGGTGGA GCTGATTGAG GTGATGCGCG CCGATTTCGA AGAACATAAG GATGAAGTGG ACTGGTTATG
A

To print the DNA molecules onto the glass slides, Shannon Guiles separately resuspended both ethanol-precipitated purified PCR products to a final concentration of 0.1 µg/µl in 50% v/v DMSO.

(Note: This was one option provided for the Corning GAPS II slides (see Appendix, section 9.2.2.1). Paul Debbie had told us that the DMSO-based printing solution gives excellent probe spot uniformity and denatures the double-stranded DNA, whereas other salt-based printing solutions tend to produce “coffee rings” when dry. Patricia J. Koutz, Director of Research and Development at V&P Scientific, the maker of the printer, had suggested adding a little detergent to the DMSO solution to improve printing (phone conversation, 21 January 2004), but the instructions with the Corning slides explicitly recommended against this, explaining that detergents would interfere with the bonding of the probe DNA to the surface.)

I numbered the Corning GAPS II slides serially as "lh*nnn*", where the *nnn* is a three-digit number. Each slide was used for a single hybridization experiment, so the slide designator uniquely identifies the hybridization conditions. Since I performed only 64 hybridization experiments, these experiments appear as only two-digit numbers in Figure 4-6.

I used the V&P Scientific VP478 pin printer to print DNA solution onto the Corning GAPS II slides in the pattern shown in Figure 4-3. Each fixed probe spot was estimated by the manufacturer to contain 3 nl of DNA solution; other researchers have found that the delivered volume was 14 nl (e-mail dated 14 March 2005 from Patricia J. Koutz, Director of Research and Development at V&P Scientific). We will use the latter value. Since the concentration of the DNA in the DMSO printing solution was 0.1 µg/µl, each 14-nl probe spot contained 1.4 ng of DNA, or 2.3 fmol of each strand. Each "L"-shaped group of probe spots consists of three subgroups of four

positive-control probe spots and four negative-control probe spots, arranged so that both positive and negative control probe spots would placed at various distances from the center of the reaction chamber. There are two "L"-shaped groups because I wanted to perform hybridizations stirred with the liquid-on-liquid mixing technique in parallel with unstirred control hybridizations. Each set of 12 positive- and negative-control probe spots presents a total of 28 fmol of DNA to bind the target. I will call the probe spots in the group closer to the end of the slide “unstirred”, and the probe spots in the group closer to the middle of the slide “stirred”, no matter whether each slide’s particular hybridization condition included stirring. Keep in mind that the unstirred side of each sample was not always hybridized with the coverslip method.

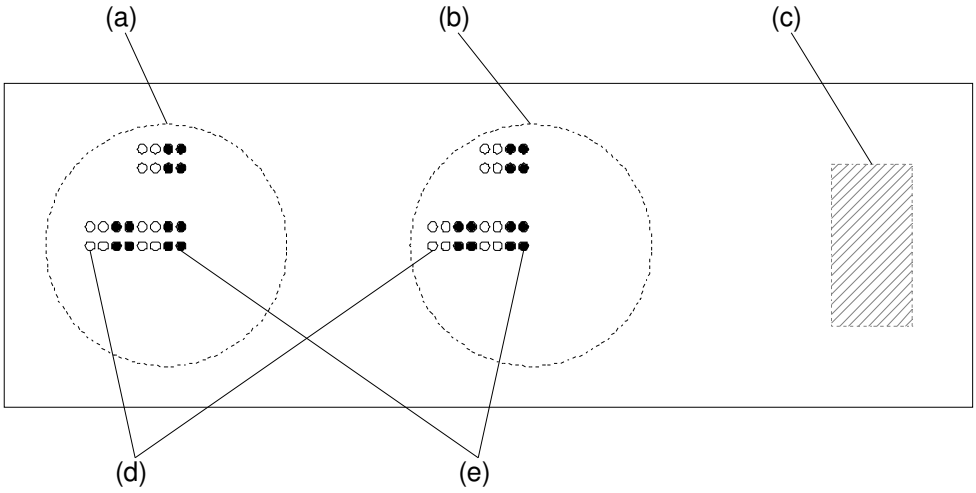

Figure 4-3: Microarray design. Labels denote: (a) unstirred reaction chamber area; (b) stirred reaction chamber area; (c) slide label (on reverse face of slide); (d) negative control probe spots; (e) positive control probe spots. Figure is drawn to scale.

Following the Corning GAPS II slide protocols (see Appendix beginning on page 123), I allowed the printed slides to dry slowly in a humid environment, rehydrated and snap-dried the slides, and exposed the slides to a 300 mJ dose of UV light to immobilize and crosslink the deposited DNA with the gamma-amino-propyl-silane surface. From this step forward, I will refer to the slides with the printed and immobilized probe DNA spots as microarrays. The microarrays were optionally scanned as a check on the uniformity of printing and then stored in desiccation at room temperature.

I printed the slides in batches of ten or twenty. The DMSO in the printing solution has intrinsic fluorescence (Martinez et al., 2002), which can be detected with a microarray scanner. Scans were performed as described in the Appendix starting on page 123. Figure 4-4(a) shows a fluorescent image of a typical printed microarray.

The GenePix Pro software segments the image into "feature" and background areas, and reports descriptive statistics on the pixel intensities in each area. We will refer to the pixels in these feature regions as fluorescent spots. I take the median fluorescent spot intensity and subtract the median local background intensity, and this local-background-subtracted median intensity for each individual fluorescent spot is shown in Figure 4-5, along with the mean for each group of 12 positive- and negative-control fluorescent probe spots on the stirred and unstirred sides of each slide.

Both positive and negative control probe spots fluoresce, but with different intensities. Further, probe spots printed in different 10-slide printing batches had different levels of fluorescence, which suggests that the amount of DNA deposited on the slides may have varied between printing batches. This variation makes it harder to perform slide-to-slide comparisons, but usually we will be comparing the stirred and unstirred sides of the same slide.

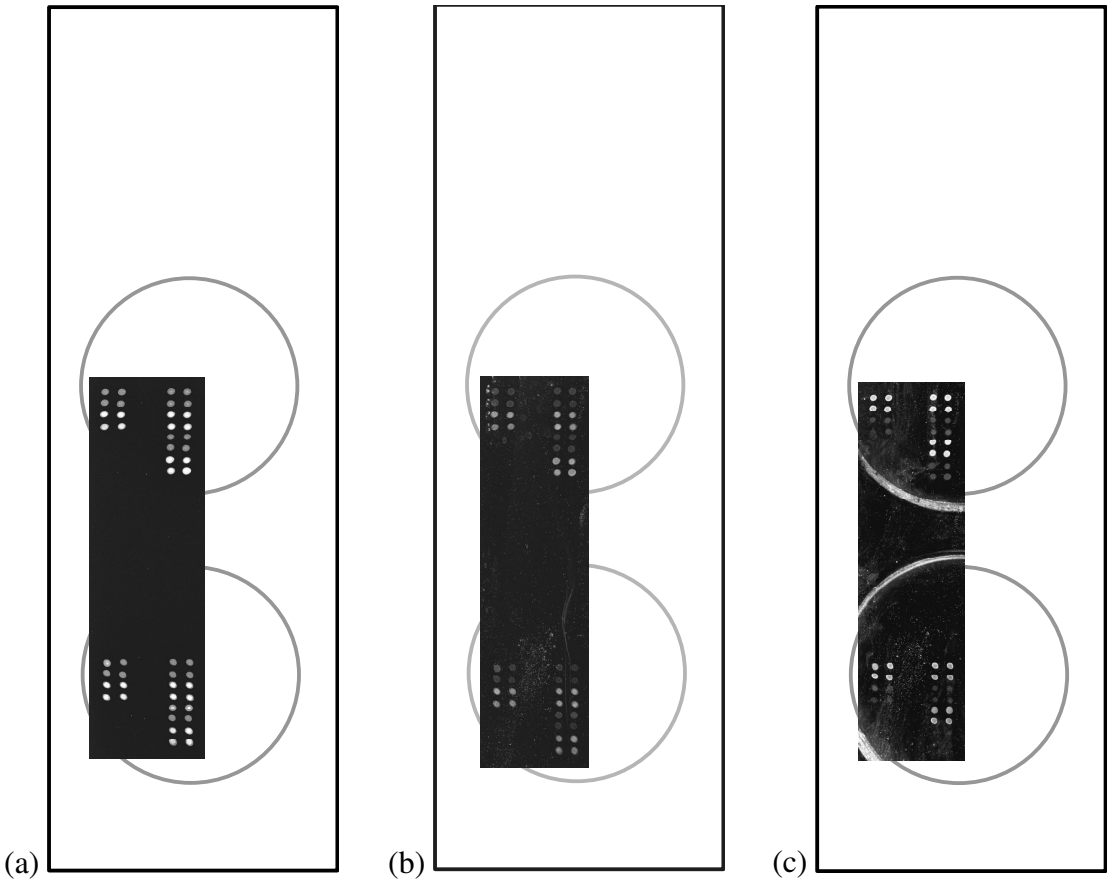

Figure 4-4: Example excerpt images of microarray #33 (a) after printing and immobilization; (b) after a no-DNA, no-BSA pre-hybridization wash; (c) after hybridization and washing. Contrast has been adjusted in each case. Observe that the negative controls appear to have higher intensities in (a) and (b), but the positive controls dominate in (c). The approximate positions of the dual reaction chambers are drawn for reference. The scan region was always selected to cover all the probe spots plus a margin.

Figure 4-5: Printing uniformity. Scans of microarrays after the DNA probe spots have been immobilized but before exposure to the fluorescently-labeled targets reveals large signals at the probe spots, possibly intrinsic fluorescence of residual DMSO in the printing solution. These data have been normalized and corrected for power differences as described in section 8.3.4, starting on page 133.

Each small dot represents the median pixel intensity of a single fluorescent spot: blue for positive controls (dark blue after washing) and red for negative controls (dark red after washing). The upward- and downward-pointing open triangles show the arithmetic means of each set of 12 positive- and negative-control fluorescent spots, respectively. Each slide has a total of 48 probe spots, and they are given in the order: stirred-side positive control, stirred-side negative control, unstirred-side positive control, unstirred-side negative control. The filled triangles for slides 25, 26, and 27 represent the intensities after no-target DNA dummy hybridization and washing. The filled triangles for slides 30–39 represent the intensities after a pre-hybridization bath (30–34 without bovine serum albumin (BSA) blocker; 35–39 with 0.2 mg/ml BSA) and washing.

In order to show more detail at the lower intensity scales, three exceptional data points were omitted: an unstirred positive control probe spot from slide 40 at 8.8%, an unstirred positive control probe spot from slide 48 at 14.8%, and an unstirred negative control probe spot from slide 62 at 9.6%. Also, two dummy-hybridized positive control probe spots from slide 25 and four dummy-hybridized negative control probe spots from slide 26 do not appear because their median intensities were below the surrounding background level, giving a negative background-subtracted intensity value.

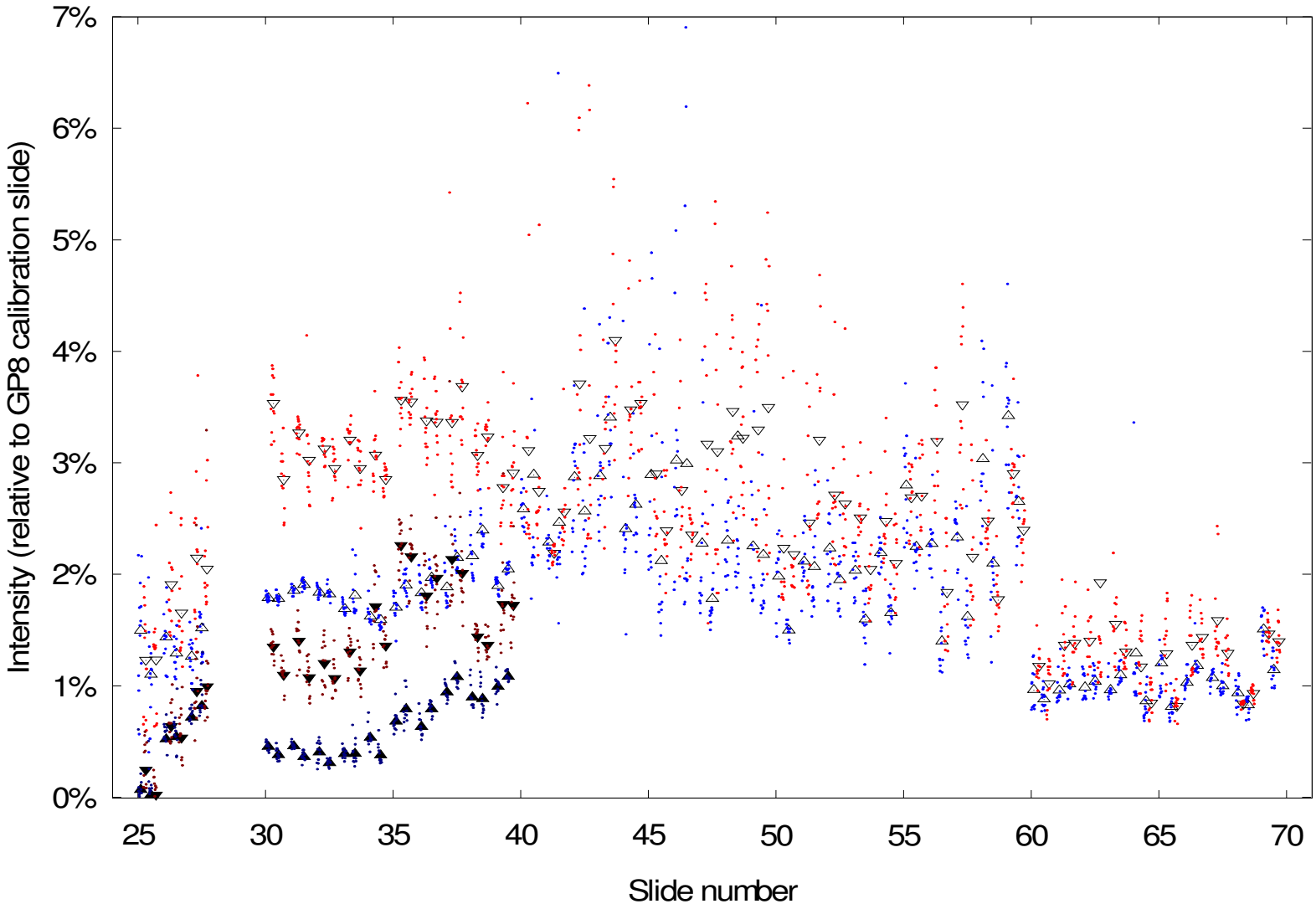
7%
6%
5%
4%
3%
2%
1%
0%
Intensity (relative to GP8 calibration slide)
25
30
35
40
45
50
55
60
65
70
Slide number

4.2.5 Target DNA production and fluorescent labeling

I selected the forward sequence of gene b1771 to be the positive control single-stranded DNA target species. Shannon Guiles amplified and labeled this sequence by PCR with fluorescent Cy3-conjugated dUTP in the nucleotide mix and only the forward primer, according to the recipe in the Appendix starting on page 120, and purified it as before. This standard "stock" concentration of labeled target DNA to which all dilution ratios in the rest of the experiment refer is approximately 0.1 µg/µl, or 300 nM. The stock labeled target DNA was stored at –20°C in the dark.

4.2.6 Hybridization

Array hybridization was performed either with conventional "coverslip" method or the liquid-on-liquid mixing method. The hybridization buffer was 3x standard saline citrate (SSC): 0.45 *M* sodium chloride and 0.05 *M* sodium citrate in water. The target DNA was diluted in hybridization buffer and prepared as per the Corning protocol (Hybridization without Formamide: section 9.2.2.4.3): I boiled the microfuge tube holding the diluted target at 95°C for one minute and then centrifuged it for one minute to collect all drops of condensed vaporized target solution. The only differences from the Corning protocol were (1) I did not employ a pre-hybridization protein-blocker wash (except for slides 35-39) and (2) the target solution did not contain a nucleic acid blocker.

4.2.6.1 Coverslip method

Coverslip-method hybridizations were performed by placing an unhybridized microarray into an Array-It hybridization chamber, pipetting 10 µl of boiled diluted target solution directly onto both the stirred and unstirred areas of the microarray, and placing a cover glass on the drop, spreading the target volume under the area of the cover glass. A 5-µl drop of hybridization buffer was placed in a well at the end of the

microarray away from the unstirred side, and the Array-It hybridization chamber lid was attached. The entire hybridization chamber was immersed in a 50±2°C water bath for the duration of the hybridization process.

4.2.6.2 Liquid-on-liquid mixing

Liquid-on-liquid mixing hybridizations were performed by assembling the LOLM slide holder and dual-reaction chamber with an unhybridized microarray and clean O-ring seals. 200 µl of boiled diluted target solution was pipetted into the center of each reaction chamber, and the slide holder was rocked briefly by hand until the target solution wetted the entire microarray area enclosed by the reaction chamber. (Note that this volume of aqueous solution is ten times greater than that used in the immunofluorescence staining and flow visualization experiments. This was because the Corning GAPS II microarray slides were more hydrophobic than the standard glass slides used in the earlier experiments, and the larger volume was needed to wet the same slide surface area.) 2 ml of mineral oil was pipetted down the side of each reaction chamber, covering the aqueous target solution. The pre-assembled stirring motor and motor mount was then attached to the reaction chamber, and the combined apparatus was placed in a 50°C air thermostat for the duration of the hybridization process. In practice, the temperature varied in the range 40–55°C. The stirring was performed by the same stepper motor used in the previous chapters. The stirring with pauses was accomplished by having the software controller step the motor through two full turns in one second, followed by 20 seconds of inaction.

Figure 4-6: Experiment map showing hybridization conditions, target concentrations, and hybridization durations. Each row represents a particular hybridization geometry and target concentration, written as a dilution from the stock solution. The abbreviations are: (U) LOLM hybridization without agitation; (6) LOLM hybridization with stirring at 6 rpm; (145) LOLM hybridization with stirring at 145 rpm; (145-P) LOLM hybridization with stirring at 145 rpm for 1 second followed by no agitation for 20 seconds; (C) coverslip hybridization in the Array-It hybridization chamber. The horizontal position of each bar represents the hybridization duration of the experiment labeled by the number to the right of each bar. For example, experiment #23 hybridized a 1:400,000 dilution of stock target in the LOLM reaction chamber with stirring at 145 rpm for 5 hours. Each LOLM hybridization used a target volume of 200 µl, while each coverslip hybridization used 10 µl of target. Samples hybridized with the five blue-shaded conditions (rows labeled C 1:2,000 through 145-P 1:40,000) were each exposed to 1.5 fmol of labeled target molecules.

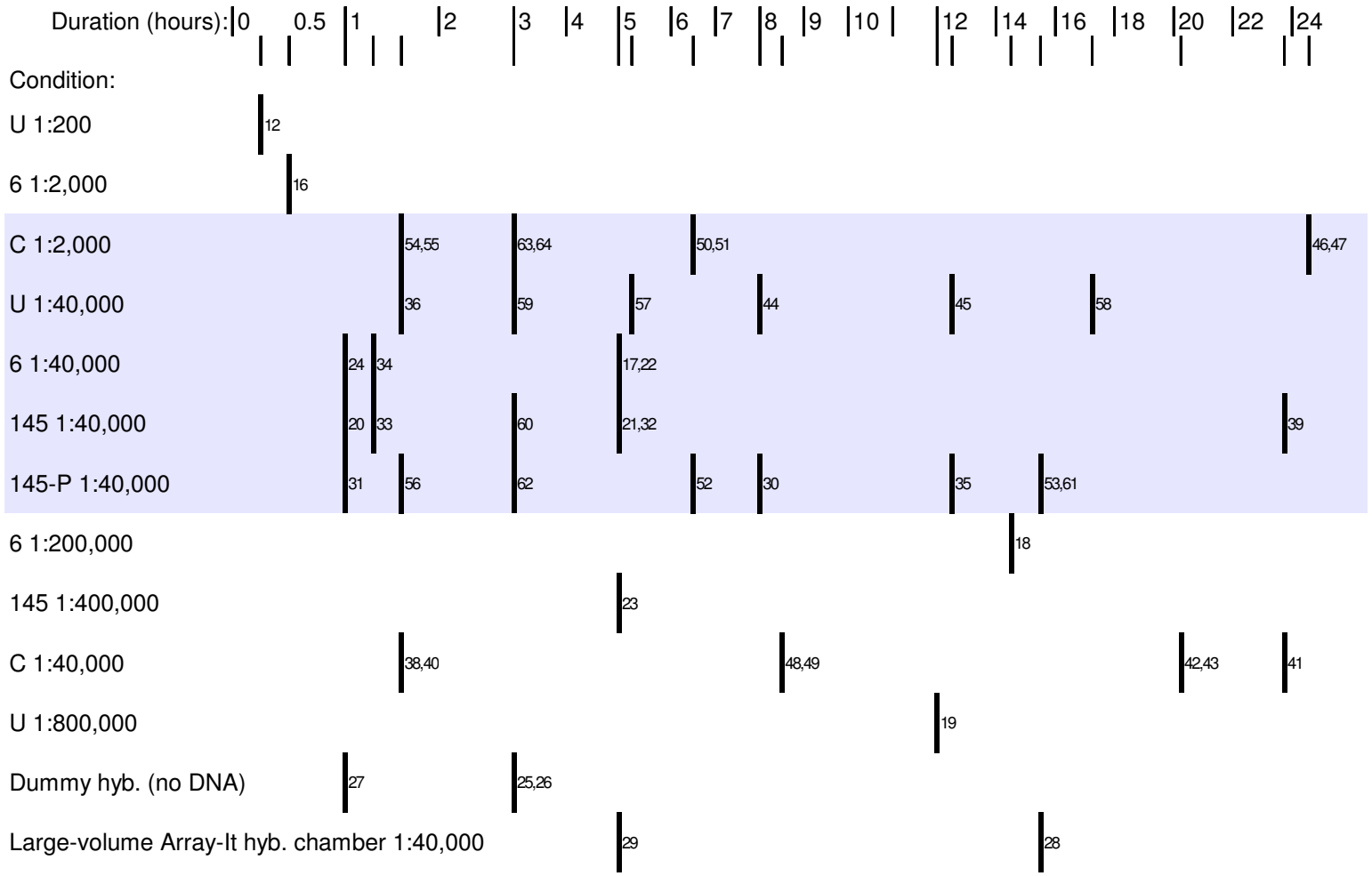
Duration (hours):
0
0.5
1
2
3
4
5
6
7
8
9
10
12
14
16
18
20
22
24
Condition:
U 1:200
12
6 1:2,000
16
C 1:2,000
54,55
63,64
50,51
46,47
U 1:40,000
36
59
57
44
45
58
6 1:40,000
24
34
17,22
145 1:40,000
20
33
60
21,32
39
145-P 1:40,000
31
56
62
52
30
35
53,61
6 1:200,000
18
145 1:400,000
23
C 1:40,000
38,40
48,49
42,43
41
U 1:800,000
19
Dummy hyb. (no DNA)
27
25,26
Large-volume Array-It hyb. chamber 1:40,000
29
28

4.2.6.3 Experiment map

The concentration of the target DNA, duration of the hybridization, and stirring rate and pattern (if any) were varied. Figure 4-6 shows a catalog of all the hybridization experiments that were done. In every case except the two high-concentration short-time experiments numbered 12 and 16 (data points shaded blue in Figure 4-8 and onward), the total amount of complementary DNA in the probes exceeded the amount in the target by a factor of 20 (conditions shaded blue in Figure 4-6 and data points colored black in Figure 4-8 and onward) or more (data points shaded red in Figure 4-8 and onward).

4.2.6.4 Post-hybridization

The post-hybridization washing was performed as described in the Corning protocol (section 9.2.2.5).

4.2.7 Scanning

After the post-hybridization wash and air-dry steps, the slides were again scanned with an Axon GenePix 4000B scanner. The scanned images were segmented into fluorescent spots and background areas and descriptive statistics of the pixel intensities of each fluorescent spot were reported with the GenePix Pro 4.0.1.23 software.

The fluorescence signal in the fluorescent spot and background regions is expected to be the sum of the fluorescence from all sources that could possibly be excited by the laser and detected by the photomultiplier tube. A complete list of these sources is shown for each category in Table 4.

Table 4: Sources of fluorescence expected in various areas of scanned microarray images.

Source	Positive control fluorescent spots	Negative control fluorescent spots	Background regions
Dark current of scanner's photomultiplier tube, and power fluctuations in excitation laser	Present	Present	Present
Glass substrate and surface coating	Present	Present	Present
DNA probe and residual DMSO printing solution	Present	Present	
Hybridization buffer	Present	Present	Present
DNA target (with fluorescent Cy3 labels)	Specifically-hybridized	Non-specifically adsorbed	Non-specifically adsorbed

Figure 4-7: Microarray hybridization intensity data compared with pre-hybridization fluorescence. These data have been normalized and corrected for power differences as described in section 8.3.4. The up- and down-pointing triangles show the arithmetic means of each set of 12 positive and negative control fluorescent spots' median intensities, respectively. The single-sided error bars denote the standard deviation of each group of 12 spots' median intensities. Each slide has a total of four groups of 12 spots, and they are given in the order: stirred-side positive control, stirred-side negative control, unstirred-side positive control, unstirred-side negative control. For comparison, the small triangles are imported from Figure 4-5, showing the mean median intensities after printing (open triangles) and pre-hybridization (filled triangles). The large filled triangles show the intensities for the same groups after hybridization. In order to show more detail, data points less than 0.1% of the intensity of the GP8 calibration slide are shown at the 0.001 level.

The mean median intensity of each group of hybridized negative control fluorescent spots (dark red filled big down-pointing triangles) in slides 30–39 is even lower than its corresponding pre-hybridized intensity (light red filled small down-pointing triangles), which in turn is lower than the post-printing fluorescence signal (light red open small down-pointing triangles). This suggests that it will not be necessary to subtract the pre-hybridization fluorescence signal from the post-hybridization signal. Still, the negative controls show a slight correlation between the mean post-printing and mean post-hybridization intensities.

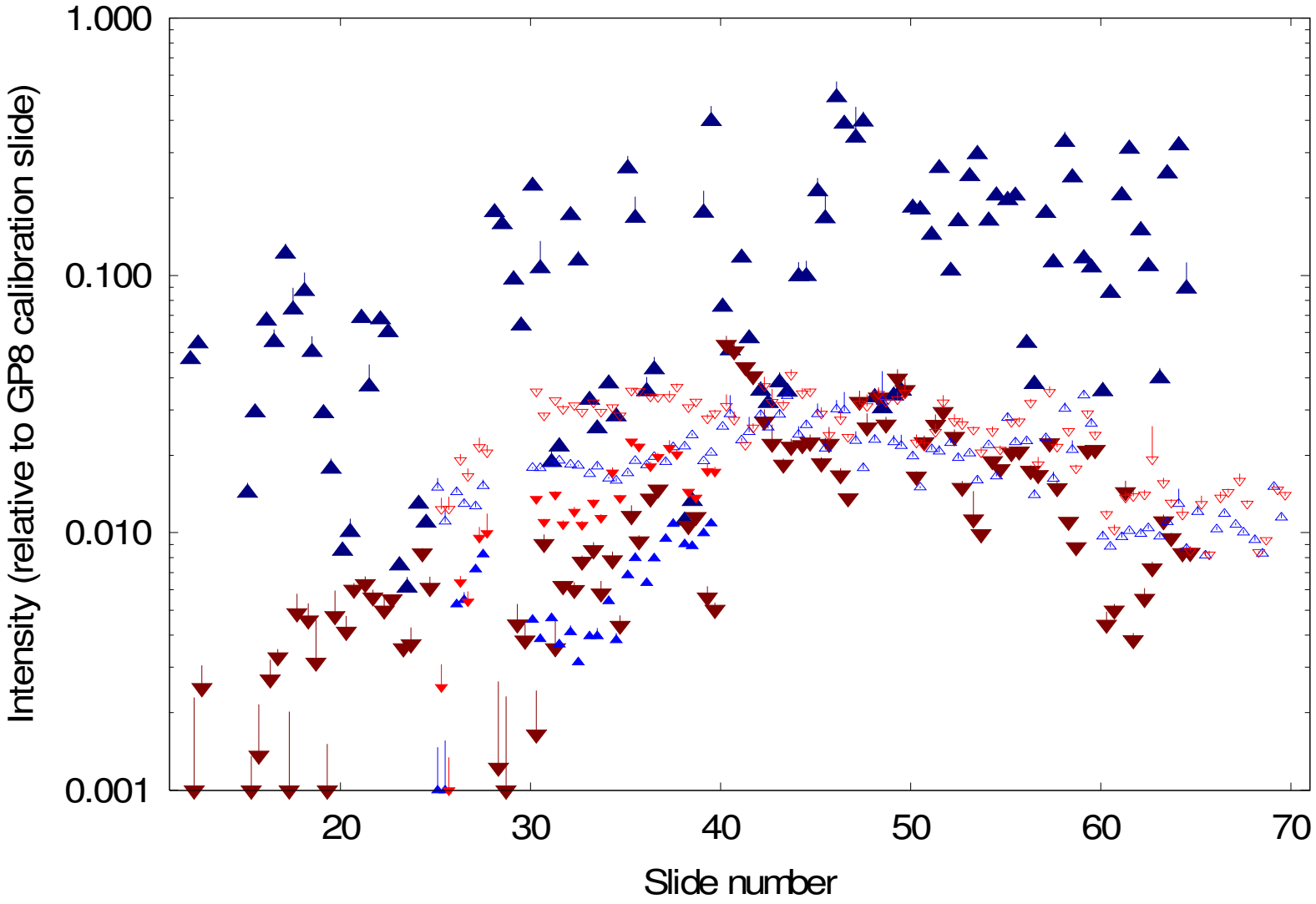
1.000
0.100
0.010
0.001
Intensity (relative to GP8 calibration slide)
20
30
40
50
60
70
Slide number

Local-background-subtracted median pixel intensities were calculated for all fluorescent spots and, if necessary, converted to an effective 800 V PMT Gain setting. Finally, these intensities were normalized by the model calibration slide intensity, which accounts for scanner age and power variations. The scanner calibration, conversion factors, and rationale for the normalization process are described in more detail in section 8.3, starting on page 126. These normalized fluorescent spot intensity values are shown averaged in groups of 12 fluorescent spots (positive or negative control, stirred-side or unstirred-side) in Figure 4-7.

To obtain the integrated intensity for each probe spot, these normalized intensity values were multiplied by the area of the fluorescent spot in 10-µm × 10-µm pixels; the integrated intensity for a reaction was the arithmetic sum of the integrated intensities of the 12 positive control probe spots. This integrated intensity was compared with the total integrated intensity expected from the amount of stock target DNA present in the target solution to obtain the efficiency with which the labeled target DNA adsorbed to the microarray probe spots.

4.3 Results

I will evaluate the effect of the liquid-on-liquid mixing (LOLM) technique on the efficiency of microarray hybridization — the efficiency of the adsorption of labeled target DNA to the microarray fluorescent probe spots. I will also attempt to assess the effect of LOLM on the sensitivity and specificity of microarray hybridization. By sensitivity, I mean how small of a signal the technique can help to measure; by specificity, I mean how well the technique can distinguish correct and incorrect hybridization. In all cases, I will compare the results with LOLM stirring to those achieved with unstirred LOLM and conventional coverslip hybridizations.

4.3.1 Efficiency

The efficiency of the microarray hybridization is the fraction of the total DNA in the applied target solution that bound to the positive-control probe spots. To calculate this, I assume that the integrated fluorescence intensity (median background-subtracted median fluorescent spot intensity times the area of the fluorescent spot, summed over all 12 positive-control fluorescent spots in one reaction chamber) is directly proportional to the amount of DNA that bound to the positive-control probe spots. (The proportionality constant is calculated in section 8.5 (see p. 138).) Then, I divide this integrated intensity by the integrated intensity expected from the DNA present in the applied target solution. More succinctly:

$$\text{Efficiency} = \frac{\text{Total measured fluorescence}}{\text{Total expected fluorescence}}$$

where both fluorescence signals are expressed in model calibration slide units; the total expected fluorescence is computed from the amount of diluted target solution placed in the reaction chamber and the calibrated fluorescence signal (see section 8.5); and the total measured fluorescence is the sum of the integrated intensities of the twelve positive-control fluorescent spots:

$$\begin{pmatrix}\text{Total measured}\\ \text{fluorescence}\end{pmatrix} = \sum_{\text{All 12 spots}} \left[\begin{array}{l}(\text{number of pixels})\times\\ (\text{median local background subtracted pixel intensity})\end{array}\right]$$

To calculate the uncertainty in the efficiency, I must add in quadrature the uncertainty in the total expected fluorescence and the uncertainty in the total measured fluorescence.

The uncertainty in the total expected fluorescence arises from two sources: pipetting or liquid-handling errors and the error in the calibrated fluorescence signal. To reduce pipetting and liquid-handling errors, I made intermediate dilutions of the

target solution. For example, to produce two 200-µl volumes of target solution at the 1:40,000 dilution from stock, I first made and mixed a 1:200 dilution of stock by pipetting 1 µl of stock target into a microfuge tube followed by 199 µl of hybridization buffer. I then took 2 µl of this 1:200 dilution and added 398 µl of hybridization buffer. Overall, there are five uptake-dispense operations with two pipettors, each calibrated (April 2004, just before the bulk of the data were taken) to less than 1% error, so the worst-case overall uncertainty in the amount of target DNA present in any hybridization reaction could be as large as ±5%. The treatment of the calibrated fluorescence signal relies on the uncertainties computed for the fit parameters: 0.3% in the slope and 59% in the intercept. We will ignore the fractional error in the intercept because the amounts of stock DNA target solution used in each experiment was in the region of Figure 8-7 where the non-zero intercept and zero intercept calibration curves have are very close. The overall uncertainty in the total expected fluorescence is close to 5%.

The uncertainty in the total measured fluorescence can be estimated in two ways: the standard deviation of the positive-control pixel intensity over the 12 spots on each side of the slide, multiplied by the square root of the equivalent number of 10-µm×10-µm pixels, plus an additional term to account for uncertainty in the number of pixels; or, the standard deviation of the integrated median local-background subtracted intensities of the 12 spots, times the square root of 12. The latter method does require the assumption that the pixel intensities within every individual fluorescent spot is drawn from the same distribution as for other probe spots in the same 12-spot group. We will use the latter method for two reasons: convenience, because the GenePix Pro software reports descriptive statistics on the pixel intensities in each spot; and accuracy, because it is difficult to explain an estimate of the uncertainty in the number of pixels. One way would be to note that in most of the scan

data, each 600-µm (diameter) circular fluorescent probe spot contains about 1,000 20-µm×20-µm pixels, which means that about 10% of the pixels are on the circumference, which could then be assumed to approximate the correct boundary position. Using the easier method, I estimate the fractional uncertainty in the total measured fluorescence to be in the range 1.4% to 27.5%, with average at 8%.

In calculating the data for the plots, I used the slide-specific values for the uncertainties, without dropping any quantities. The efficiency results appear in Figure 4-8.

However, before discussing the results shown in Figure 4-8, I will describe modifications to the naïve diffusion-only model from section 2.3.1 that apply to the microarrays treated with the LOLM conditions. These experiments differ from earlier ones in that the volume of the reaction solution was much larger for the microarray hybridizations than the immunofluorescence stainings — so large, in fact, that the one-dimensional diffusion of reactants from the bulk of the solution to the reactive surface was likely a significant limitation on the rate of reaction, as highlighted by Gadgil et al. (2004). Further, the extended hybridization times allowed the circular diffusion-radius depletion regions centered on each probe spot to intersect. After the depletion regions begin to overlap, the expected total efficiency for the 12 replicate positive control probe spots increases slower than when each probe spot draws reactants in isolation. A simplified estimate of the model efficiency (solid curve in Figure 4-8) shows cusps at 1,200, 9,000, and 23,000 seconds as each successive model regime becomes appropriate; in reality, the transitions should not be so pronounced. (This simplified model overestimates the expected diffusion-only hybridization efficiency in the neighborhood of the cusps.)

Figure 4-8: Absolute efficiency of DNA hybridization versus hybridization duration, on a log-log scale. The efficiency is the sum of the integrated intensity of all positive-control fluorescent spots, divided by the expected fluorescence yield for the amount of labeled target solution present in the hybridization reaction. The integrated intensity of a fluorescent spot is calculated by multiplying the local-background-subtracted median intensity of the fluorescent spot by the number of 10-µm × 10-µm pixels in the fluorescent spot.

An efficiency of 1.0, denoted by the dashed line, implies that all the target bound to the positive probes. The solid curve is the approximate expected efficiency given a diffusion-only model and rapid binding. Filled symbols denote the stirred-side positive controls; unfilled symbols denote the unstirred-side positive controls. Blue-colored symbols denote hybridizations where total target exceeded 1.5 fmol (200 µl of 1:40,000 dilution of stock); black symbols denote hybridizations where total target equaled 1.5 fmol; red symbols denote hybridizations where total target was less than 1.5 fmol. Hybridization conditions were: square (■,□) coverslip; diamond (♦,◊) unstirred LOLM; down triangle (▼,▽) 6-rpm LOLM; up triangle (▲,Δ) 145-rpm LOLM; circle (●,○) paused 145-rpm LOLM.

For clarity, pairs of points corresponding to different samples have been displaced slightly in the x-axis; for the true hybridization times, please refer to Figure 4-6. Also, the absolute efficiencies of the blue symbols were so low that they are shown on the floor of the plot. The true values are: blue diamond 0.0006 (filled), 0.00053 (open); blue triangle 0.00022 (filled), 0.00166 (open); blue triangle 0.00342 (filled), 0.00337 (open).

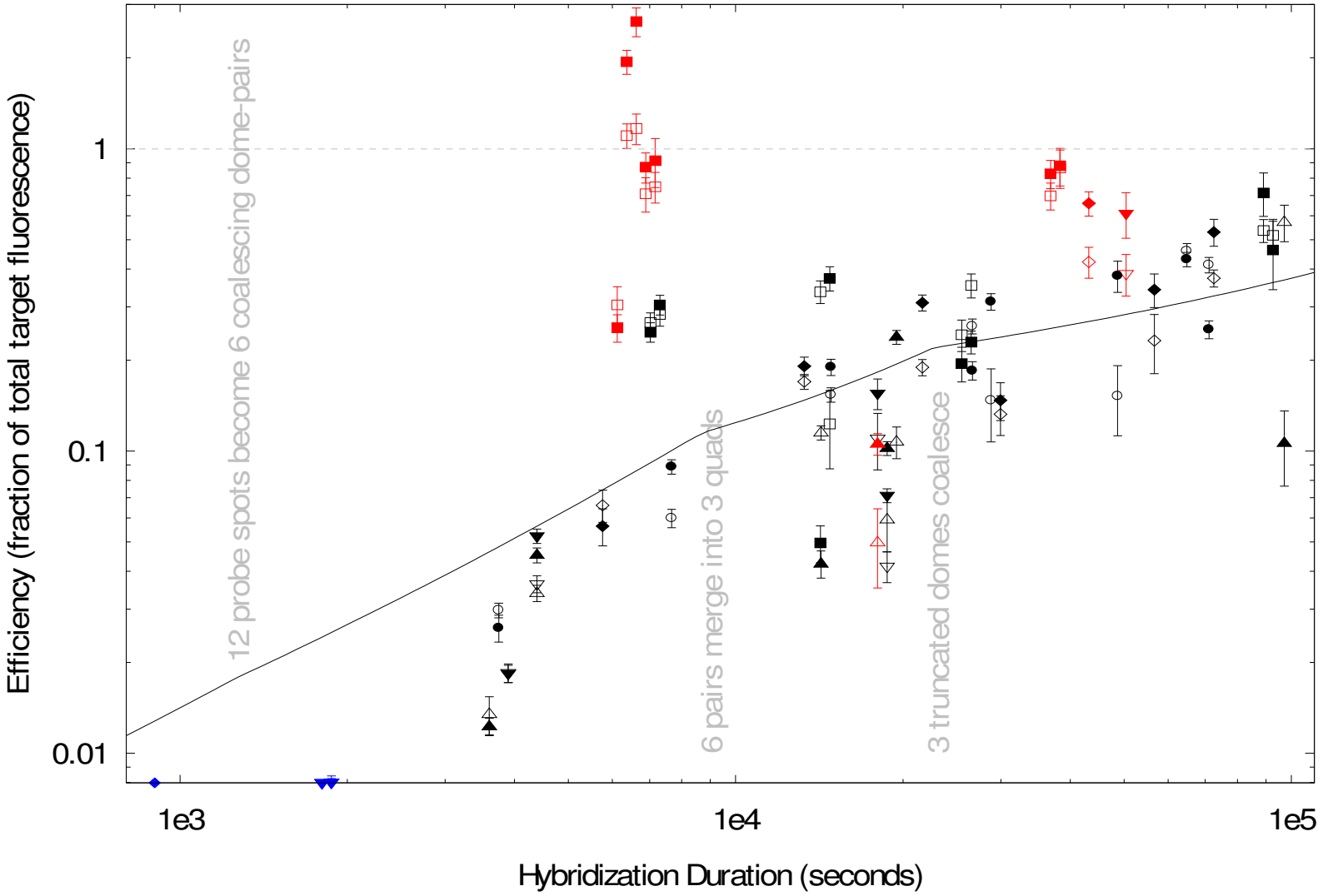
Efficiency (fraction of total target fluorescence)
1
0.1
0.01
1e3
1e4
1e5
Hybridization Duration (seconds)
12 probe spots become 6 coalescing dome-pairs
6 pairs merge into 3 quads
3 truncated domes coalesce

The diffusion-only model predicts complete binding in a week (much less than 100 days) because the reaction chamber is smaller than the whole slide and there are twelve replicated positive control probe spots over the surface of the microarray. I expect that all the coverslip experiments (square-shaped symbols) would fall on the diffusion model curve. If the unstirred LOLM configuration were a diffusion-only system, then I would similarly expect all unstirred LOLM experiments (diamond-shaped symbols) and unstirred-side data (open symbols, any shape) to fall on or near the curve. If stirring were to produce any increased hybridization, then I would expect to see the stirred-side data (filled circles and triangles) have initially higher efficiencies than their unstirred-side (open circles and triangles) counterparts and that eventually the unstirred-side data would "catch up" to the stirred-side adsorption. The data frustrate all of these expectations. There is an overall trend toward higher hybridization efficiencies with longer hybridization duration. However, the stirred-side fluorescence signal was not always stronger than the unstirred-side integrated fluorescence intensity. Further, except for the anomalously high low-concentration coverslip experiments, there is no method among those tested that is clearly superior to the others.

The efficiencies from the slides where the labeled target exceeded the binding capacity of the probes (high-concentration, blue symbols) are all low, probably because the efficiency is calculated as a fraction of the applied target, not an equivalent mass of probes. If we assume that any single-stranded probe can bind an equal mass of single-stranded target, then the maximum possible efficiency of the blue diamonds — representing the unstirred 1:200 experiment with 300 fmol of labeled target — is (28 fmol probe over all 12 probe spots) / (300 fmol) = 9%, which is still some 100 times the amount that bound. The blue triangles, representing the 6-rpm LOLM 1:2,000 samples with 30 fmol of labeled target, should not move much.

A more direct comparison — the ratio of the efficiency of the stirred to the unstirred positive controls — appears in Figure 4-9. Here and in Figure 4-10, the error bars for the efficiency ratio are computed as for any quotient.

If in Figure 4-8 the stirred side of a microarray had a higher efficiency than its corresponding unstirred side, then that pair would be assigned a value greater than 1.0 in Figure 4-9; if the stirred side were less efficient, that that microarray would have a ratio less than 1.0.

I expect the coverslip and unstirred LOLM hybridizations to have stirred-side-to-unstirred-side ratios of 1.0, since both halves of the microarray were exposed to the same conditions. In fact, most samples hybridized with those conditions show stirred-side-to-unstirred-side efficiency ratios above 1.0, which suggests a systematic bias. Printed samples were assigned randomly to hybridization conditions, so there is no reason this systematic bias would be absent from the stirred LOLM experiments. Assuming the same level of systematic bias, any improved efficiency due to stirring should appear as an even larger efficiency ratio. However, none appears in Figure 4-9; indeed, without the titles, it would be difficult to say which plot contained stirred-LOLM data.

Within the stirred LOLM experiments, we expect the 6-rpm LOLM stirring (down triangle symbols) to spread the reactants less than the 145-rpm LOLM stirring, but the mean efficiency ratio with the 6-rpm continuous LOLM stirring is higher than the mean efficiency ratio with the 145-rpm paused LOLM stirring (circle symbols), which itself exceeds the mean efficiency ratio with 145-rpm continuous LOLM stirring (up triangle symbols). This suggests that slower stirring may be important.

Figure 4-9: Efficiency ratio of stirred to unstirred positive controls versus hybridization duration, on a log-log scale. A ratio of 1 indicates that the stirred and unstirred positive controls on a sample had the same efficiency, and a dashed line is drawn at this level as a guide to the eye. Ratios larger than 1 indicate that the stirred side positive controls collected more fluorescent target than the unstirred side positive controls.

Symbol shapes and colors are the same as in Figure 4-8: square (■) for coverslip hybridizations; diamond (♦) unstirred LOLM; down triangle (▼) 6-rpm LOLM; up triangle (▲) 145-rpm LOLM; circle (●) paused 145-rpm LOLM; red for hybridizations with less than 1.5 fmol of labeled target; black, 1.5 fmol of labeled target; blue, greater than 1.5 fmol of labeled target. For clarity, points have been displaced slightly in the horizontal axis.

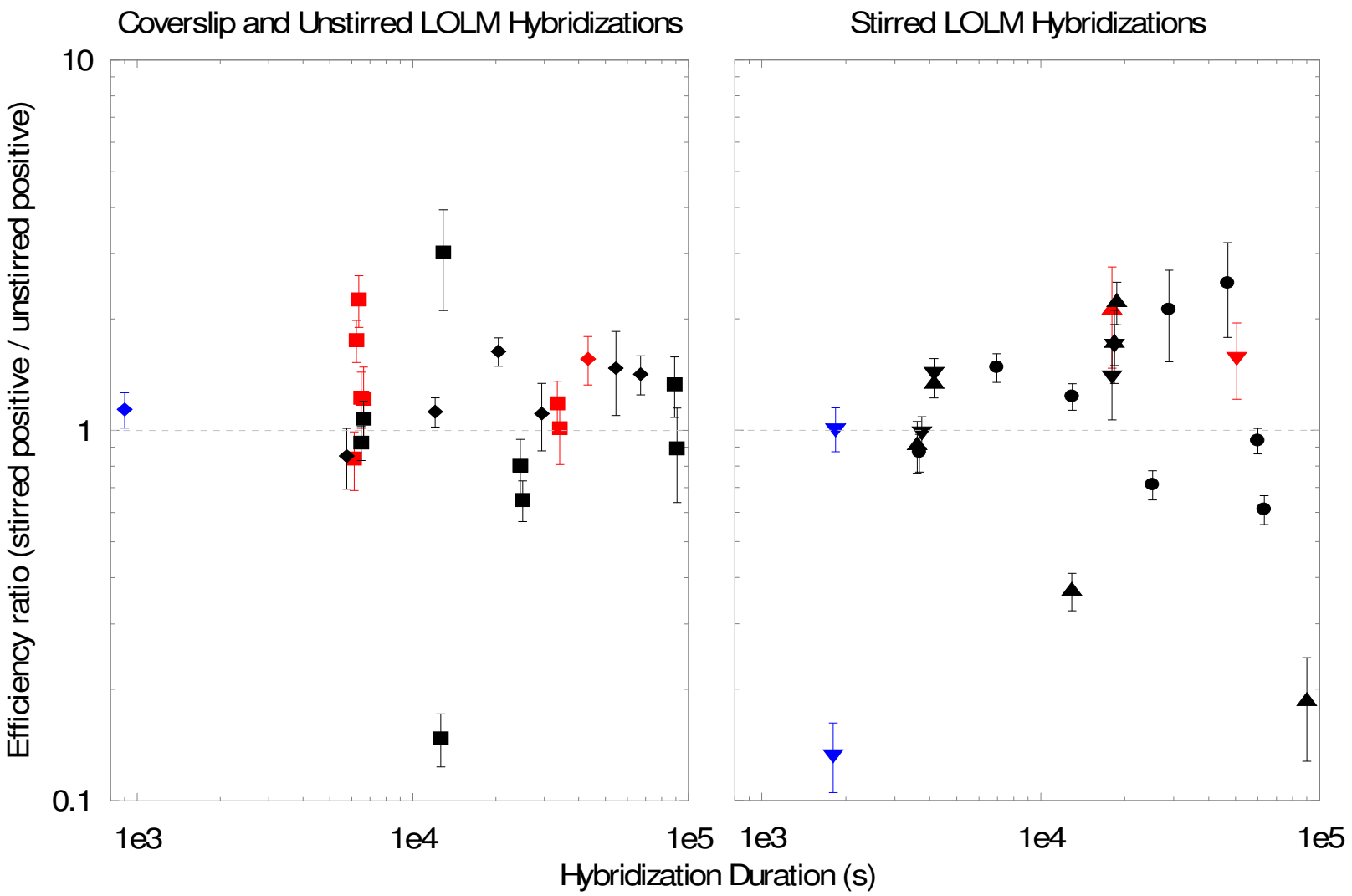
Coverslip and Unstirred LOLM Hybridizations
Stirred LOLM Hybridizations
Efficiency ratio (stirred positive / unstirred positive)
10
1
0.1
1e3
1e4
1e5
1e3
1e4
1e5
Hybridization Duration (s)

Using results from the flow visualization experiment (see the end of Chapter 3, on page 46), I combine the hybridization duration and LOLM stir-rate parameters to calculate the number of blend time-periods used to incubate each microarray. Here, the practical area ratio for the calculation of the blend time is that between the reaction chamber diameter and a probe spot diameter — returning to the baker's map analogy, when the stripe thickness approaches a probe spot diameter, then every probe spot will be accessible to the reactant solution. Figure 4-10 presents the same data as in Figure 4-9 but with blend time-periods instead of hybridization duration as the horizontal axis. If the ratio of the stirred-to-unstirred hybridization efficiencies were affected by the number of blend times elapsed during hybridization, then this figure should show a trend.

No clear trend in efficiency ratio as a function of blend times appears in Figure 4-10. The last several plots in this chapter show data in different hybridization condition categories, plotted against a hybridization duration horizontal axis, for ease of correlating data with Figure 4-6. Note, however, that within any single category of stirred experiments, the blend time is a constant numerical factor times the hybridization duration, so the horizontal axes may be imagined as such.

Figure 4-10: Efficiency ratio of stirred to unstirred positive controls versus blend times, on a log-log scale. The blend time was calculated in the previous chapter, and depends on the stir rate. To facilitate visual comparison, the plot from Figure 4-9 for the unstirred LOLM and coverslip-method hybridizations is shown with a compressed hybridization duration axis at the left, where zero blend times would belong. All other details are the same as in Figure 4-9: A ratio of 1 indicates that the stirred and unstirred positive controls on a sample had the same efficiency, and a dashed line is drawn at this level as a guide to the eye. Ratios larger than 1 indicate that the stirred side positive controls collected more fluorescent target than the unstirred side positive controls.

Symbol shapes and colors are the same as in Figure 4-8: square (■) for coverslip hybridizations; diamond (♦) unstirred LOLM; down triangle (▼) 6-rpm LOLM; up triangle (▲) 145-rpm LOLM; circle (●) paused 145-rpm LOLM; red for hybridizations with less than 1.5 fmol of labeled target; black, 1.5 fmol of labeled target; blue, greater than 1.5 fmol of labeled target. For clarity, points have been displaced slightly in the horizontal axis.

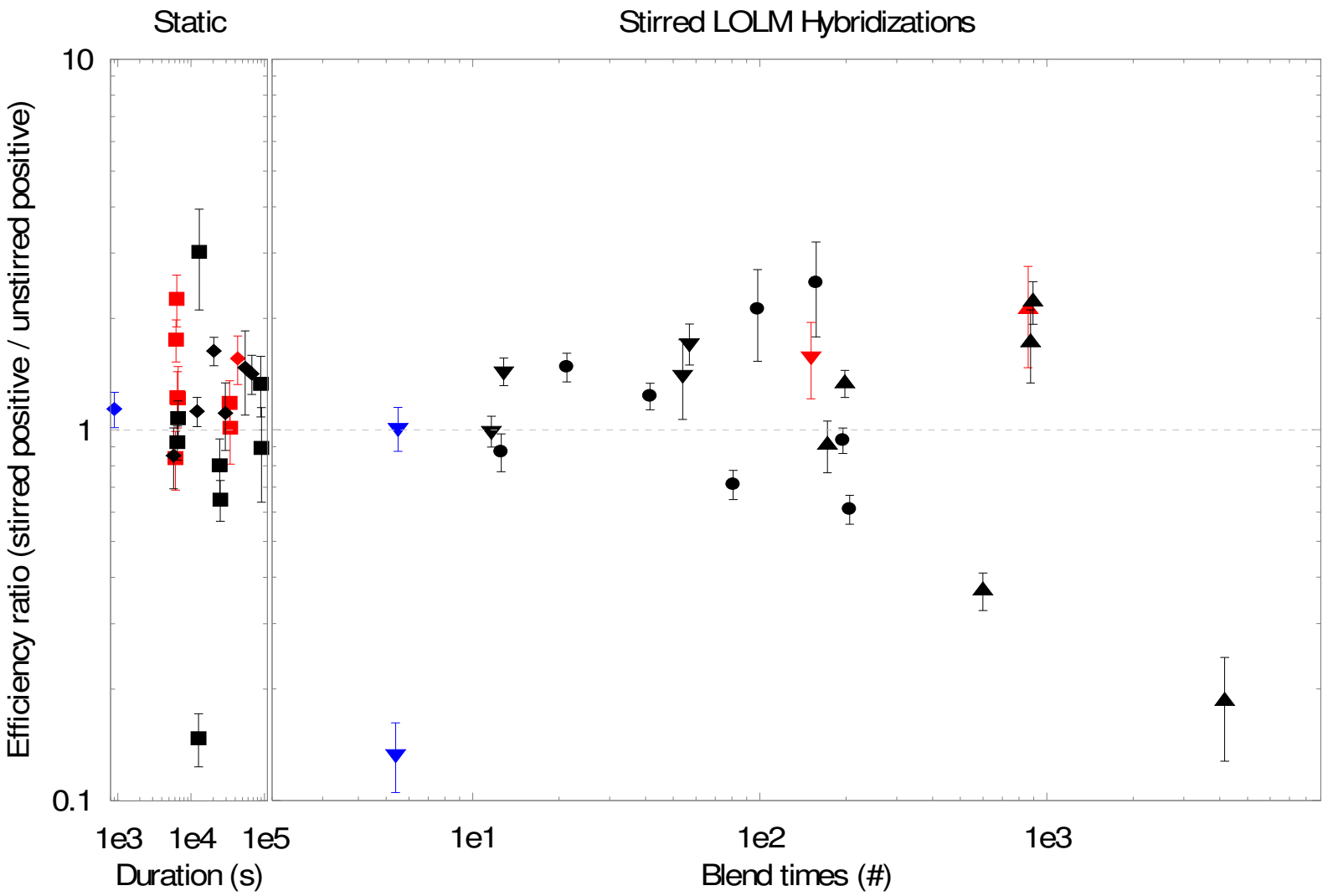
Static
Stirred LOLM Hybridizations
10
1
0.1
Efficiency ratio (stirred positive / unstirred positive)
1e3
1e4
1e5
Duration (s)
1e1
1e2
1e3
Blend times (#)

4.3.2 Uniformity (group of replicates)

I will use the coefficient of variation, defined as the ratio of the standard deviation of some data to their mean, to describe how the LOLM technique affects the uniformity, sensitivity, and specificity of microarray signals. (This coefficient of variation is often written CV%, but in this document I shall not express it as a percentage: here, 1.0 means 100%.) The coefficient of variation is a simplistic measure of relative variation, but more sophisticated analyses seem unwarranted.

If all areas on a given microarray were exposed to the same amount of labeled target during the hybridization process, then all probe spots would get an equal chance to hybridize with the target; if there were local depletions and varying concentrations of the target, then the resulting adsorption isotherm would likely not be uniform over the surface of the microarray. To check this, I will consider each 12-spot replicate group and calculate:

$$\text{spot CV\%} = \frac{\text{standard deviation of the 12 spots' integrated intensities}}{\text{mean spot integrated intensity}}$$

This describes the uniformity of the target adsorption: a smaller value means that any fluorescent spot's integrated intensity is a good estimator for any other in the replicate group, while a larger value means that the probe spots have large relative variations in integrated intensity. Unfortunately, this value has no proper distribution on which to define an uncertainty, and each data point reports data from a particular replicate group on a single slide.

- For the positive controls, if stirring increases intensity relative to the standard deviation, a lower CV% will result.
- Negative controls tend to have lower intensities than positive controls, and therefore higher CV%.

The spot-to-spot CV% data are shown in Figure 4-11. As before, all the unstirred experiments (coverslip method, unstirred LOLM, and open symbols in the 6-rpm, 145-rpm, and 145-rpm paused data) should be directly comparable to each other. For the positive controls, it appears that, in general, the stirred CV% and unstirred CV% have similar distributions, and are all below 1.0. The coverslip-method hybridizations seem to have slightly higher spot-to-spot CV% results than the others, but no technique among those surveyed seems to produce dramatically more-uniform microarray hybridizations than any other. For the negative controls, the 145-rpm continuous and paused LOLM stirred hybridizations seem to have slightly higher CV% than their unstirred controls, perhaps due to a reduction in non-specific hybridization.

Figure 4-12 shows the ratio of the stirred to unstirred spot integrated intensity CV%'s from Figure 4-11. If the ratio is less than 1.0, then the stirred side had a lower CV% than the unstirred side. If the ratio exceeds 1.0, then the stirred side had a greater CV% than the corresponding unstirred side. Overall, it appears that under the conditions tested, the LOLM stirring produces little or no improvement in uniformity among the positive controls compared to unstirred and coverslip-method hybridizations.

Figure 4-11: Spot integrated intensity CV%. This is the ratio of the standard deviation of each group of 12 fluorescent spots' integrated intensities to their weighted arithmetic mean (total integrated intensity (sum over fluorescent spots: pixel times local background-subtracted mean intensity) divided by number of fluorescent spots).

Top row: positive controls; bottom row: negative controls. Symbol shapes and colors are the same as in Figure 4-8: filled symbols denote stirred-side data and open symbols denote unstirred-side data; red for hybridizations with less than 1.5 fmol of labeled target; black, 1.5 fmol of labeled target; blue, greater than 1.5 fmol of labeled target. Data obtained under different hybridization conditions are shown in different panels, but all panels have the same axis ranges to facilitate visual comparisons. For clarity, data points in the coverslip, 6-rpm LOLM, and 145-rpm LOLM panels have been displaced slightly in the x-axis.

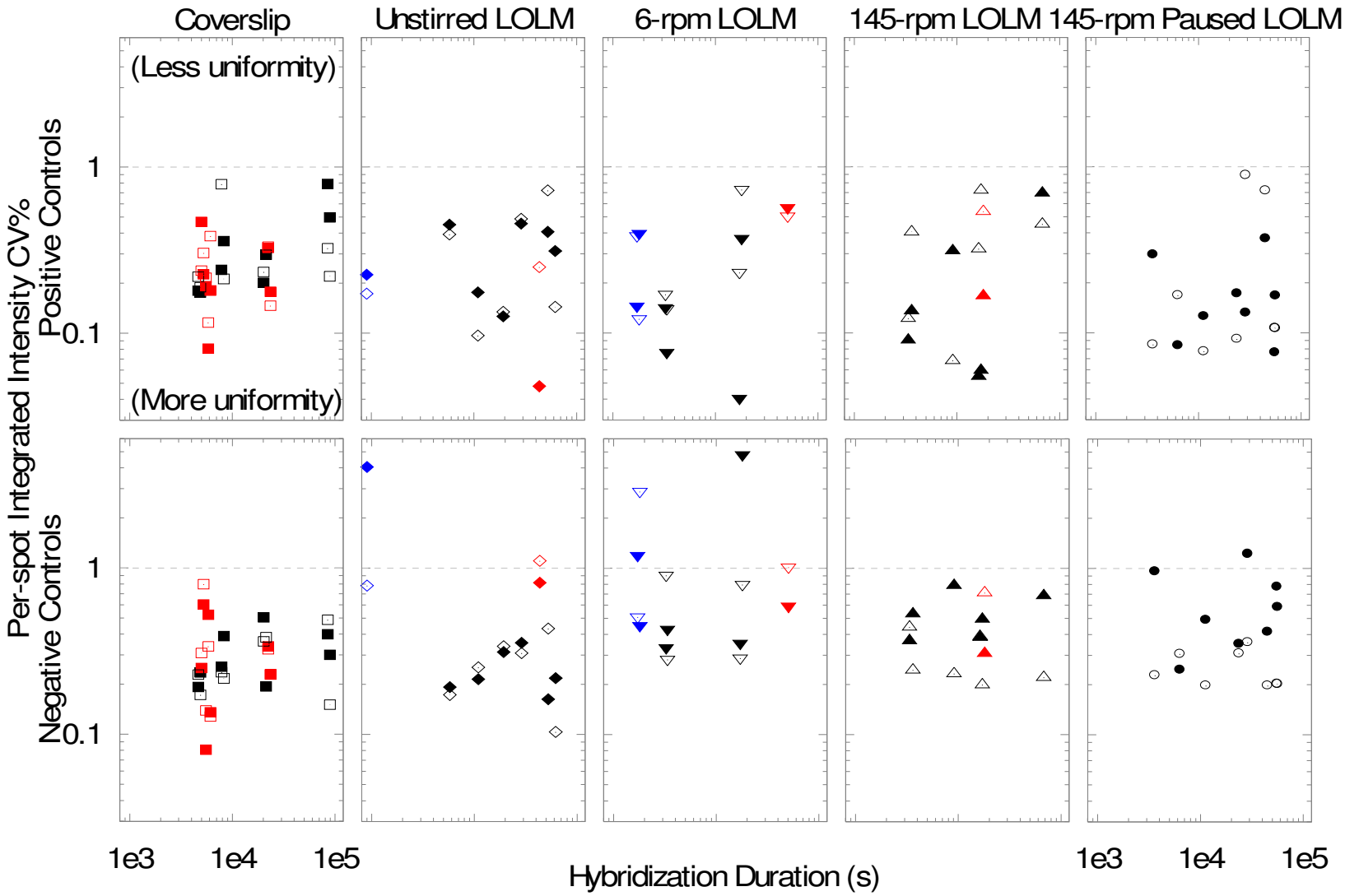
Coverslip
Unstirred LOLM
6-rpm LOLM
145-rpm LOLM
145-rpm Paused LOLM
(Less uniformity)
(More uniformity)
Per-spot Integrated Intensity CV%
Positive Controls
Negative Controls
1
0.1
1e3
1e4
1e5
Hybridization Duration (s)

Figure 4-12: Ratio of stirred to unstirred spot integrated intensity CV%. This is the ratio of the filled to open symbols shown in Figure 4-11. A level of 1 indicates that the CV% of the stirred and unstirred spot integrated intensities were the same, while a ratio less than 1 means that the stirred spot CV% was less than the corresponding unstirred control spot integrated intensity CV%.

Top row: positive controls; bottom row: negative controls. Filled symbols: stirred; open symbols: unstirred. Symbol shapes and colors are the same as in Figure 4-8: red for hybridizations with less than 1.5 fmol of labeled target; black, 1.5 fmol of labeled target; blue, greater than 1.5 fmol of labeled target. Data obtained under different hybridization conditions are shown in different panels, but all panels have the same axis ranges to facilitate visual comparisons. For clarity, data points in the coverslip, 6-rpm LOLM, and 145-rpm LOLM panels have been displaced slightly in the x-axis.

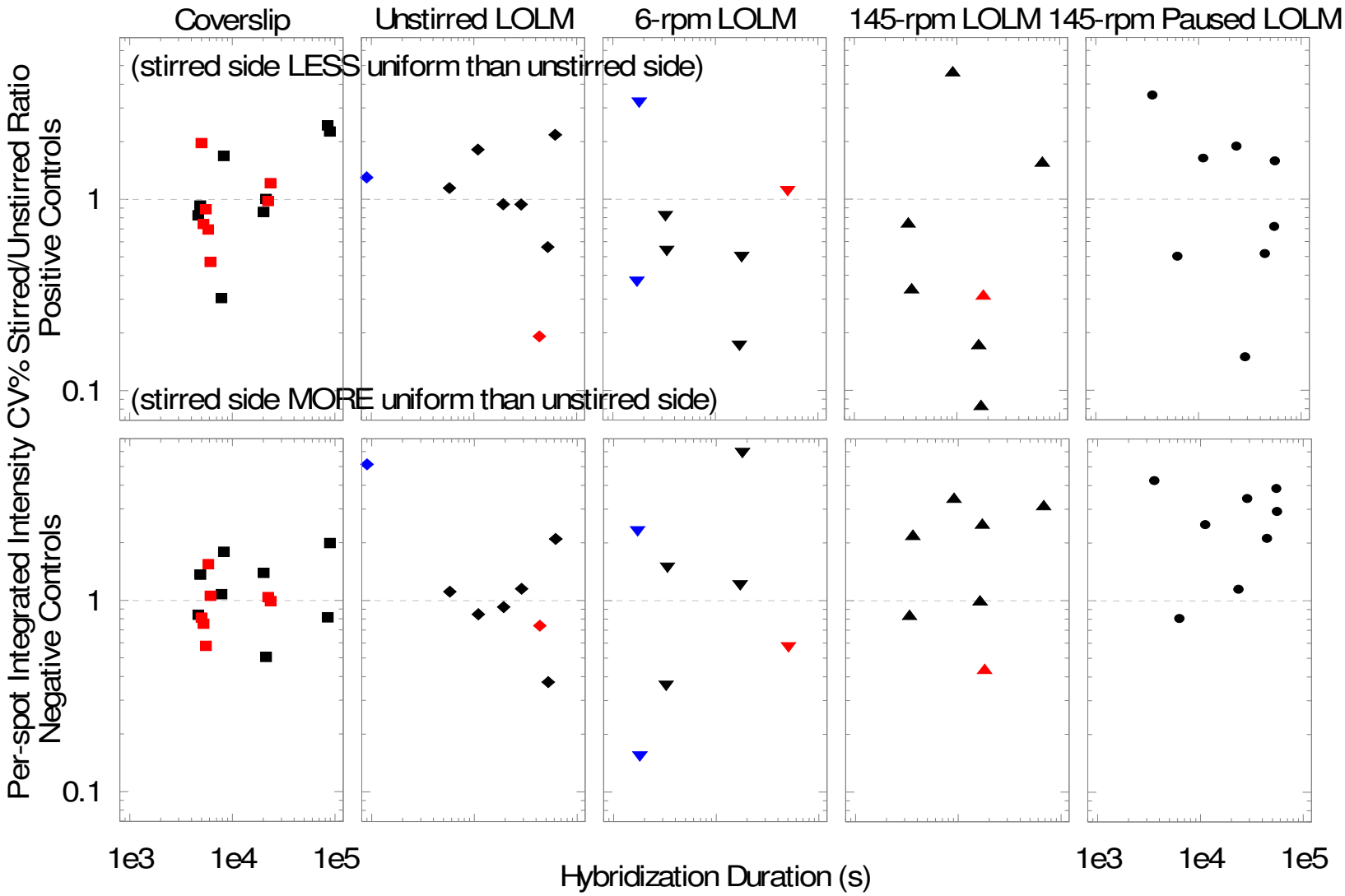
Coverslip
Unstirred LOLM
6-rpm LOLM
145-rpm LOLM
145-rpm Paused LOLM
(stirred side LESS uniform than unstirred side)
(stirred side MORE uniform than unstirred side)
Per-spot Integrated Intensity CV% Stirred/Unstirred Ratio
Positive Controls
Negative Controls
1
0.1
1e3
1e4
1e5
Hybridization Duration (s)

4.3.3 Sensitivity and Specificity (pixel)

In the previous section, I described how well any given fluorescent spot estimated the average of its group. We must also consider the information in that fluorescent spot. To evaluate the sensitivity and specificity of the microarray with and without the LOLM technique, I will consider the pixel CV%, that is:

$$\text{pixel CV\%} = \text{mean of features}'\left(\frac{\text{standard deviation of pixel intensities}}{\text{mean pixel intensity}}\right)$$

The ideal positive control foreground signal would have a high intensity above background, and little or no intensity variation within the area, producing a low CV%, which implies good sensitivity. The ideal negative control signal would have little or no fluorescence signal above background, producing a high CV%, which implies good specificity. If the CV% exceeds 1, then the local-background-subtracted intensity is within one standard deviation of zero, which is a common criterion for a negative result.

The pixel CV% data are shown in Figure 4-13. As before, all the unstirred experiments (coverslip method, unstirred LOLM, and open symbols in the 6-rpm, 145-rpm, and 145-rpm paused data) should be directly comparable to each other. However, for the positive controls, the pixel CV% obtained in the coverslip method is higher than those in the other methods, suggesting less sensitivity than obtained in any of the LOLM cases. The unstirred LOLM and the 145-rpm paused LOLM pixel CV% are mostly lower (suggesting higher sensitivity) than the continuously stirred LOLM cases. Since the pixel CV% is defined as an arithmetic mean, it makes sense to calculate a corresponding standard deviation of the mean (standard error), and these values are shown as one-sided error bar heights.

The negative controls in the 6-rpm, 145-rpm, and 145-rpm paused LOLM stirred samples show higher pixel CV% values — which I interpret as improvements in specificity — compared to their unstirred counterparts, which are on a par with the pixel CV% obtained from the coverslip and unstirred LOLM experiments.

The ratio of the stirred to unstirred pixel CV% appears in Figure 4-14. The error bars are calculated in the standard way for quotients, using the standard errors calculated above. For the positive controls, ratios less than 1.0 suggest improvements in sensitivity due to stirring. The LOLM experiments show a slight trend towards improved sensitivity in longer-duration hybridizations. For the negative controls, ratios greater than 1.0 suggest improvements in specificity due to stirring, which are in evidence in the paused 145-rpm LOLM experiments.

Overall, it appears that under the conditions tested, the LOLM technique may produce slight improvements in sensitivity and specificity compared to coverslip-method hybridizations.

Figure 4-13: Mean pixel CV%. This is the simple mean over all fluorescent spots within a certain group of each fluorescent spot's ratio of the standard deviation of the fluorescent spot's pixel intensities to its local background-subtracted median intensity. The simple standard error of each group of 12 fluorescent spots is shown as the height (not length) of the angled error bar extending up and to the right for stirred-side controls and up and to the left for unstirred-side controls.

The error bars are drawn only upwards for clarity, but it is important to keep in mind that they extend downwards, too. Since most of the error bars are so small, the logarithmic axis does not impose a large visual distortion.

Top row: positive controls; bottom row: negative controls. Filled symbols: stirred; open symbols: unstirred. For clarity, data points in the coverslip, 6-rpm LOLM, and 145-rpm LOLM panels have been displaced slightly in the x-axis.

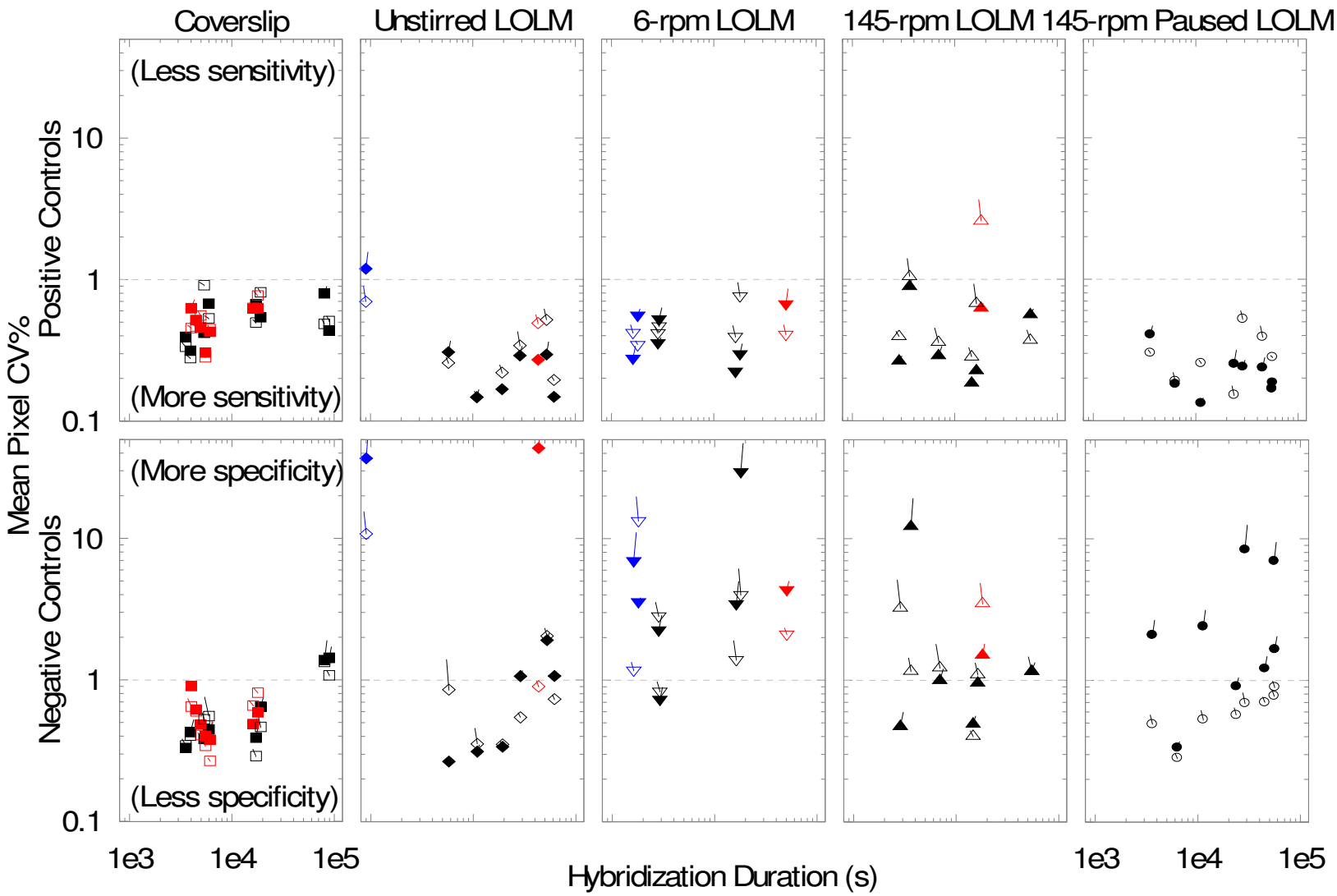
Coverslip
Unstirred LOLM
6-rpm LOLM
145-rpm LOLM
145-rpm Paused LOLM
(Less sensitivity)
(More sensitivity)
(More specificity)
(Less specificity)
Positive Controls
Negative Controls
Mean Pixel CV%
10
1
0.1
1e3
1e4
1e5
Hybridization Duration (s)

Figure 4-14: Ratio of stirred to unstirred pixel intensity CV%. This is the ratio of the values of the filled to open symbols shown in Figure 4-13. A level of 1 indicates that the CV% of the stirred and unstirred fluorescent spot pixel intensities were the same, while a ratio less than 1 means that the stirred pixel CV% was less than the corresponding unstirred control pixel intensity CV%.

Top row: positive controls; bottom row: negative controls. Filled symbols: stirred; open symbols: unstirred. Symbol shapes and colors are the same as in Figure 4-8: red for hybridizations with less than 1.5 fmol of labeled target; black, 1.5 fmol of labeled target; blue, greater than 1.5 fmol of labeled target. Data obtained under different hybridization conditions are shown in different panels, but all panels have the same axis ranges. For clarity, data points in the coverslip, 6-rpm LOLM, and 145-rpm LOLM panels have been displaced slightly in the x-axis.

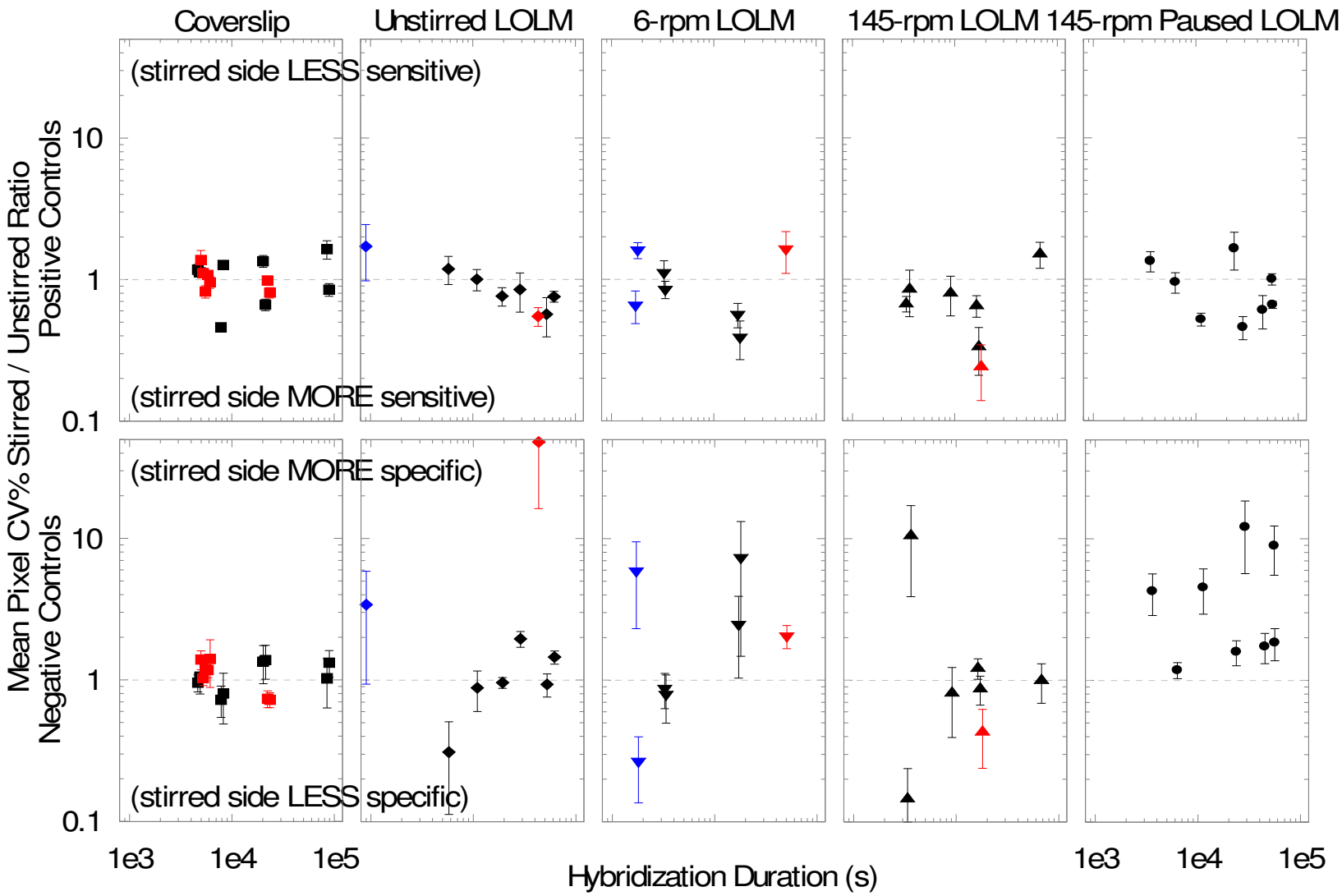
Coverslip
Unstirred LOLM
6-rpm LOLM
145-rpm LOLM
145-rpm Paused LOLM
(stirred side LESS sensitive)
(stirred side MORE sensitive)
(stirred side MORE specific)
(stirred side LESS specific)
Mean Pixel CV% Stirred / Unstirred Ratio
Positive Controls
Negative Controls
10
1
0.1
1e3
1e4
1e5
Hybridization Duration (s)

4.4 Conclusion

The lack of enhancement in hybridization efficiency is comparable to the data given for the Advalytix Arraybooster in Figure 4-1(a), samples 1–10 (PCR products) for the 8- and 20-hour incubations, which matches my experimental conditions. The LOLM stirring produces no improvement in microarray sensitivity (how well faint signals may be measured). Compared to coverslip-method hybridizations, the stirring may produce at most slight improvements in uniformity and specificity under particular circumstances.

Why was it that the stirred immunofluorescence staining experiments showed a much larger enhancement than the stirred microarray experiments? One possible explanation may be found by analyzing the differences between the two experiments: in the immunofluorescence staining experiments, the enhancement was found by selecting the best-quality stained chromosome on each slide, while in the microarray experiments, all the probe spots were measured together; in the immunofluorescence staining experiments, the stirrer was a rotating paddle, which the flow visualization experiments showed would concentrate tracer particles in the center of the reaction chamber, while the agitator used in the microarray experiments dispersed the tracer particles more uniformly. Then, if the antibodies in the immunofluorescence staining experiments behaved like the tracer particles, fly chromosomes in the center of the reaction chamber might have been exposed to an effectively higher concentration of the antibody stain.

There are a few problems with this explanation. One is that the diffusion constant of the antibodies in the immunofluorescence staining experiments was over ten times larger than that of the tracer particles in the flow visualization experiments, which would tend to smear the concentration effect. The other is that the concentration

effects observed in the flow visualization experiments developed over the course of hours of high-speed stirring, which was much longer than the 15-minute and 1-hour incubation times used in the immunofluorescence staining experiments. Each of these two facts suggest that the concentration effect proposed above would be unlikely to account for the factor-of-a-hundred enhancement in immunofluorescence staining efficiency found in stirring. Still, the data selection may have played a role that was made impossible in the microarray experiment by the improved stirrer and data averaging analysis.

Another possibility is that the liquid-on-liquid mixing affected the DNA hybridization reaction differently than the antibody-antigen binding reaction. Perhaps the greater shear applied in the microarray experiment inhibited the DNA hybridization nucleation or zippering processes, by separating weakly hybridized DNA strands. (compare Sato et al., 2004) (By comparison, the antibodies used in the immunofluorescence staining experiments have relatively small intrinsic viscosities (Cantor and Schimmel, 1980a, p. 651) and are unlikely to have their tertiary structure disrupted by the flow.) But then the 145-rpm paused stirring experiments should have allowed plenty of time for hybridization without shear; yet the 145-rpm paused experiments failed to show any hybridization enhancement above the 6-rpm continuously stirred cases.

5 PHYSICS OF MIXING FOR SLIDE-BASED BIOLOGICAL ASSAYS

In this chapter, I discuss the liquid-on-liquid mixing system from a physics perspective. There are four sections: geometry of the stirring system; considerations for an optimal liquid-on-liquid mixer; a dynamical systems view of the stirring process; future experiments to discover why stirring produced no hybridization enhancement in the microarray experiments.

5.1 Geometrical considerations of the liquid-on-liquid mixing system

5.1.1 Large aspect ratio

The liquid-on-liquid mixing system is intended to improve transport in slide-based assays, where the chemical reaction substrate is spread over a wide area compared to the depth of the aqueous reactant solution. The aspect ratio in these experiments is large: an antibody with diffusion constant $D = 2\times10^{-7}$ cm^2/s requires an expected 60 s to diffuse through the 50-µm depth of the immunofluorescence staining assays; a 1-kb ssDNA molecule with a similar constant requires an expected 6000 s to diffuse through the 500-µm depth of my microarray experiments. These times are to be contrasted with the week (10^6 s) that diffusion alone would require to bring these molecules from one side of the typical 1-cm radius of the microarray reaction surface to the other.

This large aspect ratio differs from the typical bulk chemical reactor where reactants are mixed in solution. In the latter case, stirring is needed to shrink the diffusion boundary layers between the reactants in three-dimensional space. It may be desirable to make the solution into a uniform mixture. In slide-based assays, the thin-film reactant layer is already so close to the reactive surface that the time required for diffusion perpendicular to the film area is a factor-of-100 less than required for

reactants to diffuse across the horizontal extent of the reactant layer: vertical non-uniformities in the reactant solution will disappear on a time scale short compared to horizontal non-uniformities. Now, if the substrate were uniform over the area of the slide-based experiment, this horizontal diffusion would be irrelevant: each reactant molecule would need only to find the nearest substrate through vertical diffusion. However, efficient use of DNA microarrays demands the placement of multiple different probes over the surface of the slide, which breaks the symmetry of a uniform surface substrate, and necessitates the interrogation of all surface areas by every target reactant molecule for chemical equilibrium to be possible.

In this case, accelerating the horizontal (parallel to the surface) transport of molecules in the aqueous layer may improve the accessibility of the reactive substrate to the reactant and speed the arrival of chemical equilibrium, while accelerating the vertical (perpendicular to the thin film) transport of the same reactants is unlikely to speed microarray reactions as it would for the uniform substrates or bulk chemical reactions.

5.1.2 Coupling of fluid motion from the stirring liquid to the reactant liquid

To accelerate the horizontal transport in the aqueous reactant layer, the liquid-on-liquid mixing system stirs an immiscible overlayer of mineral oil, as shown in Figure 5-1. In this section, I estimate the amount of fluid motion in the aqueous layer as a function of the relative viscosities of the oil and water and the depth of the aqueous layer and the position of the paddle end above the fluid-fluid interface.

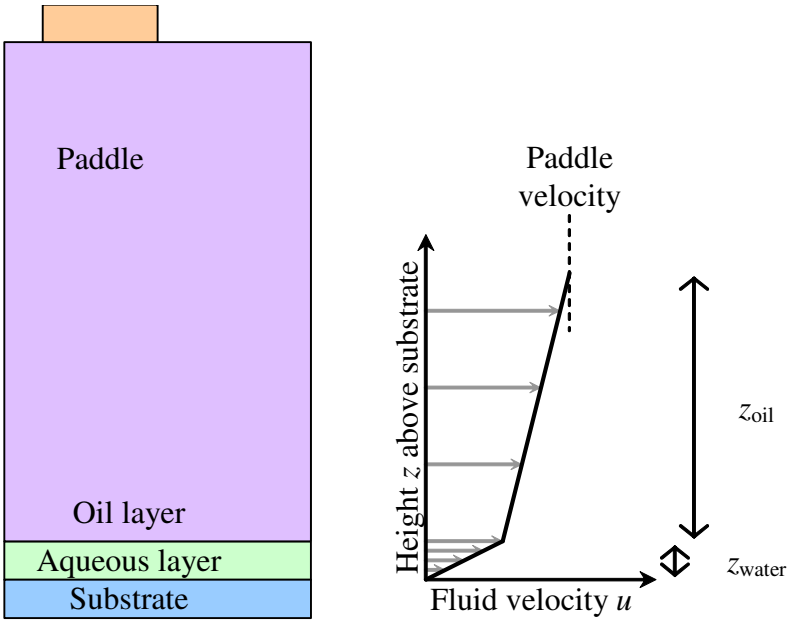

Figure 5-1: Side view of cylindrical liquid-on-liquid mixing chamber with fluid velocity profile (not to scale).

I assume the following boundary conditions:

- At the end of the paddle, the mineral oil stirring fluid velocity $u(z = z_{oil} + z_{water})$ equals the paddle velocity U.
- Mineral oil is a Newtonian fluid with paddle-to-water depth z_{oil} and dynamic viscosity $\eta_{oil} = \rho\upsilon = (0.873\pm0.002\ g/cm^3) \times (0.676\pm0.013\ S) = 0.59\pm0.01\ P$ (for the microarray experiments: heavy mineral oil from Table 2).
- At the oil-water interface, there is a non-slip condition, and the fluid velocities on both sides of the interface $u(z = z_{water})$ are equal.
- The shear stress $\sigma = \eta$[strain rate] is uniform throughout the fluids; in particular, the shear stresses on both sides of the oil-water interface are equal.
- Water is a Newtonian fluid with oil-to-substrate depth z_{water} and dynamic viscosity $\eta_{water} = 0.01$ P at room temperature and 0.00653 P at 50°C (from Table 2).

- At the water-substrate interface, there is a non-slip condition, and the fluid velocity is $u(z = 0) = 0$.
- (Definition:) Newtonian fluids have strain rate equal to the velocity gradient. (Weisstein, 2005)

These boundary conditions are enough to make a rough estimate of the velocity profiles $u(z)$ in the two fluids. Since the shear stresses in the two fluids are equal, we have:

η_{oil}[strain rate in oil] = $\sigma_{oil} = \sigma_{water} = \eta_{water}$[strain rate in water]

η_{oil}[velocity gradient in oil] = η_{water}[velocity gradient in water]

$\eta_{oil} \, (u(z_{oil} + z_{water}) - u(z_{water})) \, / \, z_{oil} = \eta_{water} \, (u(z_{water}) - u(0)) \, / \, z_{water}$

$u(z_{water}) = U \, (1 \, / \, (1 + (\eta_{water} \, z_{oil}) \, / \, (\eta_{oil} \, z_{water})))$

In the immunofluorescence staining, flow visualization, and microarray experiments, the dynamic viscosity of the oil and the thickness of the water layer varied according to Table 5:

Table 5: Parameters used to calculate the fluid velocity at oil-water interface in the immunofluorescence staining, flow visualization, and microarray experiments. Dynamic viscosity is calculated by multiplying kinematic viscosity and density from Table 2. Water layer thickness is calculated by dividing volume of aqueous solution by reaction surface area.

Experiment	Oil dynamic viscosity η_{oil}; ratio η_{oil} / η_{water}.	Water layer thickness z_{water}; ratio z_{oil} / z_{water}.	Fluid velocity $u(z_{water})$ at oil-water interface, as a fraction of paddle velocity U
Immunofluorescence staining (20°C)	> 0.59 P; > 59	50 µm; 78	> 0.43
Flow visualization (20°C)	> 0.21 P; > 21	50 µm; 78	> 0.21
Microarray (50°C)	< 0.21 P; < 33	500 µm; 7	< 0.82

Table 6: Flow rates and Reynolds numbers in the different experiments with the liquid-on-liquid mixing device. The Reynolds numbers were calculated with the estimated flow rates at the oil-water interface, a scale length of 1 cm (the radius of the reaction chamber), and the viscosities of the oil overlayer and water reaction layer from Table 5.

Experiment	Stir rate	Calculated flow rate at oil-reaction layer interface	Reynolds number in overlayer	Reynolds number in reaction layer
Immunofluorescence staining	3.4 rpm	> 0.14 cm/s (acrylic paddle)	> 0.69	> 15
Flow visualization	3.4 rpm	> 0.07 cm/s (acrylic paddle)	> 0.12	> 7.1
	17 rpm	> 0.36 cm/s (acrylic paddle)	> 0.6	> 36
	23 rpm	> 0.48 cm/s	> 0.8	> 48
	40 rpm	> 0.84 cm/s	> 1.4	> 84
	70 rpm	> 1.5 cm/s	> 2.5	> 150
	120 rpm	> 2.5 cm/s (Al paddle)	> 4.2	> 250
	150 rpm	> 2 cm/s (Be-Cu flipper)	> 3.6	> 210
Microarray	6 rpm	> 0.3 cm/s (Be-Cu flipper)	> 0.55	> 50
	145 rpm	< 8 cm/s (Be-Cu flipper)	< 13	< 1200

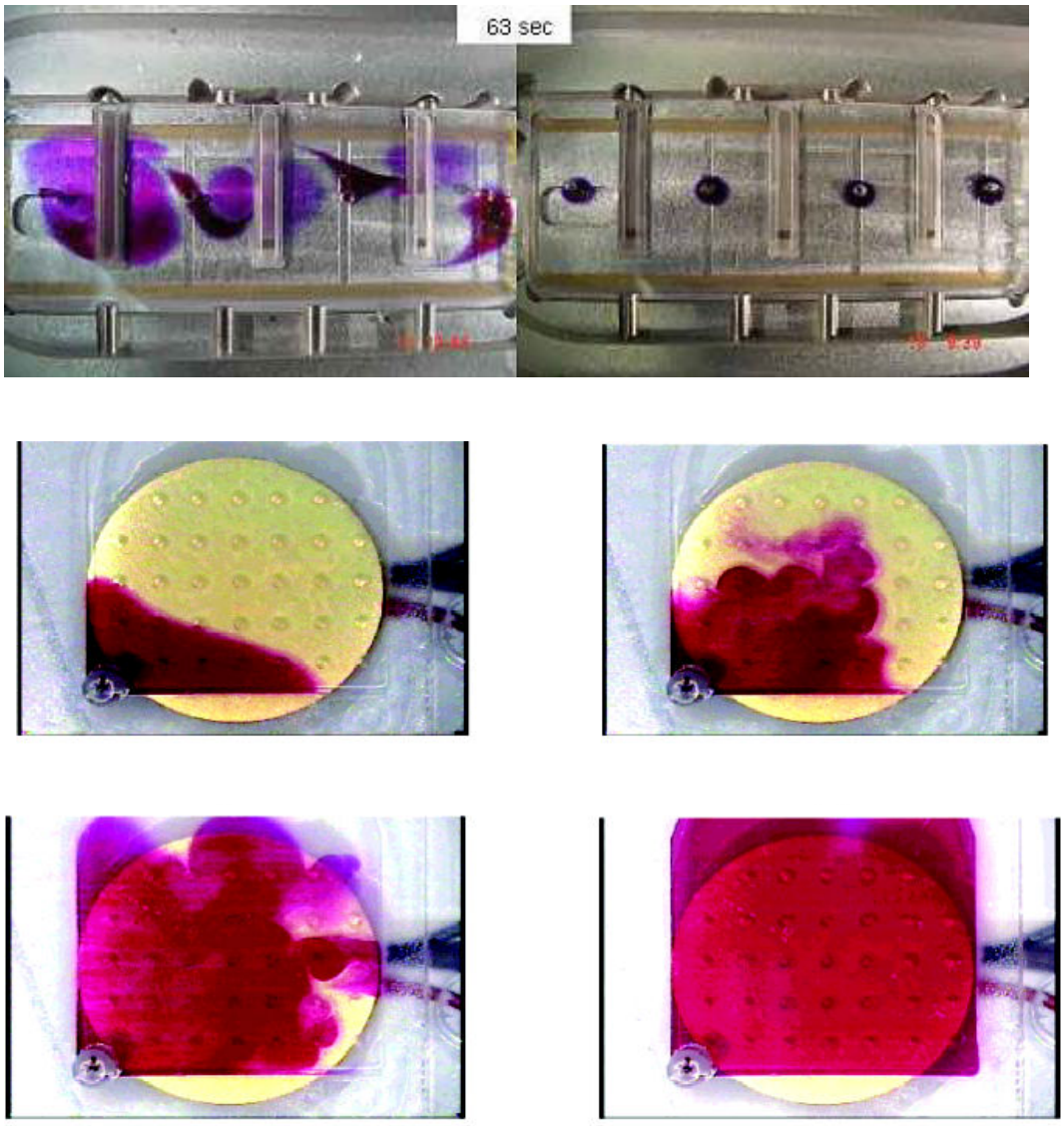

Figure 5-2: Images of dye moved by active micromixing technologies. Two images at top: Advalytix ArrayBooster (from Toegl et al. (2003)). Images taken 63 s apart. Four images at bottom: Motorola Life Sciences cavitation microstreaming project (from Liu et al. (2003)). Each successive image of the 16 mm square chamber was taken at intervals of 2 s.

The order-of-one cm/s flow rates in my experiments are comparable to the flow rates we can estimate by analyzing images of dye movement in other active-mixing technologies (see Figure 5-2).

5.2 Towards an optimal liquid-on-liquid mixing device

What parameters affect the design of the liquid-on-liquid mixing device? A short list of the most important factors would include: size, aspect ratio, substrate characteristics (especially wetting properties with respect to the reactant layer and overlayer), fluid properties, and stirring speed. Some of these factors are constrained by the assay: usually the biological reactant layer is aqueous. Since the rate of reaction is usually proportional to the concentration of the reactant, the reactant concentration should be maintained at a high level. If the reactant is rare, then the small solution volume of a thin aqueous film spread over the reactive surface helps maintain the high concentration. The thin film thickness and the fluid velocity determine the shear rate.

5.2.1 Mixing speed

Considering only mixing speed, recall that the flow visualization experiments demonstrated that the higher mixing speeds tested did appear to spread the colloidal dye at a higher rate than lower mixing speeds; yet the microarray experiments showed little or no significant differences between arrays hybridized with stirring at the high and low speeds. Fluid dynamics tells us that at low fluid flow rates, the fluid motions will be laminar, while high fluid flow rates may produce turbulent motions close to the surface. However, as noted above, the vertical mixing (perpendicular to the substrate) promoted by the turbulent motions would likely not improve the efficiency of the slide-based assay as much as the enhanced horizontal transport (parallel to the substrate), which is already available with laminar flow.

At a sufficiently high stirring speed, the energy dissipated in the shear at the oil-water interface will become comparable to the surface tension there. By then, sufficient energy needed to increase the interfacial area will be available, and bubbles of oil in water or water in oil may form. Even before that point, the energy input may cause greater intermingling of oil and water than in equilibrium. If the interface becomes less-sharply-defined, the no-slip boundary condition at that interface may no longer apply. This effect, bringing the oil phase closer to the substrate and some of the reactant away from the substrate, would probably not improve the efficiency of the slide-based assay.

5.2.2 Shear effects

Another constraint on the rate of stirring could be shear effects that might disrupt or inhibit target-probe hybridization nucleation. I want to estimate the maximum flow or shear rate that will still enable the hybridization reaction to proceed. One way to do this is described in the microarray methods (section 4.2.2), with the argument that if the shear rate is sufficiently high to prevent the polymer's relaxation, then the DNA targets and probes may never be in a configuration where they can hybridize. Since the product $\sigma\tau$ was close to unity for the 6-rpm stirring rate used in the microarray experiments, we can read from Table 6 that the flow velocity at the oil-water interface was 0.4 cm/s, with a Reynolds number in the overlayer of approximately 0.6. (If this argument is valid, then the microarray hybridization reactions stirred at 145 rpm should have resulted in subdued efficiencies. The data do not rule out this possibility.) The Reynolds number for the immunofluorescence staining experiments was 0.3. These Reynolds numbers are far smaller than those (10^3 or higher) at which turbulent motions develop, so the flows in the overlayer in both

series of experiments were laminar, and an ideal liquid-on-liquid mixer for long cDNA targets will also require laminar flows throughout.

It is also possible to calculate the velocity that would produce a drag force on the single-stranded free end of a partially-hybridized duplex sufficient to unzip the probe-target combination, but this strategy leads to a shear rate of 10^5 s^{-1}, which does not help bound our problem. (If we pretend that the unhybridized portion of the target is 1 kb long and assumes a globular shape with a density equal to water, then the radius of this globule will be roughly $a = 0.5 \times 10^{-6}$ cm. For the Stokes drag force $6\pi\eta aU$, where η is the viscosity of the solvent, a is the radius of the sphere, and U is the flow velocity, to exert the 14 ± 2 pN (from quasi-equilibrium DNA unzipping studies; see Koch et al., 2002) on such a globule in water, the flow velocity U must be on the order of 10 cm/s. This latter condition is likely not the correct explanation of the lack of hybridization enhancement: such a flow velocity at a distance the length of a ssDNA probe from the surface would imply a shear rate of 10^5 s^{-1}, which would be enough, given the first argument cited above, to straighten even a trinucleotide target.)

Oligonucleotide-probe arrays, by contrast, have probe- and target-lengths between 20 and 100 nt. The shorter probes bring the critical hybridization step 10–50 times closer to the surface of the slide, where the non-slip boundary condition requires fluid velocities to approach zero. The shorter target molecules relax 50-500 times faster than the 1-kb target molecules used in my experiments, and this factor may allow faster mixing speeds to be used, although the Reynolds numbers may still fail to reach 10^3, and fluid motions in the overlayer will likely remain laminar.

5.3 A dynamical systems view of stirring

Dynamical systems theory is the modern study of the time evolution of systems under fixed, deterministic rules. I will describe stirring from this perspective

by mapping phase portraits of mixing systems. I will consider steady, laminar flows; periodically-forced laminar flows; and turbulent flows. In this section, I draw heavily on Sethna (2006).

5.3.1 Mixing with steady flows

In Hamiltonian dynamics, Liouville's theorem implies that volumes in phase space remain constant even as they evolve to new places and shapes. Incompressible fluids have the same condition in physical space. Steady, laminar flows are non-dissipative and time-reversible, stretching and reshaping fluid particles.

The stretching in three-dimensional real space is characterized by three Lyapunov exponents, which govern the change in shape of the fluid particle volume. Since the volume is constant, the three Lyapunov exponents must sum to zero. Aside from the case where all three exponents are zero, if any one exponent is nonzero, then the fluid particle will be stretched and thinned. After a sufficiently long time, every fluid particle experiencing the same flow and with the same Lyapunov exponents will be stretched throughout the volume originally inhabited by those same fluid particles.

If the entire reaction volume participates in this stirring and has the same Lyapunov exponents, then some part of every fluid particle will eventually be arbitrarily close to every position in the reaction volume. This stirring process is ergodic, which is a sufficient condition for the "good" stirring previously described (for microarrays, that which would bring every reactant target molecule sufficiently close to interrogate every substrate probe).

If the reaction volume has two or more regions that experience different amounts of steady stirring, the Lyapunov exponents in each region will be different. There will be distinct closed cycles in phase space between which the stirring alone cannot mix particles. The flow is non-ergodic. The KAM theorem shows that the

likelihood of this non-ergodic behavior is high for systems with small numbers of particles.

Steady flow in two dimensions is never chaotic: incompressible fluids cannot have flow fields adding fluid to or removing fluid from a constant volume, so fluid particles must travel in closed, nonintersecting cycles instead of spiraling in or out of a region. Such closed trajectories offer no opportunity for random fluctuations to bring chaotic behavior to the flow. In my immunofluorescence staining, flow visualization, and microarray experiments, the 1-cm radius reaction layer was 0.005–0.05 cm thick: thin, but not two-dimensional. For the thin third dimension to support chaotic mixing, there must be vorticity within that thickness. Such fluid motion is possible, for example, in Stroock's microfluidic mixer (2002). In my experiments, however, there is no clear evidence for or against this vorticity.

5.3.2 Mixing with periodically-forced laminar flows

For periodically-forced flow, complex-valued Floquet exponents generalize the real-valued Lyapunov exponents in describing the change per period. In the same way that the Bloch theorem gives wave solutions to the Schrödinger equation with a space-periodic potential in the Hamiltonian, Floquet's theorem shows that periodically-forced dynamical systems (expressible with a time-periodic potential in the Hamiltonian) have solutions of the form: $\varphi(t) = P(t)\exp(tB)$, where $P(t)$ is time-periodic with the same period T as the forcing, B is a constant (complex) matrix, and the eigenvalues of $\exp(TB)$ are of the form $\exp(\mu T)$. Then, the often complex-valued μ are the Floquet exponents. (Ott, 1993, pp. 354–357)

Time can be thought of as an additional dimension, and chaotic patterns have been shown to develop in two-dimensional blinking-vortex flows (Aref, 1984) and journal-bearing flows (Ottino, 1989). Two-dimensional periodic flows do not

necessarily show chaos, though: particularly if the stream lines during one part of the period do not intersect the stream lines during any other part of the period. Several of my flow-visualization experiments revealed annular flow patterns with no radial mixing, even with randomly-reversing, swinging-chain paddles. It was a surprise that these paddles, with stirring patterns expected to be more random, reproduced the same KAM surfaces seen in the flow visualization experiments with the ordinary, flat paddle performing steady rotation.

5.3.3 Mixing with turbulent flows

Unlike laminar flows, turbulent flows exhibit vorticity and energy dissipation at all length scales. This prompts a different dynamical-systems description of mixing. Berkooz et al. (1993), citing Téman (1988), say that "any dynamical system which captures all of the relevant spatial scales will be of enormous dimension." To give an idea of this, a snapshot of the flow velocity at every point in real space is a vector field that can be represented with some large sum of Fourier components. High frequencies in a typical power spectrum of turbulence are limited by the fluid's viscosity. This infinite space of independent functions will have an infinite set of particle trajectory solutions, each of which may have a Lyapunov exponent. Instead of using three Lyapunov exponents to describe the evolution of fluid particle shapes in real space, we have an infinite family of Lyapunov exponents. These exponents can be used to estimate the rate of divergence of nearby initial conditions, with better mixing available with a larger number or magnitude or both of positive exponents.

Sreenivasan (1991) disagrees with this description, saying, "Turbulent eddies are spatially compact structures, not Fourier modes with infinitely extended support." Berkooz et al. (1993) suggest that this degree of complexity may be unnecessary, recommending instead their "proper orthogonal decomposition" (POD), also known as

Karhunen-Loève decomposition and principal components analysis. The POD decomposition can still produce an infinite number of nonzero eigenvalues.

All turbulent flows are chaotic, but not all chaotic flows need be turbulent. For example, non-turbulent low-shear chaotic flows produced by aperiodic stirring can also mix the reactant solution. This is fortunate, because the maximal Reynolds numbers for flows in my experiments (Table 6) are too low to force a diagnosis of turbulence. I previously noted that some non-chaotic fluid motions can also be efficient at delivering material from a reactant solution. But which would mix the fastest? Experimental observations of increased Lyapunov exponents at higher Reynolds numbers in Taylor-Couette flow (Brandstäter, et al, 1983) and in a microchannel (Xia, et al, 2006) suggest that high-shear flows may indeed mix faster. In my experimental configuration, all methods of mixing require diffusion to carry the reactants to the surface-bound substrate. Here, the higher shear rates from the turbulent flow would slightly thin the diffusion boundary layer compared with the non-turbulent flows, reducing the time needed to cross.

5.3.4 Blend time estimates versus contemporary dynamical systems theory

It is clear that a complete description of mixing is far richer than a simple blend time. Among my flow visualization experiments, we can see examples where mixing covered different amounts of the reaction surface. The blend time in those cases described only the initial scrambling, and not any long-time-scale features, nor the areas that did not mix.

5.4 Future experiments

The above discussion suggests questions to be addressed in future experiments, which could help illuminate a microscopic explanation of how the liquid-on-liquid mixing might affect DNA hybridization. These include: did the stirring inhibit DNA-

DNA hybridization by exerting sufficient shear to disrupt DNA secondary structures? Did the oil wet the microarray surface or mix with the water and inhibit target DNA hybridization?

5.4.1 Single-stranded DNA secondary structure

Since the product literature for the Advalytix ArrayBooster device reports a large difference in the hybridization enhancements of short oligonucleotide and long cDNA targets (and other hybridization station manufacturers tend to report only oligonucleotide results), the estimates in the geometry section above make us wonder whether any agitation, while helping to transport the target DNA molecules across the reaction surface, might inhibit the hybridization process by affecting the secondary structure of long target or probe DNA molecules. The experiments applying stirring interrupted with pauses were an attempt to test this possibility; while no significant difference was seen between the hybridization efficiencies obtained with and without the 19-second pauses, lower duty cycles (longer pauses) might offer a productive compromise between large-distance-scale transport and small-time-scale shear. Another way to test this hypothesis is to perform oligonucleotide-target hybridizations to oligonucleotide-probe arrays in the liquid-on-liquid mixing reactor and check for hybridization enhancement. Alternatively, we could cut the long target DNA molecules into shorter fragments prior to hybridization with the long probe cDNA arrays. The difference between these two possible experiments would address the effect of higher flow velocities in far-from-surface hybridizations that the long probe cDNAs would have to undergo.

5.4.2 Other failure modes

In our experiments, we noted that the mineral oil used in the stirred overlayer tended to wet the coated glass microarray slides. On several slides, the oil even

displaced the aqueous reactant and no hybridization occurred. If the presence of oil were inhibiting the hybridization reaction, it would be appropriate to re-test the glass coverslips, slowly rotated as in Carl Franck's 2000–2002 experiments.

6 CONCLUSION

I studied a system that was intended to provide convective fluid motions in thin-film reactions. This appeared to provide dramatic improvements in the banding quality of immunofluorescent staining of polytene chromosomes at short times or low antibody concentrations, but the increase in efficiency, uniformity, sensitivity, and specificity of microarray hybridizations was negligible. Further studies are needed to resolve the apparent inconsistency between these two results.

7 APPENDIX: DNA PROBE AND TARGET PRODUCTION

The DNA molecules used as the microarray probes and target were prepared by PCR. The recipes are below:

7.1 Probes: Conventional PCR

Recipe:

ddH20:	182.6 µl
template resuspended (E. coli D4889)	8 µl @ 0.125 µg/µl
betaine	120 µl @ 5M
10x PCR buffer	40 µl
$MgCl_2$	32 µl @ 25 mM
forward primer	5.0 µl @ 40 µM
reverse primer	5.0 µl @ 40 µM
dNTP mix	3.2 µl @ 25 mM
Taq	4 µl @ 5 U /µl

Thermocycler program for conventional PCR was:

1: 95°C for 5 minutes 2: 58°C for 1 minute 3: 72°C for 3 minutes

4: 95°C for 1 minute 5: 58°C for 1 minute 6: 72°C for 3 minutes

7: Goto Step 4 27 times

8: 95°C for 1 minute 9: 58°C for 1 minute 10: 72°C for 5 minutes

11: 4°C for 10 hours 12: End

7.2 Target: Linear PCR

prepare 80 µl "modified 2.5 mM dNTP mix":

2 µl of dATP 100 mM

2 µl of dGTP 100 mM

2 µl of dCTP 100 mM

74 µl of ddH_20

prepare 80 µl makeup dTTP(final conc 1mM):

0.8 µl of dTTP @ 100mM in 79.2 µl ddH2O

Prepare both labeled and unlabeled ssDNA target by linear PCR and unlabeled dsDNA by regular PCR as test in 50 µl reactions each.

Thermocycler program for linear PCR was:

1: 94°C for 2 min 40 sec	2: 58°C for 1 min	3: 72°C for 1 min 30 sec
4: 94°C for 40 sec	5: 58°C for 1 min	6: 72°C for 1 min 30 sec
7: GOTO step 4, 44 times		8: 72°C for 5 min
9: 4°C for 10 hours	10: END	

Recipes:

	Labeled ssDNA	Unlabeled ssDNA	Unlabeled dsDNA
ddH_20	9.3 µl	9.3 µl	8.7 µl
Sequence b1771 Protocol 2 product (7/23/03 A, 58C) (0.138 µg/ µl)	3.6 µl	3.6 µl	3.6 µl
Betaine 5 *M* (optional: can be H_2O)	15 µl	15 µl	15 µl
10X PCR Buffer	5 µl	5 µl	5 µl
MgCl2 @ 50mM	2 µl	2 µl	2 µl
Sequence b1771 reverse primer 40 μM	0.6 µl	0.6 µl	0.6 µl
Sequence b1771 forward primer 40 μM	0	0	0.6 µl
modified dNTP @ 2.5mM	4.0 µl	4.0 µl	4.0 µl
makeup dTTP @ 1mM	3.4 µl	10 µl	10 µl
CyDye Fluorescent Nucleotides: Fluorolink Cy3-dUTP, 1 *mM*, (sold in 25-µl aliquots, PA53022, $295 from APBiotech)	6.6 µl	0	0
Taq pol 5U/µl	0.5 µl	0.5 µl	0.5 µl

8 APPENDIX: MICROARRAY SCANNER CALIBRATION

8.1 Introduction

This appendix describes the microarray scanner and my calibration. It is organized in the following sections: characteristics of the scanner; calibration slide characteristics and scanning method; correction for the scanner's power fluctuations; conversion factors between different scan power and photomultiplier tube voltage settings; measurement of fluorescence intensity yield from known quantities of my labeled target DNA.

8.2 Scanner Characteristics

The Axon GenePix 4000B is an instrument designed to scan fluorescent microarrays. This unit contained two lasers for fluorescence excitation at 532- and 635-nm wavelengths and two photomultiplier-tube-based fluorescence emission detectors. For the microarray experiments described in this thesis, I used only the 532-nm laser and its corresponding photomultiplier tube detector, leaving the 635-nm laser and the other corresponding detector turned off. All further description will refer to the 532-nm excitation-detection system.

8.2.1 Scanner Parameters

There are seven user-selected parameters that control the behavior of the scanner and software: whether the laser and corresponding detector are in use, the photomultiplier gain (voltage), scan power (intensity), the resolution, the number of neighboring scan lines whose intensities are to be averaged, the height of the focal plane away from the slide surface, and the scan area.

I set the photomultiplier tube gain (voltage) at 600 V, 700 V, or 800 V: low enough so that the measured fluorescence emission intensities would not saturate the

detector and noise would not be too large, and high enough to read a signal from the microarrays. Most microarrays were scanned at the 800 V setting. I later converted all my data to be expressed in intensity units relative to a model calibration slide.

I always scanned microarrays at the 100% scan power setting. The instrument provides two other scan power settings available — stated to be 33% and 10%, but for this particular instrument, closer to 38.3% and 17.3% respectively — by attenuating the excitation laser output with neutral density filters. This is to be distinguished from the instrument's self-measured laser output, which is described below.

I set the scanner's resolution to 10, 20, 40, or 100 µm, depending on the expected size of the fluorescent spots on the slide, choosing the resolution so that pixels on the boundary between feature and background regions (described later) would not be too large a fraction of the sample. In every case, there were at least several hundred pixels in each fluorescent spot and a thousand pixels in the associated background. I never averaged neighboring scan lines (lines to average was always set to 1). For all the experiments reported here, the focal position was set to 0 µm: at the surface of the slide. The scanner can detect fluorescence signals in a field depth of ten microns, but there is significant attenuation at and beyond that point.

The scan area was a rectangular region set to include all array fluorescent spots with a visual margin of at least three diameters of the fluorescent spot closest to the edge. This is double the margin needed for the GenePix Pro software's measurement of the local background region of any fluorescent spot — all the non-foreground pixels within a disk of diameter three times the fluorescent spot diameter, centered on the fluorescent spot.

8.2.2 Scan Data

For each scan, the scanner software records the seven user-selected parameters described above and three other parameters: the temperature of the scanner in degrees C, the laser output power in terms of an internal photosensor voltage, and the age of the laser in power-on minutes. Each pixel in the scan area is assigned a 16-bit intensity value. The GenePix Pro 4.0.1.23 software segments the image into user-defined circular "feature" areas centered on the fluorescence probe spots and associated background regions. For elliptical or otherwise non-circular probe spots, the feature boundary encloses the minor axis. For each fluorescent spot, the software reports the position, the diameter, the median, mean, and standard deviation of foreground and background pixel intensities, the percentage of foreground pixels one and two standard-deviations above the background, and the number of foreground and background pixels.

I choose the median pixel values to represent the feature and background intensity because, compared to the mean, the median is less sensitive to eccentric fluorescent spot shapes and noise such as spurious scattering from dust particles. In most cases, there is an insignificant amount of noise, and the median is very close to the mean. I define the integrated intensity of a fluorescent spot to be the median-background–subtracted median foreground pixel intensity multiplied by the number of foreground pixels in the fluorescent spot.

Sporadic scanned images contained unexpected streaks, graininess, Moiré-like patterns, or wholesale changes in intensity, as shown in Figure 8-1. I attributed these spurious results to power fluctuations and discarded all images where I observed these artifacts, re-scanning the slides in every case.

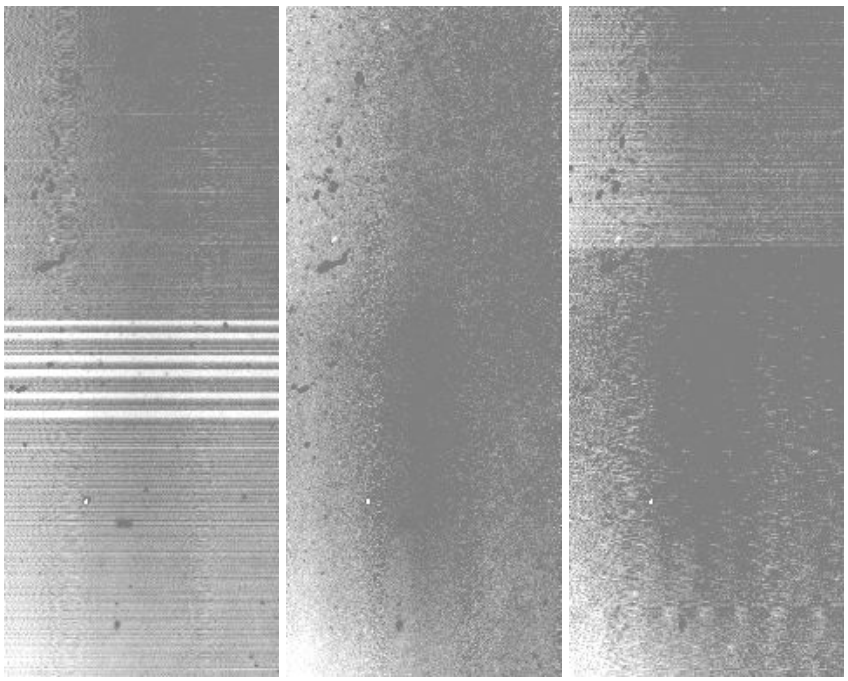

Figure 8-1: Scans of the GP8 calibration slide sometimes revealed spurious artifacts including changes in intensity, Moiré-like patterns, and graininess.

I measured the photomultiplier tube dark current by scanning with no slide in the slide holder. The dark currents measured at different scan powers (10%, 30%, 100%) and photomultiplier tube voltages (600 V, 700 V, 800 V) had statistically significant but not practically significant differences; the average level was 41.1 +/- 1.6 scanner units.

8.3 Calibration Slide and Scanner Fluctuations

8.3.1 GP8 Calibration Slide

Axon supplies several calibration slides, labeled "GP8", for use with the 532-nm laser. These are made of plastic embedded with a bleach-resistant fluorescent dye. Although they may appear uniform and identical to the naked eye, these calibration slides exhibit different spatial fluorescence variations when scanned, as shown in

Figure 8-2. I selected the rightmost of these slides and will confine my analysis to that slide.

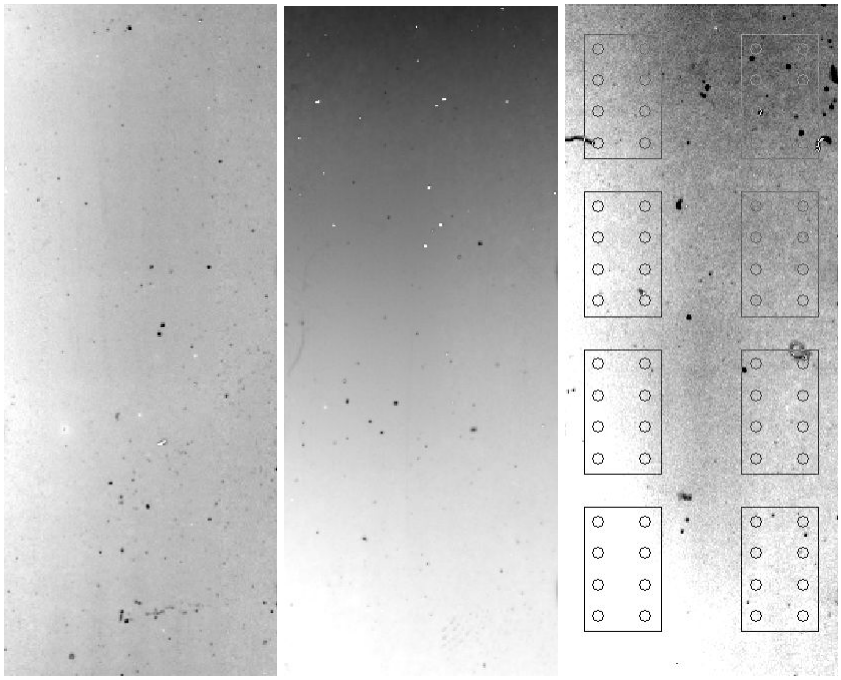

Figure 8-2: Calibration slides. The contrast has been exaggerated to show differences. The rightmost slide was used for subsequent calibration of the scanner. The 64 circles appearing on the rightmost slide indicate the regions where the median intensities were computed; the arithmetic mean of those medians was used to represent the intensity of the calibration slide. The intensity variation over the surface of the slide (expressed in the ratio of the standard deviation of the medians to the mean of the medians) is some ±2.2% for the left slide, ±17% for the center slide, and ±2.3% for the right slide. (Left and center slide scans courtesy of Benjamin Smith, 30 March 2005.)

8.3.2 Scanner warm-up time

Axon recommends waiting for a warm-up period — to be determined by the user — before scanning microarrays. To find a suitable warm-up time, I scanned the GP8 calibration slide repeatedly with a PMT gain of 700 V and a scan power setting of 100%, trying to discover an appropriate time for the intensity signal to settle. I sampled 64 circular regions over the surface of the calibration slide, denoted by the circles in Figure 8-2, and computed the mean of the 64 areas' median pixel intensities. These are shown in Figure 8-3.

The positioning of the calibration slide within the scanner's slide holder may have varied as much as 1 mm in the direction parallel to the long edge of the slide, so the 0.7-mm (diameter) circles may cover different areas in different scans. However, the local intensity variation is small compared to the 3% intensity variation over the entire surface of the slide, which in turn is small compared to the 10–15% intensity variation on any given day's scans shown in Figure 8-3.

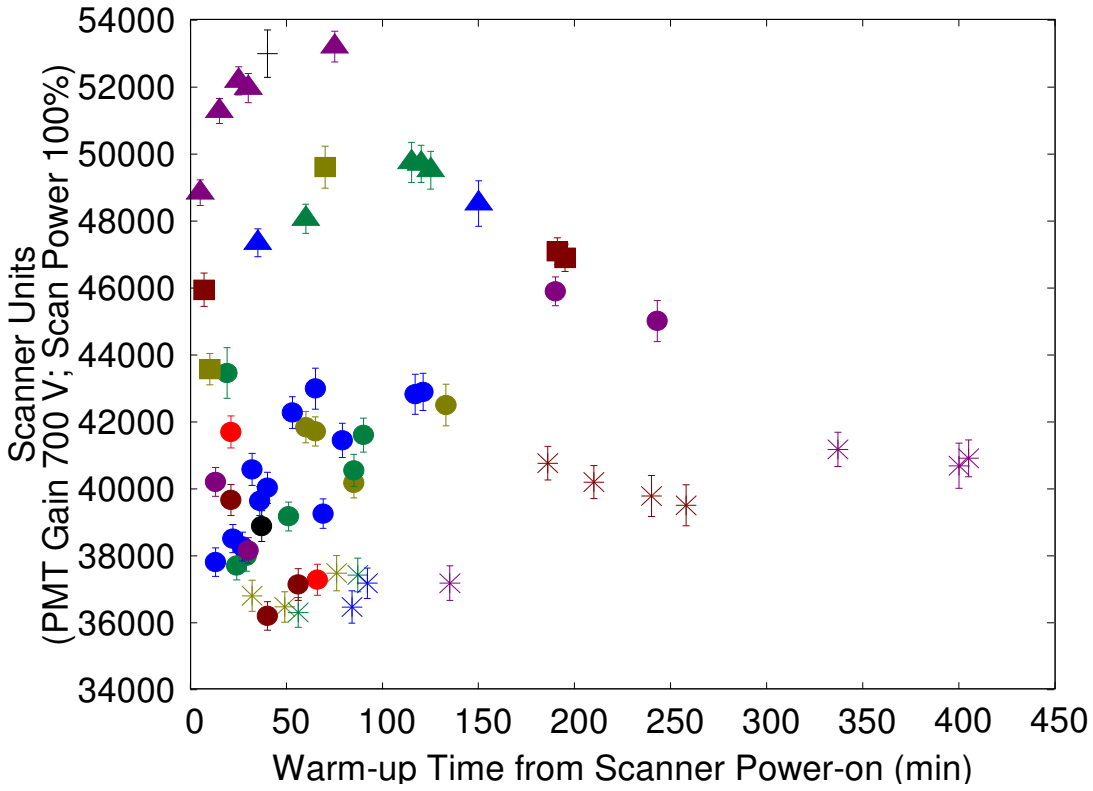

Figure 8-3: Mean of median fluorescent spot intensities from repeated scans of the calibration slide (scanner units at 700 V PMT gain and 100% laser power) show large day-to-day differences (10–15%) and a long-term trend to lower intensities. The symbols denote the month in 2004 when the slide was scanned: cross (+) April; filled triangle (▲) May; filled square (■) June; filled circle (●) July; asterisk (×) August. The error bars show the standard deviation of the median intensities.

8.3.3 Decrease in scanner sensitivity over time

It is clear that factors other than warm-up time affect the response of the scanner. Figure 8-4 shows the same data (Mean of Foreground Medians) plotted against the three scanner parameters: temperature, laser power, and laser-on time (age in minutes). The clearest trend is a 20–30% decrease in the calibration slide's fluorescence intensity with the laser-on time. The fluorescence intensity should depend directly on the measured laser power (e-mail communications from Dr. Mike DeFreitas, manager of Axon technical support, 10 February 2005 and 31 March 2005) and the efficiency of the fluorophore. To determine whether the slide's intrinsic fluorescence decreased, perhaps due to photobleaching, or whether the scanner had changed, I considered scans of a second GP8 calibration slide, one recorded at the beginning of my work, and one (courtesy of Benjamin Smith) much afterwards. If my selected calibration slide had been photobleached, then the second calibration slide, with much less scan exposure, should show only the changes in the scanner. It turns out that the second calibration slide also showed a large decrease in fluorescence intensity, and using this comparison, I calculated the reduction in intensity of my selected calibration slide to be less than 0.033% per scan, which could account for at most a 2.7% reduction in intensity over the 83 scans of the calibration slide. Most of the change must be due to some other effect, perhaps optics falling out of alignment.

Figure 8-4: Trellis graph of GP8 calibration slide scan data showing plots of all pairs of the five parameters: scanner temperature in Celsius, measured laser power in sensor voltage, laser age in powered-on minutes, mean of medians of 64 disks on selected GP8 calibration slide, and standard deviation of the medians. There are twenty plots in all, showing all ten pairs of parameters. The panes along the major diagonal contain the name of the parameter plotted in the intersecting row and column, and a histogram showing that parameter's distribution.

The clearest trends are a decrease in the calibration slide intensity (Mean of F Medians) with the age of the scanner (LaserOnTime), and a slight increase in the intensity variation (StDev of F Medians) with the laser intensity (LaserPower).

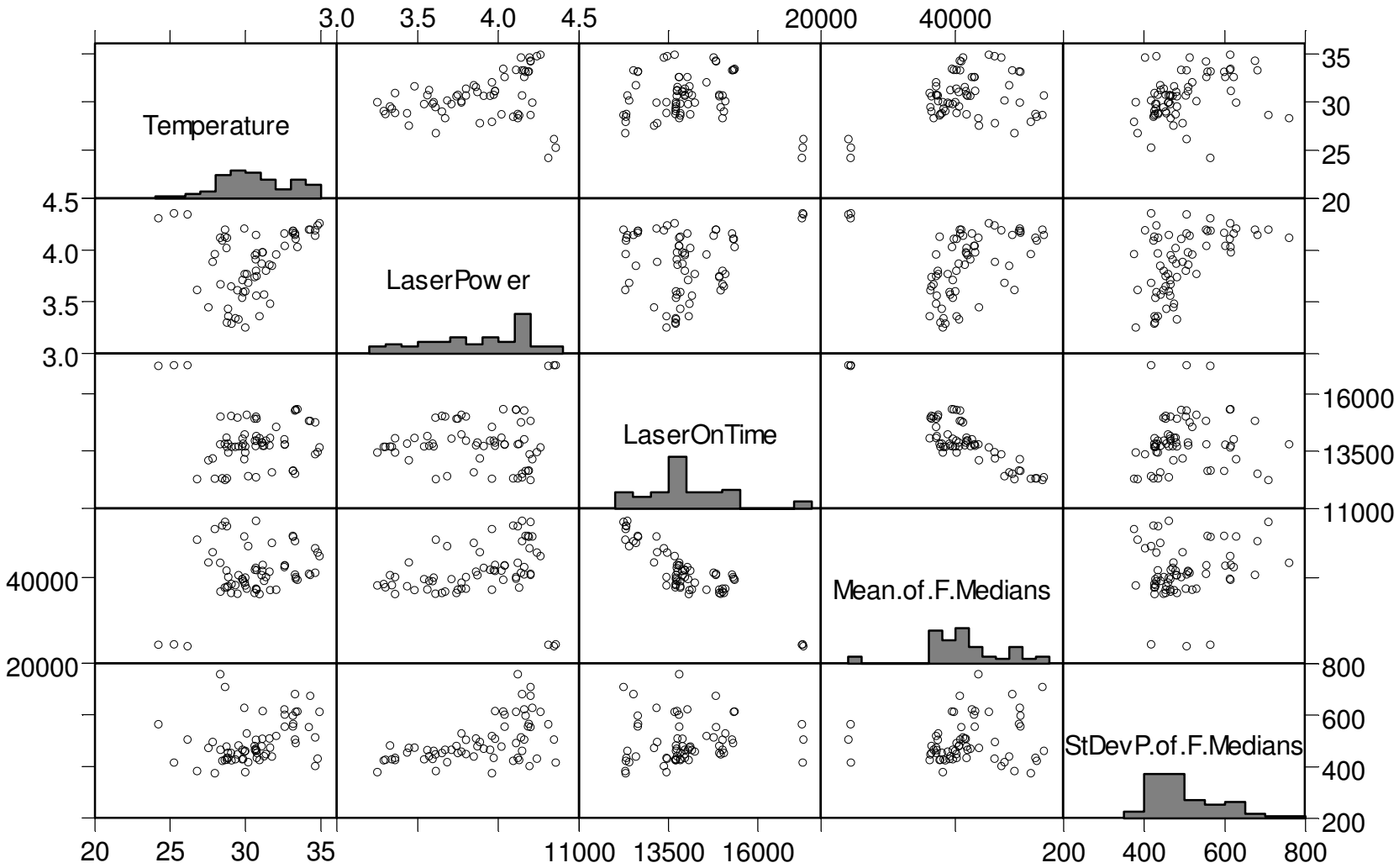
Temperature
LaserPower
LaserOnTime
Mean.of.F.Medians
StDevP.of.F.Medians
3.0
3.5
4.0
4.5
20000
40000
35
30
25
20
4.5
4.0
3.5
3.0
16000
13500
11000
40000
20000
800
600
400
200
20
25
30
35
11000
13500
16000
200
400
600
800

8.3.4 GP8 calibration slide intensity model

To correct for the decrease in scanner sensitivity over time, I made a model of the GP8 calibration slide intensity. For simplicity, I will ignore the photobleaching effect and fit the intensity data (formally, the mean of the median fluorescence intensities measured from scanning the GP8 calibration slide data) with a plane:

$$I = A \cdot P + B \cdot T + C$$

where I is the model intensity, P is the LaserPower measured by the scanner's internal sensor in volts, T is the LaserOnTime (age of the laser) recorded by the scanner in minutes, and A, B, and C are fitting parameters. A Marquardt-Levenberg algorithm fits a plane to the data taken April-August 2004 (contemporaneous with most of the microarray data) with:

$A = 7{,}980 \pm 650$ sc/V

$B = -4.43 \pm 0.23$ sc/min

$C = 72{,}600 \pm 4{,}100$ sc,

where sc denotes absolute scanner units at PMT Gain 700 V and 100% scan power. This model has no physical meaning, but it does predict that the scanner will stop working after about 20,000 power-on minutes, which is much less than the typical laser lifetime of 10,000 hours. The residuals from this fit appear in Figure 8-5. Inclusion of a photobleaching factor does not strongly affect the fit. Intensities from scans of the calibration slide in late March 2005 (courtesy of Benjamin Smith) are not coplanar with this fit, which suggests that the change in the scanner has accelerated.

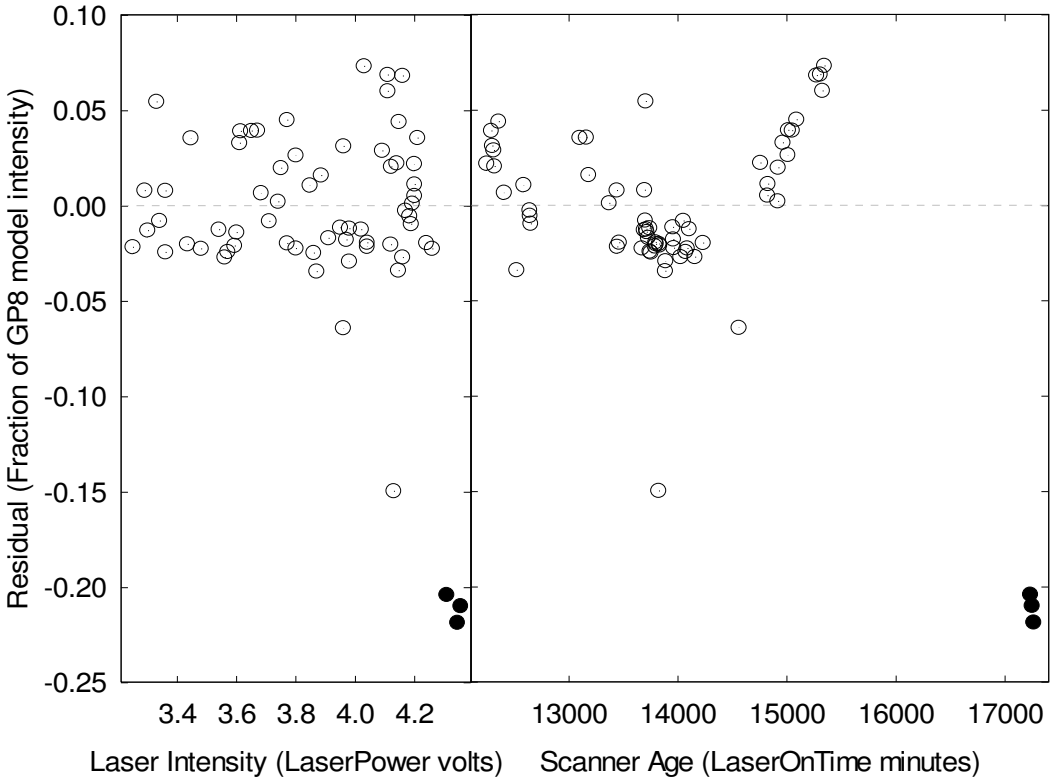

Figure 8-5: Residuals of GP8 calibration slide fluorescence intensity after fitting to a model accounting for laser output power and scanner aging, as a fraction of the model intensity. The residual from each scan appears twice: at the laser intensity and at the scanner age. Open circles (○) denote scans from April–August 2004; filled circles (●) were scanned in March 2005 and are excluded from the model. The standard deviation of the 63 open-circle residuals approximates the uncertainty in the model value: ±3.5%.

8.3.5 Implications for scan data

Any long-term reduction in the excitation efficiency or detector sensitivity would affect the calculation of the absolute efficiency of hybridization, because the efficiency calibration data were obtained before most of the microarray hybridizations were scanned. The reduction would not affect the ratio of stirred and unstirred

hybridization efficiencies or the measurement of cross-hybridization, since each slide represents a complete differential measurement.

I will adjust the scanner data by normalizing them to the intensity of the model GP8 calibration slide. This may seem to be a complication, but it is necessary because the meaning of a scanner unit has changed over the lifetime of the experiment.

8.4 Calibration of Scanner Photomultiplier Tube Voltage Settings

Scan data acquired at the 700 V photomultiplier tube gain setting can be directly normalized with the GP8 calibration slide intensity model described above. However, most of the scan data were acquired at the 800 V PMT gain setting, where the calibration slide's fluorescence emission upon a full-power scan saturates the detector.

In order to compare fluorescence intensities measured with different scanner photomultiplier tube voltage settings, I must obtain conversion factors for the intensity measured at different scanner settings. To do this, I scanned a slide spotted with fluorescently-labeled target DNA (shown in Figure 8-6(b)) and the calibration slide at those settings. Then, I computed the mean ratios of the median intensities after first subtracting either the background or the dark-current, respectively. These results appear in Table 7 and Table 8, below. The calculation of each weighted mean was performed as per Taylor (1982).

I will use the weighted-mean factors obtained to scale the GP8 calibration slide model calculated in the previous section to PMT Gain 800 V scanner units before using the model to normalize the intensity data.

Table 7: Ratio of slide intensity at PMT Gain 800 to signal at PMT Gain 700.

Ratio ± SEM	Method
2.696 ± 0.003	Scanned GP8 calibration slide with scan power 10% and took mean of simple ratios (no correction for photobleaching).
2.745 ± 0.003	Scanned GP8 calibration slide with scan power 33% and took mean of simple ratios (no correction for photobleaching).
2.718 ± 0.013	Scanned homemade fluorescently-spotted slide with scan power 100% at PMT Gain 800, PMT Gain 700, and PMT Gain 800 and took mean of geometric mean ratios (automatically correcting for photobleaching).
2.720 ± 0.002	Weighted mean of above

Table 8: Ratio of slide intensity at PMT Gain 700 to signal at PMT Gain 600.

Ratio ± SEM	Method
3.173 ± 0.003	Scanned GP8 calibration slide with scan power 100% and took mean of simple ratios (no correction for photobleaching).
3.220 ± 0.018	Scanned homemade fluorescently-spotted slide with scan power 10% at PMT Gain 700, PMT Gain 600, PMT Gain 600, and PMT Gain 700 and took mean of geometric mean ratios (automatically correcting for photobleaching).
3.236 ± 0.012	Scanned homemade fluorescently-spotted slide with scan power 33% at PMT Gain 700, PMT Gain 600, and PMT Gain 700 and took mean of geometric mean ratios (automatically correcting for photobleaching).
3.20 ± 0.10	Scanned homemade fluorescently-spotted slide with scan power 100% at PMT Gain 700, PMT Gain 600, and PMT Gain 700 and took mean of geometric mean ratios (automatically correcting for photobleaching).
3.178 ± 0.003	Weighted mean of above

8.5 Fluorescence intensity yield per quantity of labeled target DNA

I want to measure the efficiency of the hybridization process: how much of the labeled target DNA present in the hybridization reaction adsorbs to the probe spots. I will do this by integrating the intensity of the fluorescence signal over the area of the probe spots and comparing this quantity to the total fluorescence expected from the amount of DNA in the target solution.

I measured the total fluorescence expected from the labeled target DNA by placing known diluted volumes of the stock labeled target DNA (produced above) onto glass slides, allowing the DNA spots to dry, and scanning these spots. I applied the labeled target DNA to the slide surface in two ways: using a pipette to drip microliter-scale volumes, or using the microarray printer to print nanoliter-scale volumes. Example slides generated using each method appear in Figure 8-6.

(A) 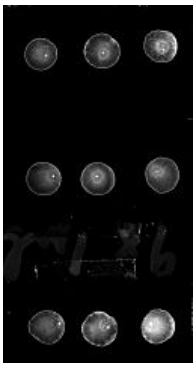 (B) 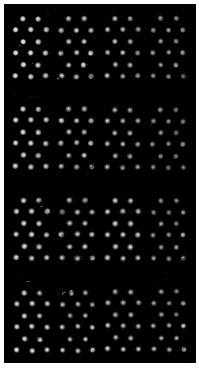

Figure 8-6: Slides bearing fluorescence molecules for use in calibration. (A) Slide ttr17 (16-Dec-2003) bearing nine dried 1-µl pipetted drops of stock target solution diluted 1:20 v/v in 50% v/v DMSO. (B) Slide ttr23 (4-Feb-2004) bearing 240 dried assumed 14-nl pin-printed drops of stock target solution diluted roughly 1:100 v/v in estimated 60% v/v DMSO.

The results of the calibration and fit curves appear in Figure 8-7. The integrated intensities of the pipetted DNA spots appear to scale linearly with the volume of stock labeled target DNA, as expected, and the volume of the spots does not seem to affect the fluorescence quantitation. I assume the microarray printer's spots contain 14 nl of solution (e-mail from Dr. Patricia Koutz, Director of Research at V&P Scientific, the manufacturer of the microarray printer) with a coefficient of variation of 5%.

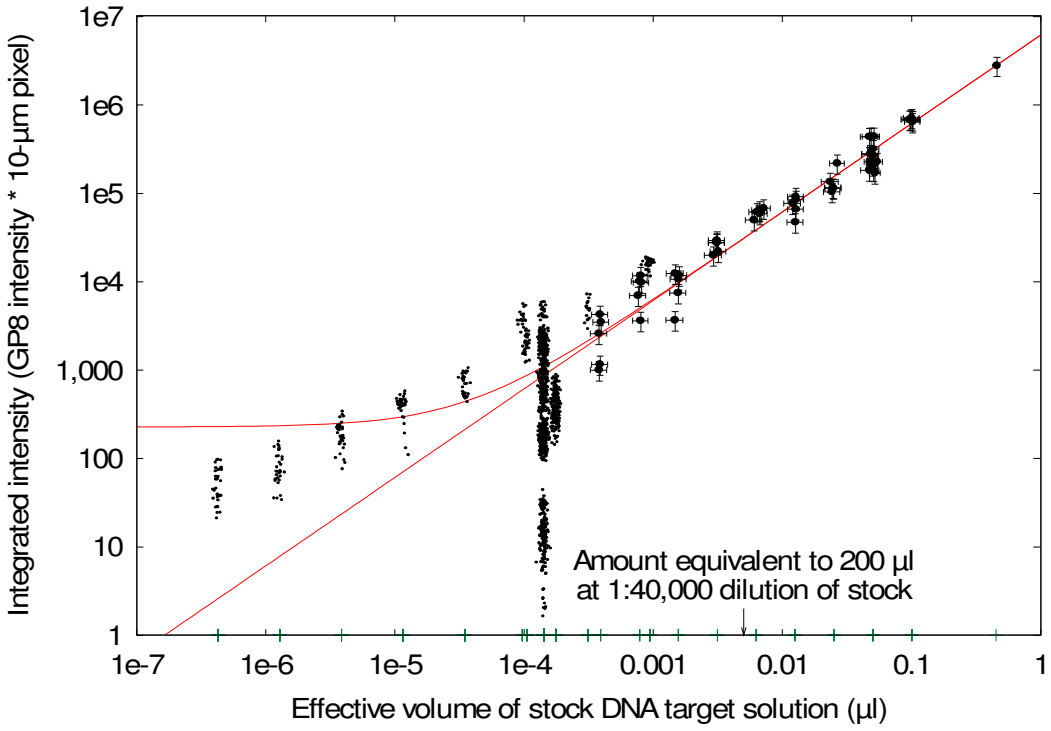

Figure 8-7: Integrated intensity calibration curve shows linear relationship between amount of fluorescence molecules deposited on a slide and integrated intensity detected from those molecules. Large symbols at higher effective volumes denote 1-µl pipetted drops at various dilutions; small symbols denote 14-nl pin printed spots at various dilutions. The points have been offset horizontally to reveal the number of data points in each group; the proper x-axis position of each group of data points is marked on the x-axis below the points.

The least-squares best fit has slope $(6.061 \pm 0.020) \times 10^6$ in units of calibration-slide intensity × 10-um pixels / µl of stock target DNA. It also has a nonzero intercept at 220 ± 130 calibration-slide intensity × 10-µm pixels, which does not have an obvious physical interpretation, since the background, including the scanner dark current, had already been subtracted from the data. If the intercept is constrained to zero, the slope increases slightly to $(6.063 \pm 0.020) \times 10^6$. In both cases, this means that each microliter of stock labeled target DNA solution produces an fluorescence signal equivalent to a 6 cm^2 area (six million 10-µm×10-µm pixels) with the same intensity as the GP8 calibration slide, under the same scanning conditions. I will use the best fit with the nonzero intercept to compute the efficiency of hybridization on my microarrays. The fit looks close on a log scale, but the standard deviation of the residuals, after normalizing by the fit, is 100%. If we consider only the pipetted data, the standard deviation is 42%. This means that the data collected to form this calibration curve have a great deal of scatter, and the calibration curve has a large uncertainty in estimating the calibration data.

9 APPENDIX: CORNING GAPS II MICROARRAY SLIDE MANUAL

The manual for the Corning GAPS II microarray substrates is excerpted here for completeness. It is also available from < http://www.corning.com/Lifesciences/technical_information/techDocs/gaps_ii_manual_protocol_5_02_cls_gaps_005.pdf >.

GAPS II Coated Slides

Instruction Manual

For Research Laboratory Use Only

Cat. No. 40003 – Slides with Bar Code

Cat. No. 40005 – Slides with Bar Code (bulk packaged)

Cat. No. 40004 – Slides without Bar Code

Cat. No. 40006 – Slides without Bar Code (bulk packaged)

For the most current information and detailed protocols, visit our website at **www.corning.com/lifesciences**

CONTENTS

9.1 Introduction

9.1.1 Overview

Corning® GAPS II Coated slides have a uniform, covalently bound coating of pure Gamma Amino Propyl Silane that gives the slides a high quality, DNA immobilizing surface. The quality of nucleic acid arrays produced is highly dependent on the substrate. A poor quality coated glass slide will lead to problems with spot uniformity and morphology as well as high and varying background fluorescence. The spots may vary in size, shape, and DNA retention due to varying surface energies across the slide. Scratches and foreign material on the slide surface also cause deformation of the array as well as varying background fluorescence. These quality issues all lead to a loss in sensitivity and generally poor results.

GAPS II slides are manufactured under the most stringent conditions to overcome these quality issues. All slides are cleaned and individually examined for mechanical defects and the presence of dust and glass particles. Using a proprietary process, GAPS is applied in an environmentally controlled, HEPA-filtered ISO Class 5 facility, resulting in coated slides with highly uniform surface properties and low autofluorescence. Surface wetability is consistent across the slide surface to assure uniform spot size and shape and to avoid uncontrolled wicking or poor volume

transfer during the print. Amine density is also uniform across the slide surface leading to uniform DNA retention across the printed array. Packaging has been developed to maintain the appropriate storage environment.

9.1.2 Handling and Care Instructions

GAPS II slides are manufactured by a carefully controlled manufacturing process to maximize their performance. To assure this performance, please follow these recommendations:

Use the slides in a clean environment. Particles falling onto the slide surface may cause defects in the printed array as well as nuclease contamination. Self-contained printing environments may be required to prevent such contamination.

Avoid direct contact with the surface of the slide to be printed. Only the print pins and processing solutions should touch the print area to avoid contamination and abrasion of the coating. The coating is very thin and contact with the surface can affect its integrity.

When using slides without bar codes, always print on the side facing away from the wall of the plastic container. Clearly mark the side to be printed using a glass-etching tool.

If the package has been inadvertently stored at temperatures lower than 20°C, allow the foil pouch to come to room temperature before opening. Otherwise, condensation may form on the slide surface, negatively affecting the wetability of the coating.

Open the metalized foil pouch just prior to printing. Close the cap on the slide container as soon as possible after removing slides for use to maintain a closed environment for unused slides. Place the closed container in the foil pouch to protect

the remaining slides and store them in a desiccator. Use the remaining slides within one week.

The original slide container protects the print zone on the slide's surface. The container is therefore a good place to store slides after printing and/or hybridizing. Keep arrays hybridized with fluorescent probes in a light-tight box to prevent photobleaching.

9.1.3 Storage Instructions

For best results, store product at room temperature (20 to 25°C) in original undamaged packaging, and use slides by the date indicated on the label. After opening, store as described in the Handling and Care Instructions.

9.2 DNA array preparation and hybridization protocols

9.2.1 General Considerations

The surface of GAPS II Coated slides is highly reactive towards DNA. The key to producing microarrays of high 2 quality is to take advantage of this high reactivity during the printing process while minimizing the spurious attachment of nucleic acids to the unprinted area during subsequent manipulation of the array. The following are some of the most critical factors to consider:

Concentration of the DNA. The high reactivity of GAPS II Coated slides allows the use of printing solutions containing as little as 25 ng of DNA per microliter. The optimal concentration needs to be determined empirically. We recommend 0.1 mg/mL as a starting point. When too little DNA is used, the printed spots will not reach signal saturation levels, thus reducing the dynamic range of the array; on the other hand, highly concentrated printing solutions can produce spots with "comet

tails" and other forms of localized background. The concentration and purity of the DNA should be checked spectrophotometrically as well as electrophoretically.

Composition of the printing solution. The chemical and physical properties of the solvent greatly influence DNA retention, spot morphology, and hybridization efficiency. The ideal printing solution is one that denatures the DNA and has low evaporation rate. Denatured DNA binds more efficiently to the GAPS coating and readily hybridizes to the labeled probe. Ionic attachment of the negatively charged phosphate groups of the DNA backbone to the free amine groups on the surface of the slide occurs in the liquid phase. Solvent evaporation causes the concentration of DNA and other nonvolatile components of the printing solution to rise, leading to time-dependent changes in spot quality and the eventual loss of the printing solution. A solvent that evaporates slowly increases DNA retention and spot uniformity.

Immobilization procedures. Binding of DNA to the GAPS coated surface is enhanced by UV crosslinking and baking. These procedures work equally well at immobilizing the printed DNA.

Blocking procedures. Although most forms of background fluorescence are not additive to the signal intensity of printed spots, their occurrence is esthetically unpleasant and may interfere with spot identification during image analysis. Deactivating the unused surface of the slide greatly reduces the incidence of high background. For this purpose, we strongly recommend that albumin be included in the prehybridization buffer, as described below.

Arrayer settings and pin quality: Follow the instructions provided by the manufacturer of arraying equipment and printing pins. Pin contact time and the force with which the pin strikes the slide affect spot size and morphology. It is strongly

recommended that the printing pins be qualified before use. Pins that are either broken or out-of-spec can ruin otherwise good arrays.

The quality of the probe and the hybridization and washing conditions greatly influence the performance of printed arrays. Optimized protocols for the use of Corning® GAPS Coated Slides have been published[1,2] and should be used as starting points to find the printing and processing conditions that best fit the reality of each laboratory. The following protocols have been successfully used in Corning laboratories.

9.2.2 Printing and Hybridization of DNA Arrays on GAPS II Slides

9.2.2.1 Printing Solution Selection

Various formulations have been used for printing DNA arrays on GAPS slides. Final determination as to what solution to use is left for the user to make. Do not add detergents to the printing solution, as their presence inhibits binding between the DNA and the GAPS molecules.

3X SSC, 1.5 M betaine[2]

Advantages

Denatures the DNA

Low evaporation rate

Interacts well with GAPS coating, producing more uniform spots

Disadvantages

Very hygroscopic; best when arrays are processed immediately after baking

50% DMSO

Advantages

Denatures the DNA

Low evaporation rate

Interacts well with GAPS coating, producing more uniform spots

Disadvantages

Strong irritant

Produces spots of large diameter, sometimes causing spots to merge

Causes aggregation of DNA at concentrations of DMSO higher than 70%

3X SSC

Advantages

Commonly used aqueous solvent

Produces spots of small diameter, allowing high printing density

Disadvantages

Does not denature the DNA

High evaporation rate, requiring carefully controlled printing environment

150 mM NaPO4, pH 8.5

Similar to 3X SSC in terms of advantages and disadvantages

9.2.2.2 Array Printing

As the GAPS surface provides free amine groups for ionic attachment of the negatively charged phosphate groups of the DNA backbone, the DNA to be printed need not be derivatized with an amine or other chemical group. Such modifications, however, will not interfere with the interaction.

1. Resuspend DNA to a maximum of 0.25 mg/mL (0.1 mg/mL is a good starting concentration for optimization) in your choice of printing solution.

2. Transfer resuspended DNA to Corning plates (Cat. No. 3656 for 384 well or Cat. No. 3357 for 96 well).

3. Setup arrayer and print slides (bar code label side up) according to manufacturer's or laboratory protocol. Be sure to label side used for printing when using slides without bar code.

9.2.2.3 Array Stabilization and Immobilization

1. Rehydrate arrays by holding slides (array side down) over a bath of hot double distilled H2O (95 to 100°C) for approximately 5 sec until a light vapor film is observed across the slide.

2. Snap-dry each array (DNA side up) on a 100°C hot plate for approximately 5 to 10 sec.

3. UV cross-link DNA to the slide by using a UV crosslinker (150 to 300 mJoules) or by baking the array at 80°C for 2 to 4 hours. Care should be taken regarding the cleanliness of the baking oven. Volatile organics can irreversibly contaminate the surface of the array leading to high backgrounds.

9.2.2.4 Array Hybridization

9.2.2.4.1 Preparation of Probe Solution

Most DNA arrays are hybridized with fluorescently labeled cDNA using various reverse-transcription protocols and commercially available reagents. The quality and cleanliness of the starting RNA and the resulting cDNA are critical factors for successful use of the arrays. It is recommended that the labeled cDNA be purified and quantitated spectrophotometrically.

Use between 20 and 45 µL of probe solution, depending on the size of the printed area and coverslip. Do not exceed a probe concentration of 10 ng/µL of cDNA. Best results are obtained with probes having a frequency of incorporation (FOI) of 20 to 50 labeled nucleotides per 1,000 nucleotides of cDNA. The FOI can be calculated using the following formulae.

Amount of cDNA probe (ng) = A260 × 37 × total volume of probe (µL)

pmol of dye incorporated =

for Cy3™: A550 × total volume of probe/0.15

for Cy5™: A650 × total volume of probe/0.25

FOI = pmol of dye incorporated × 324.5/ng of cDNA probe

When using more than one type of fluorescent nucleotide, such as the commonly used combination of cyanine-3 and cyanine-5 dyes, mix equivalent amounts of labeled cDNA, measured as the number of pmoles of incorporated Cy-dCTP.

9.2.2.4.2 Hybridization option A: Hybridization Using Formamide

Optimized probe preparation and hybridization instructions can be found on the Life Sciences web site **www.corning.com/lifesciences** in the technical bulletin titled: "Detailed Instructions for Hybridization of cDNA Probes to dsDNA Arrays Made on GAPS Slides."

9.2.2.4.2.1 Pre-Hybridization

1. Incubate arrays in 25 to 50% formamide, depending on the desired stringency, 5X SSC, 0.1% SDS, 0.1 mg/mL BSA in a Coplin jar for 30 to 60 minutes at 42°C.

2. Wash arrays by immersing in water followed by rinsing in isopropanol. Make sure the SDS is completely removed from the arrays during this step.

3. Dry arrays by centrifugation or blow dry using compressed N2.

9.2.2.4.2.2 Hybridization

1. Prepare probe in fresh hybridization solution consisting of 25 to 50% formamide (use the same formamide concentration as for pre-hybridization), 5X SSC, 0.1% SDS, and 0.1 mg/mL of a nucleic-acid blocker of choice, such as sonicated herring or salmon sperm DNA, human Cot1 DNA, etc.

2. Incubate the probe solution at 95°C for 5 min.

3. Centrifuge the probe for 2 min to collect condensation and let sample cool to room temperature.

4. Place array in Corning Hybridization Chamber (Cat. No. 2551). Pipette the probe onto the surface of the printed side of the slide. Carefully place the coverslip on top of the array in such a manner as to avoid the formation of air bubbles under the coverslip.

Small air bubbles that do form usually dissipate during hybridization. Assemble the chamber as described in its package insert.

5. Submerge the chamber in a 42°C water bath or place in a hybridization oven overnight.

9.2.2.4.3 Hybridization Option B: Hybridization Without Formamide

9.2.2.4.3.1 Pre-Hybridization

1. Incubate arrays in 3X SSC, 0.1% SDS, 0.1 mg/mL BSA in a Coplin jar for 30 to 60 min at 50°C.

2. Wash arrays by dipping in water followed by rinsing in isopropanol. Make sure the SDS is completely removed from the arrays during this step.

3. Dry arrays by centrifugation or blow-dry using compressed N2.

9.2.2.4.3.2 Hybridization

1. Prepare probe in 3X SSC, 0.1% SDS, and 0.1 mg/mL of a nucleic-acid blocker of choice, such as sonicated herring or salmon sperm DNA, human Cot1 DNA, etc.

2. Heat at 95°C for 1 min.

3. Centrifuge the probe for 2 min to collect condensation, and let sample cool to room temperature.

4. Place array in Corning Hybridization chamber (Cat. No. 2551). Pipette the probe onto the surface of the printed side of the slide. Carefully place the coverslip on top of the slide in such a manner as to avoid the formation of air bubbles under the coverslip surface.

5. Small air bubbles that do form usually dissipate during hybridization. Assemble the chamber as described in its package insert.

6. Submerge the chamber in a 50°C water bath or place in a hybridization oven overnight.

9.2.2.5 Post-Hybridization Washing

DO NOT WASH SLIDES THAT HAVE BEEN HYBRIDIZED WITH DIFFERENT PROBES IN THE SAME WASH CONTAINERS.

DO NOT WASH MORE THAN 4 SLIDES IN A 200 ML STAINING JAR.

DO NOT ALLOW ARRAYS TO DRY OUT BETWEEN WASHES.

1. Disassemble the hybridization chamber right side up.

2. Remove the coverslip by immersing the array in 2X SSC, 0.1% SDS (at 42°C) until the coverslip moves freely away from the slide.

3. Place array in 2X SSC, 0.1% SDS for 5 min at 42°C.

4. Place array in 0.1X SSC, 0.1% SDS for 10 min at room temperature.

5. Place array in 0.1X SSC for 1 min at room temperature. Repeat 4 times.

6. Rinse array in 0.01X SSC for up to 10 sec or less.

7. Dry arrays by centrifugation or blow-dry using compressed N2.

8. Scan.

9.3 References

1. Hedge, P. et al, 2000. A concise guide to microarray analysis. *Biotechniques* 29:548-562.

2. Diehl, F et al, 2001. Manufacturing DNA microarrays of high spot homogeneity and reduced background signal. *Nucleic Acids Research* 29, e38.

For questions, further clarification about this protocol, and other technical issues and information not covered in this manual, please e-mail **actoncs@acton.corning.com** or call 800-492-1110 (978-635-2200 outside Canada and USA). A detailed hybridization protocol can be found on our website at **www.corning.com/lifesciences.**

9.4 Corning products for microarray printing

Cat. No.	Product Description	Qty/Pk	Qty/Cs
40003	GAPS II coated slides with bar code	5	25 slides
40004	GAPS II coated slides without bar code	5	25 slides
40005	GAPS II coated slides with bar code, bulk	25	25 slides
40006	GAPS II coated slides without bar code, bulk	25	25 slides
40015	UltraGAPS™ coated slides with bar code	5	25 slides
40016	UltraGAPS coated slides without bar code	5	25 slides
2551	Hybridization Chamber	1	5 chambers
40001	Hybridization Chamber O-rings	5	5 rings

Visit Coming Life Sciences website at www.corning.com/lifesciences to learn about and order Corning microplates and other laboratory consumables.

Corning Incorporated

Life Sciences

45 Nagog Park

Acton, MA 01720

t 800.492.1110

t 978.635.2200

f 978.635.2476

Corning has applied for patents concerning the use of GAPS coated slides in GPCR membrane microarray applications. GAPS II coated slides are not manufactured to the specifications required for use in this application. Purchase of these slides does not imply a license to use GAPS II coated slides for GPCR membrane applications.

Corning Incorporated, One Riverfront Plaza, Corning, NY 14831-0001

REFERENCES

Adey NB, Lei M, Howard MT, Jensen JD, Mayo DA, Butel DL, Coffin SC, Moyer TC, Slade DE, Spute MK, Hancock AM, Eisenhoffer GT, Dalley BK, McNeely MR. 2002. "Gains in sensitivity with a device that mixes microarray hybridization solution in a 25-µm-thick chamber." *Anal. Chem.* 74:6413–6417.

Alberts B, Bray D, Lewis J, Raff M, Roberts K, Watson JD. 1994. *Molecular Biology of the Cell,* 3rd ed. New York: Garland Publishing. p. 349.

Aref H. 1984. "Stirring by chaotic advection." *J. Fluid Mech.* 143:1–23.

Berkooz G, Holmes P, Lumley JL. 1993. "The proper orthogonal decomposition in the analysis of turbulent flows." *Annu. Rev. Fluid Mech.* 25:539–575.

Best C, Ideker T, Kahn J, Monte D, Tom E. 2003. "Troubleshooting Guide." In Bowtell DDL, Sambrook JF, editors, *DNA Microarrays: A Molecular Cloning Manual.* Cold Spring Harbor: Cold Spring Harbor Laboratory Press. pp. 240–256.

Bowtell DDL, Sambrook JF, editors. 2003. *DNA Microarrays: A Molecular Cloning Manual.* Cold Spring Harbor: Cold Spring Harbor Laboratory Press. 712 p.

Brandstäter A, Swift J, Swinney HL, Wolf A, Farmer JD, Jen E, Crutchfield JP. 1983. "Low-dimensional chaos in a hydrodynamic system." *Phys. Rev. Lett.* 51:1442–1445. Erratum: 51:1814.

Bregman DB, Du L, Vanderzee S, Warren SL. 1995. "Transcription-dependent redistribution of the large subunit of RNA polymerase II to discrete nuclear domains." *J. Cell. Biol.* 129:287–298.

Brown PO, editor. 1999. “MGuide: Hybridization of Arrays.” Available at < http://cmgm.stanford.edu/pbrown/protocols/5_hyb_yeast.html >, accessed 9 August 2005.

Cantor CR, Schimmel PR. 1980. *Biophysical Chemistry, Part 2: Techniques for the Study of Biological Structure and Function.* New York: W.H. Freeman and Co. pp. 656–658.

Cantor CR, Schimmel PR. 1980. *Biophysical Chemistry, Part 3: The Behavior of Biological Macromolecules.* New York: W.H. Freeman and Co. pp. 979–994, 1029–1031, 1036.

Chan V, Graves DJ, McKenzie SE. 1995. “The Biophysics of DNA Hybridization with Immobilized Oligonucleotide Probes.” *Biophys. J.* 69:2243–2255.

Chen QR, Bilke S, Khan J. 2005. “High-resolution cDNA microarray-based comparative genomic hybridization analysis in neuroblastoma.” *Cancer Lett.* 228:71–81.

Chertkov M, Lebedev V. 2003. “Acceleration of chemical reaction by chaotic mixing.” arXiv:nlin.CD/0301037, LANL/LAUR021743.

Copeland KG, Grogan TM, Miller PC, Richards WL, Showalter WA. 1997. “Method for mixing reagent and sample mounted on a slide.” United States Patent 5,650,327.

Dai H, Meyer M, Stepaniants S, Ziman M, Stoughton R. 2002. “Use of hybridization kinetics for differentiating specific from non-specific binding to oligonucleotide microarrays.” *Nucleic Acids Res.* 30:e86 (8 pages).

DeRisi J, editor. 2001. “Microarrays.org: Protocol for Array Hybridization.” Available at < http://www.microarrays.org/pdfs/ArrayHybProtocol.pdf >, accessed 3 March 2003.

Duggan DJ, Bittner M, Chen Y, Meltzer P, Trent JM. 1999. “Expression profiling using cDNA microarrays.” *Nature Genet.* 21:25–32.

Gadgil C, Yeckel A, Derby JJ, Hu WS. 2004. “A diffusion-reaction model for DNA microarray assays.” *J. Biotechnol.* 114:31–45.

Gamba A, Kolokolov IV. 1996. “The Lyapunov Spectrum of a Continuous Product of Random Matrices.” *J. Stat. Phys.* 85:489-499. arXiv:cond-mat/9610192.

Georgiadis R, Peterlinz KP, Peterson AW. 2000. “Quantitative Measurements and Modeling of Kinetics in Nucleic Acid Monolayer Films Using SPR Spectroscopy.” *J. Am. Chem. Soc.* 122:3166–3173.

Grogan TM, Rangel C, Rimsza L, Bellamy W, Martel R, McDaniel D, McGraw B, Richards W, Richter L, Rodgers P, Rybski J, Showalter W, Vela E, Zeheb R. 1995. “Kinetic-Mode, Automated Double-Labeled Immunohistochemistry and in situ Hybridization in Diagnostic Pathology.” *Adv. Pathol. Lab. Med.* 8:79–100.

Heaton RJ, Peterson AW, Georgiadis RM. 2001. “Electrostatic surface plasmon resonance: direct electric field-induced hybridization and denaturation in monolayer nucleic acid films and label-free discrimination of base mismatches.” *Proc. Natl. Acad. Sci. USA* 98:3701–3704.

Holloway AJ, van Laar RK, Tothill RW, Bowtell DDL. 2002. “Options available—from start to finish—for obtaining data from DNA microarrays II.” *Nature Genet.* 32:481–489.

International Association for the Properties of Water and Steam (IAPWS). 1997. *Revised Release on the IAPS Formulation 1985 for the Viscosity of Ordinary Water Substance.* Erlangen, Germany, 15. Accessed from < http://webbook.nist.gov/ >, 8 May 2005.

Jones JC, Phatnani HP, Haystead TA, MacDonald JA, Alam SM, Greenleaf AL. 2004. "C-terminal Repeat Domain Kinase I Phosphorylates Ser2 and Ser5 of RNA Polymerase II C-terminal Domain Repeats." *J. Biol. Chem.* 279:24957–24964. In particular: the caption to Table II.

Kohara Y, Noda H, Okano K, Kambara H. 2002. "DNA probes on beads arrayed in a capillary, 'Bead-array', exhibited high hybridization performance." *Nucleic Acids Res.* 30:e87.

Kohara Y. 2003. "Hybridization reaction kinetics of DNA probes on beads arrayed in a capillary enhanced by turbulent flow." *Anal. Chem.* 75:3079–3085.

Korkola JE, Estep AL, Pejavar S, DeVries S, Jensen R, Waldman FM. 2003. "Optimizing stringency for expression microarrays." *Biotechniques* 35:828–835.

Korn EL, Habermann JK, Upender MB, Ried T, McShane LM. 2004. "Objective method of comparing DNA microarray image analysis systems." *Biotechniques* 36:960–967.

Lehr HP, Reimann M, Brandenburg A, Sulz G, Klapproth H. 2003. "Real-time detection of nucleic acid interactions by total internal reflection fluorescence." *Anal. Chem.* 75:2414–2420.

Lenigk R, Liu RH, Athavale M, Chen Z, Ganser D, Yang J, Rauch C, Liu Y, Chan B, Yu H, Ray M, Marrero R, Grodzinski P. 2002. "Plastic biochannel hybridization devices: a new concept for microfluidic DNA arrays." *Anal. Biochem.* 311:40–49.

Lewin B. 2000. *Genes VII.* New York: Oxford University Press, Inc. p. 558.

Lis JT, Mason P, Peng J, Price DH, Werner J. 2000. "P-TEFb kinase recruitment and function at heat shock loci." *Genes Dev.* 14:792–803.

Liu RH, Lenigk R, Druyor-Sanchez RL, Yang J, Grodzinski P. 2003. "Hybridization enhancement using cavitation microstreaming." *Anal. Chem.* 75:1911–1917.

Lodish H, Berk A, Zipursky SL, Matsudaira P, Baltimore D, Darnell J. 2000. *Molecular Cell Biology,* 4th ed, New York: W.H. Freeman and Co. p. 272.

Martinez MJ, Aragon AD, Rodriguez AL, Weber JM, Timlin JA, Sinclair MB, Haaland DM, Werner-Washburne M. 2003. "Identification and removal of contaminating fluorescence from commercial and in-house printed DNA microarrays." *Nucleic Acids Res.* 31:e18.

Miller PC, Degroff MJ, Gizinski MJ, Rybski JA, Vandivort PS. 1993. "Immunohistochemical staining method and reagents therefor." United States Patent 5,225,325.

Naef F, Lim DA, Patil N, Magnasco M. 2002. "DNA hybridization to mismatched templates: A chip study." *Phys. Rev. E* 65:040902.

Nelson BP, Grimsrud TE, Liles MR, Goodman RM, Corn RM. 2001. "Surface plasmon resonance imaging measurements of DNA and RNA hybridization adsorption onto DNA microarrays." *Anal. Chem.* 73:1–7.

Nkodo AE, Garnier JM, Tinland B, Ren H, Desruisseaux C, McCormick LC, Drouin G, Slater GW. 2001. “Diffusion coefficient of DNA molecules during free solution electrophoresis.” *Electrophoresis* 22:2424–2432.

O'Brien T, Hardin S, Greenleaf A, Lis JT. 1994. “Phosphorylation of RNA polymerase II C-terminal domain and transcriptional elongation.” *Nature* 370:75–77.

O'Brien T, Lis JT. 1991. “RNA Polymerase II Pauses at the 5′ End of the Transcriptionally Induced *Drosophila hsp70* Gene.” *Mol. Cell. Biol.* 11:5285–5290.

Ott E. 1993. *Chaos in dynamical systems.* New York: Cambridge University Press. 385 p.

Ottino JM, Wiggins S. 2004. “Designing Optimal Micromixers.” *Science* 305:485–486.

Ottino JM. 1989. “The Mixing of Fluids.” *Sci. Am.* 260:56–67.

Ottino JM. 1990. “Mixing, Chaotic Advection, and Turbulence.” *Annu. Rev. Fluid Mech.* 22:207–253.

Pappaert K, van Hummelen P, Vanderhoeven J, Baron GV, Desmet G. 2003. “Diffusion-reaction modelling of DNA hybridization kinetics on biochips.” *Chem. Eng. Sci.* 58:4921–4930.

Pappaert K, Vanderhoeven J, van Hummelen P, Dutta B, Clicq D, Baron GV, Desmet G. 2003. “Enhancement of DNA micro-array analysis using a shear-driven micro-channel flow system.” *J. Chromatog. A.* 1014:1–9.

Patturajan M, Schulte RJ, Sefton BM, Berezney R, Vincent M, Bensaude O, Warren SL, Corden JL. 1998. "Growth-related changes in phosphorylation of yeast RNA polymerase II." *J. Biol. Chem.* 273:4689–4694.

Peterson AW, Heaton RJ, Georgiadis RM. 2001. "The effect of surface probe density on DNA hybridization." Nucleic Acids Res. 29:5163–5168.

Peterson AW, Wolf LK, Georgiadis RM. 2002. "Hybridization of mismatched or partially matched DNA at surfaces." *J. Am. Chem. Soc.* 124:14601–14607.

Probstein RF. 1994. *Physicochemical Hydrodynamics,* 2nd ed. New York: John Wiley & Sons, Inc. pp. 120, 123.

Rant U, Arinaga K, Fujiwara T, Fujita S, Tomow M, Yokoyama N, Abstreiter G. 2003. "Excessive Counterion Condensation on Immobilized ssDNA in Solutions of High Ionic Strength." *Biophys. J.* 85:3858–3864.

Rudkin GT. 1972. Replication in Polytene Chromosomes. In Beerman W, editor, *Developmental Studies on Giant Chromosomes.* New York: Springer-Verlag. pp. 61–85.

Sartor M, Schwanekamp J, Halbleib D, Mohamed I, Karyala S, Medvedovic M, Tomlinson CR. 2004. "Microarray results improve significantly as hybridization approaches equilibrium." *Biotechniques* 36:790–796.

Sato Y, Sato Y, Okumura A, Suzuki K, Kawaguchi H. 2004. "Flow-stress-induced discrimination of a K-ras point mutation by sandwiched polymer microsphere-enhanced surface plasmon resonance." *J. Biomater. Sci. Polym. Ed.* 15:297–310.

Schaupp CJ, Jiang G, Myers TG, Wilson MA. 2005. "Active mixing during hybridization improves the accuracy and reproducibility of microarray results." *Biotechniques* 38:117–119.

Sethna JP. 2005. E-mail message to Richard C. Yeh and Carl Franck dated 3 December 2005.

Sethna JP. 2006. *Statistical Mechanics: Entropy, Order Parameters and Complexity.* New York: Oxford University Press. 352 p.

Siggia E. 2001. Personal communication to Carl Franck.

Sprott JC. 2000. "Lyapunov Exponents." Available at < http://sprott.physics.wisc.edu/phys505/lect05.htm >, accessed 3 December 2005.

Sprott JC. 2003. *Chaos and Time-Series Analysis.* New York: Oxford University Press.

Sreenivasan KR. 1991. "Fractals and multifractals in fluid turbulence." *Annu. Rev. Fluid Mech.* 23:539–600.

Stellwagen E, Lu Y, Stellwagen NC. 2003. "Unified Description of Electrophoresis and Diffusion for DNA and Other Polyions." *Biochemistry* 42:11745–11750.

Stroock AD, Dertinger SKW, Ajdari A, Mezic I, Stone HA, Whitesides GM. 2002. "Chaotic mixer for microchannels." *Science* 295:647–651.

Tan PK, Downey TJ, Spitznagel EL Jr, Xu P, Fu D, Dimitrov DS, Lempicki RA, Raaka BM, Cam MC. 2003. "Evaluation of gene expression measurements from commercial microarray platforms." *Nucleic Acids Res.* 31:5676–5684.

Taylor JR. 1982. *An Introduction to Error Analysis: The Study of Uncertainties in Physical Measurements.* Mill Valley, CA: University Science Books. p. 150.

Toegl A, Kirchner R, Gauer C, Wixforth A. 2003. "Enhancing results of microarray hybridizations through microagitation." *J. Biomol. Tech.* 14:197–204.

Tritton DJ. 1988. *Physical Fluid Dynamics,* 2nd ed. New York: Oxford University Press. 544 p.

Tu Y, Stolovitzky G, Klein U. 2002. "Quantitative noise analysis for gene expression microarray experiments." *Proc. Natl. Acad. Sci. U S A.* 99:14031–14036.

Vainrub A, Pettitt BM. 2002. "Coulomb blockage of hybridization in two-dimensional DNA arrays." *Phys. Rev. E* 66:041905.

van Holde KE. 1985. *Physical Biochemistry,* 2nd ed. Englewood Cliffs, NJ: Prentice-Hall, Inc. p. 103, table 4.3.

van Ness J, Hahn WE. 1982. "Physical Parameters Affecting the Rate and Completion of RNA Driven Hybridization of DNA: New Measurements Relevant to Quantitation Based on Kinetics." *Nucleic Acids Res.* 10:8061–8077.

Wagner W, Pruss A. 2002. "The IAPWS formulation 1995 for the thermodynamic properties of ordinary water substance for general and scientific use." *J. Phys. Chem. Ref. Data* 31:387–535.

Wang D, Urisman A, Liu YT, Springer M, Ksiazek TG, Erdman DD, Mardis ER, Hickenbotham M, Magrini V, Eldred J, Latreille JP, Wilson RK, Ganem D, DeRisi JL. 2003. "Viral discovery and sequence recovery using DNA microarrays." *PLoS Biol.* 1:E2.

Weisstein EW. “Shear Stress.” *Eric Weisstein's World of Physics.* < http://scienceworld.wolfram.com/physics/ShearStress.html >, accessed 18 December 2005.

Wetmur JG. 1976. “Hybridization and renaturation kinetics of nucleic acids.” *Annu. Rev. Biophys. Bioeng.* 5:337–361.

Xia HM, Shu C, Wan SYM, Chew YT. 2006. “Influence of the Reynolds number on chaotic mixing in a spatially periodic micromixer and its characterization using dynamical system techniques.” *J. Micromech. Microeng.* 16:53–61.

Yauk CL, Berndt ML, Williams A, Douglas GR. 2004. “Comprehensive comparison of six microarray technologies.” *Nucleic Acids Res.* 32:e124 (7 pages).

Zehring WA, Lee JM, Weeks JR, Jokerst RS, Greenleaf AL. 1988. “The C-terminal repeat domain of RNA polymerase II largest subunit is essential in vivo but is not required for accurate transcription initiation in vitro.” *Proc. Natl. Acad. Sci. USA* 85:3698–3702.

Zhang Y, Hammer DA, Graves DJ. 2005. “Competitive Hybridization Kinetics Reveals Unexpected Behavior Patterns.” *Biophys. J.* 89:2950–2959.